UNIVERSITA' DEGLI STUDI DI NAPOLI

FEDERICO II

Russo Carmela

Characterization and synthesis of carbon aggregates in high temperature environment

Tutor:

Prof. Andrea D'Anna

Scientific Committee:

Dr. Anna Ciajolo
Prof. Andrea D'Anna
Prof. Eliseo Ranzi

Contents

Summary

Carbon materials in all its forms, from the natural carbon solid materials, as coal and graphite, to the synthesized carbon materials, as carbon black, pitch fibers, fullerenes, carbon nanotubes, etc,. have been object of many studies regarding their characteristics and behaviour due to their importance in the energy and industrial sectors.

Recently, most of the research efforts have been focused on the synthesis of new carbon materials and in particular on their physico-chemical properties which are very variable as a function of the production process. Arc discharge and laser ablation methods, chemical vapour deposition, pyrolysis and flame synthesis are the processes mostly used for production of special carbon materials as fullerenes, nanotubes, graphene, etc., whose structures are relatively simple and fairly well known. By contrast, traditional high-temperature pyrolytic and combustion processes in very fuel-rich conditions of gaseous, liquid, and solid fuels also produce a carbon material, namely soot, that is important when the enhancement of radiative transfer is required, but undesired for the pollutant effect. A special form of soot is carbon black that is an industrially-manufactured product used as filler in rubber products and as a component in ink for printers.

Soot and related high mass aromatic species, as polycyclic aromatic hydrocarbons, constitute as a whole the carbon particulate matter, in form of particles and aggregates, that can be produced starting from organic precursors, generally hydrocarbons, in high temperature partially oxidative conditions (fuel-rich) typical of combustion processes. Soot exhibits a mixed ordered/disordered character having a nano-structure mainly based on two-dimensional graphene layers grouped, cross-linked and/or layered each other in a disordered (turbostratic) way. The degree of order/disorder depends on the process temperature and fuel source.

This PhD thesis is focused on the study of the structural characteristics of carbon particulate matter, synthesized in the well-controlled combustion conditions of a premixed fuel-rich flame, where it is possible to study the parameters affecting their formation and, consequently, controlling their features. In this context the main objectives of this thesis are: i) to explore the diagnostic potentialities of fast and non-destructive spectroscopic tools for carbon characterization, ii) to get a deeper understanding of the formation mechanism of carbon materials in flames with the perspective of controlling and modulating the properties of carbon materials obtained.

Structural characterization of carbon materials at a nanoscale implies the determination of three key parameters that determine their structure and properties: the fraction of sp^2-bonded carbon sites, the hydrogen content and the ordering and clustering of sp^2 sites. Various characterization methods have been developed and implemented to determine these structural parameters. Among them, the

use of optical features have been in deeper investigated and focused on the upgrade and the exploitation of the diagnostic potentiality of spectroscopic tools. In particular UV-Visible, FT-IR and Raman spectroscopy, have been developed for the quantitative and qualitative characterization of flame-derived carbon soot materials and their related micro- and nano-structure.

A reconstruction method of UV-Visible spectra has been developed as diagnostic tool discriminating the contribution and the spectral features of different molecular weight aromatic species to the spectral properties of carbonaceous species formed in flame.

A detailed procedure for the quantitative FT-IR analysis of aromatic and aliphatic hydrogen has been set up by using different standard aromatic and aliphatic species and implemented on hydrogen-rich and hydrogen-poor carbon materials.

Regarding Raman spectroscopy, there are no multiwavelength Raman data for flame formed soot. Part of this work was devoted to fill this gap by providing Raman spectra at different excitation energies and exploiting the resonant Raman process as a powerful mean for soot structural and electronic characterization.

On the basis of the experimental results obtained, relationships between synthesis/combustion conditions and specific carbon properties, such as size distribution, chemical composition, optical properties and internal structural organization, have been found. This has led to give further insights on the carbonaceous species formation mechanism into a flame environment.

According to this general overview of the approach followed during this thesis work, the manuscript has been organized as follows.

Sect. I reports an overall description of the wide carbon world, ranging from perfect allotropes to disordered carbons.

In Sect. II the background concepts of each diagnostic and the status of art relatively to the analysis of carbon materials are presented.

In Sect. III the experimental details on the sample and the characterization techniques used to derive the relevant properties of carbon particulate matter are given.

Finally, in Sect. IV the main experimental data and their discussion are reported presenting a set of useful correlations between spectral and structural parameters.

Introduction

Unquestionably, carbon is the ubiquitous and most versatile element of the periodic table, however only in the late 18th century carbon began to be treated and studied as a chemical element. When Lavoisier listed “Carbone” in his “Traité Elémentaire de Chimie” as a new chemical element, scientific researchers had already discovered the versatility of carbon since it had been identified as the elementary component of both diamond and graphite.

Carbon materials have long been revered for their outstanding materials properties. Since the recent discovery of fullerenes, carbon nanotube and graphene, the element carbon has caught even more the attention of a great part of the scientific community.

The unique electronic configuration of the carbon atom gives it the ability to form different hybridized atomic orbitals, that give in turn the possibility to adapt itself in many different molecular, crystalline and disordered forms. The nature of the chemical bonds underlies the varied chemical and physical properties of the carbon materials. The unique and tunable properties of carbon-based materials enable technologies for identifying and addressing new challenges, confirming the statement that Walker addressed to carbon in the far 1990 defining it as a “an old but new material revisited” (Walker, 1990)

1 Carbon-based materials

Historically, carbon has played an important rule in the daily life of humans since prehistoric times when it could be commonly used as main component in black inks for painting.

Many of the things we use in our day-to-day life contain carbon. Carbon is in the pencil we use, in the diamond we wear, on the street we drive. Carbon is everywhere. Over 95% of all known chemical compounds are 'carbon-based compounds'. Although some other elements can bond to themselves to form chains and clusters, none of them equals carbon in the extent and versatility of its catenation.

Carbon is the sixth element of the periodic table. Each carbon atom has six electrons which occupy 1s2, 2s2, and 2p2 atomic orbitals. The 1s2 orbital contains two strongly bound core electrons. Four more weakly bound electrons occupy the 2s2 and 2p2 valence orbitals. Since the narrow energy gap between the 2s and 2p electron shells, the electronic wave functions for these four electrons can readily mix with each other. The general mixing of 2s and 2p atomic orbitals is called hybridization and the mixing of a single 2s electron with one, two, or three 2p electrons is called sp^n hybridization with n = 1; 2; 3. It is possible to describe all carbon materials by combination of these different hybridization states. The physical, chemical and electronic properties of carbonaceous materials are strongly coupled to carbon atom structural conformation and, thus, to their hybridization state (Robertson, 2002). In nature, carbon appears in pure forms, as graphite and diamond, while the various non-crystalline carbons can be considered to be intermediate between diamond, graphite and hydrocarbon polymers. Due to carbon versatile bonding, this element has been used to shape a plethora of so many material forms that it has been necessary to bring order to the chaos of carbon world and state a clear nomenclature (Thrower, 2012; Fitzer et al., 1995).

1.1 Carbon allotropes

In order to give an overall description of the wide carbon world is better to start from the well assessed allotropic forms, that consist in different structural forms of this element. Diamond is made up exclusively of sp^3 bonded carbon atoms, while graphite is composed of ordered stacks of honeycomb sp^2 carbon layers. A schematic model of these two materials is reported in Fig.1. In the graphitic phase, the structure is highly anisotropic, showing semimetallic behaviour in the basal plane and poor electrical conductivity along the c-axis.

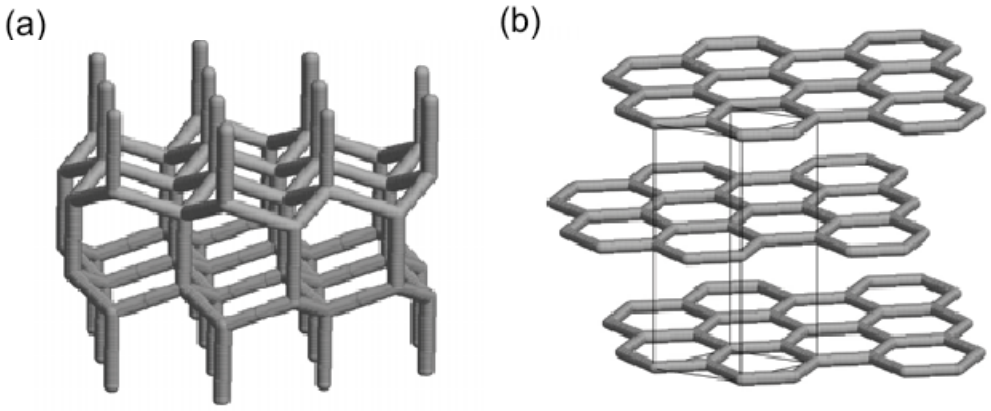

Fig. 1 Schematic model of diamond (a) and graphite (b)

The π electrons are delocalized along the graphitic layers. This feature is responsible for a high conductivity along these layers. In contrast to the semimetallic anisotropic graphite phase, diamond is a isotropic, cubic insulator. (Dresselhaus et al., 1996). Diamond's hardness (designated as 10 on the Mohs scale), extraordinary strength and high density (3.514 g/cm^3) is opposite to graphite's softness, low hardness (less than 1 in the Mohs scale) and low density (2.266 g/cm^3).

Fullerenes and carbon nanotubes constitute other recently discovered carbon allotropic forms. The close cage nearly spherical molecule C_{60} and related fullerene molecules ceased to be a hypothetic molecule (Osawa, 1970) and became true in the 1985 thank to Kroto et al.(Kroto et al, 1985), that were awarded the 1996 Nobel Prize in Chemistry. However, first representations of similar highly symmetric polyhedrons were already given by Leonardo da Vinci in about the year 1500 (De Divina Proportione, Luca Pacioli, 1498) and later by the architect Buckminster Fuller, from whom derived the name chosen for these new molecules, that resemble his geodesic domes.

Fullerenes are built up of fused pentagons and hexagons and have a bond hybridization which is intermediate between graphite and diamond due to their spherical shape. The response to this non planarity is the σ-character of curved π–orbitals (Kroto et al., 1993). The highly pyramidalized sp^2 carbon atoms in fullerene cause a large strain energy within the molecule. The smallest fullerene, C_{60}, made of twelve pentagons and twenty hexagons, has the highest number of 5-membered rings per benzene rings and is characterized by the largest pyramidalization angle (Henning et al., 2004). These molecules have attracted a great deal of interest since their discovery because their unique structure and properties. Because of the high symmetry of C_{60}, its relatively high abundance, and the fact that all C_{60} molecules are identical, C_{60} has been investigated as a prototype nanostructure for modelling purposes. In the field of nanotechnology, superconductivity (Haddon et al., 1991) is one of the most heavily studied properties. Fullerenes were also under study for potential medicine uses such as gene and drug delivery system, antioxidant activity (Bakry et al., 2007).

Carbon nanotubes, identified for the first time in the 1991 (Iijima, 1991; Iijima et al., 1993), have a cylindrical structure formed from rolled graphene sheet. Carbon nanotubes are capped at either end by half of a fullerene, so that the smallest diameter nanotube corresponds to the smallest fullerene diameter.

The fundamental carbon nanotube is a single-wall structure with three basic geometries: armchair, zigzag, and chiral. Carbon nanotubes have attracted a lot of interest because of their one-dimensional periodic structure with electronic structure that depends on their diameter and chirality (Dresselhaus et al., 1995). Nanotubes-based transistors have been made and operate at room temperature (Postma et al., 2001), wires fabricated from nanotubes exhibit a specific conductivity higher than metals (Zhao et al., 2011), however more controlled growth of nanotubes then the actual synthesis routes is necessary to provide carbon nanotubes with the same diameter and chirality.

Ultimately, fullerenes and nanotubes have engendered much excitement especially with regard to possible future applications, but actually they have had a limited impact on industry.

Now, graphene, the last discovered allotropic carbon form (Novoselov et al., 2004), a one-atom-thick flat sheet of carbon, is surrounded by favourable omens, not the least of which is the speed with which groundbreaking experiments on its properties were rewarded with the 2010 Nobel Prize in Physics.

It has been just six years since Nobel laureates Andre Geim and Kostya Novoselov at the University of Manchester, UK, first reported the exceptional properties of peeled atomically thin layers of graphene from graphite using scotch tape (Novoselov et al., 2004).

A single layer of graphene is simultaneously the world's thinnest, strongest and stiffest material, as well as being an excellent conductor of both heat and electricity. Graphene’s high electrical conductivity and high optical transparency make it a candidate for transparent conducting electrodes, required for touchscreens, in particular the flexibility is the graphene’s extra oomph in respect to indium tin oxide (Nathan et al., 2012). However, a single graphene sheet conducts charge so well that it is hard to make the current stop, something that must be solved if the material is ever going to be used in digital devices such as transistors, which control the flow of current like on–off switches. Material's electronic properties have to be changed in the appropriate way to creating a band gap, which essentially turns it into a semiconductor (Wang et al., 2009).

Likewise of diameter and chirality in nanotube, electronic behaviour in graphene depends on the size of a given sheet and on the presence or absence of defects. Currently, the most common techniques available for graphene production are chemical vapour deposition (Reina et al., 2009) and mechanical (Novoselov et al., 2004) and chemical exfoliation of graphite (Hernandez et al., 2008). Although its fascinating properties look promising for the advent of a new generation of

carbon nanomaterials, the large scale production of graphene has become a stumbling block on the road of further applications. To commercialize graphene, new methods for large-scale production of low cost and high-quality graphene are required. These processing difficulties suggest that graphene, as carbon nanotubes, will not soon have its market place. In the meantime, nano-carbon structures can be more competitive in less demanding electronics, solar cells and biomedical devices.

1.2 Disordered carbon material

Despite the most well known carbon forms are its perfect allotropes, the vast range of carbon materials, both natural and synthetic, are characterized by disordered structures, mainly due to the presence and the arrangement inside them of different hybridized carbons. These kinds of materials can exhibit a short-range crystalline order or can be totally disordered. Considering that graphite and diamond are the two main allotropic forms of bulk materials and remembering the so different properties that characterize these two carbon allotropes (see 1.1) it is easy to understand the wide range of materials that can be obtained tuning the amount of them.

1.2.1 Non-crystalline carbons

Tar-like materials, such as pitch, resins, bitumens, are a non-crystalline viscous materials, black or dark brown, that at relatively low temperature become fluid. In research on solid-fuel combustion, tar can mean any condensable product ejected from solid matter mainly through thermal treatment processes.

Pitch materials are used as binder in graphite electrode manufacture and in carbon-carbon composite and as precursor for the production for carbon fibers (Mochida et al., 2000). Tar pitches are traditionally obtained from coal tars that are the by-products of bituminous coal coking process used to produce metallurgic coke. Coal tar pitch is the residue obtained from coal tar distillation, which involves the conversion of coal tar into a variety of intermediate chemical products. A sharp decrease in coal production, due to the continuous decrease in the production of metallurgic coke caused by environmental and economical reasons, has led to a clear need to establish routes for producing pitches from alternative feedstocks or via non-traditional routes that do not rely on conventional metallurgical-coke-making technology (Schobert et al., 2002). Synthetic pitches have been already derived from aromatic monomers (Mochida et al., 1988) or from hydrotreatment of aromatic materials (Andresen et al.,2004).

Asphaltenes, generally contained in petroleum and coal, are another tar-like material of great interest. For instance asphalt, that is an asphaltene-derived product, has practical uses, such as material for road construction, waterproofing and roofing, and as curing agents and corrosion inhibitors. By contrast, asphaltenes are usually considered a problem in the oil field, since they cause a marked increase of petroleum viscosity, can precipitate and consequently clog flow lines. Naturally-occurring hydrocarbon fluids are compounds that span from dry natural gas to tar. Across that range, density and viscosity increase dramatically, and colour changes from clear to deep brown. The definition in use today for these materials is the heavy oil fraction insoluble in n-alkanes, such as n-pentane or n-heptane, and soluble in toluene. The definition of asphaltenes as a solubility class rather than as a chemical class underlies the difficulty to study them. Although many studies have been focused on these materials (Mullins et al., 2007) some difficulties still remain in the definition of a chemical structure for asphaltenes. However, in recent years the Yen-Mullins model (Mullins et al., 2012) has shown to be able to describe asphaltenes structure in agreement with the myriad experimental data provided on this material: they consists of a few number of fused ring systems substituted with alkylic chains.

To the family of non crystalline carbons belong also solid glassy carbons, that should not be confused with amorphous carbon since they consist of two-dimensional structural elements (Fitzer et al., 1995). Glassy carbons are widely used as electrode material in electrochemistry and for high-temperature crucibles. They are prepared by subjecting the organic polymeric precursors to a series of heat treatments at temperatures up to 3000°C carbon (Jenkins et al., 1970).

1.2.2 Short-range order carbons

In condensed matter physics, an amorphous (from the Greek a, without, morphé, shape, form) solid is a solid that lacks the long-range order characteristic of a crystal. According to the IUPAC recommendations amorphous carbon is a carbon material with short-range crystalline order (Fitzer et al., 1995). Generally speaking, an amorphous carbon can have any mixture of sp^3, sp^2, and even sp^1 sites, with the possible presence of up to 60% hydrogen. The variety of these materials is summarized on the ternary phase diagram (Robertson, 1996; Ferrari et al. 2000) reported in Fig.2.

Tetrahedral amorphous carbon ta-C and its hydrogenated analogue ta-C:H are characterized by a significant fraction of sp^3, while hydrogenated amorphous carbons, a-C:H, have a rather small C-C sp^3 content. However, this diagram dismisses an other important structural parameter in the characterization of amorphous carbons, namely the extension of the sp^2 phase, that plays a crucial role in the different optical, electronic, and mechanical properties of these materials.

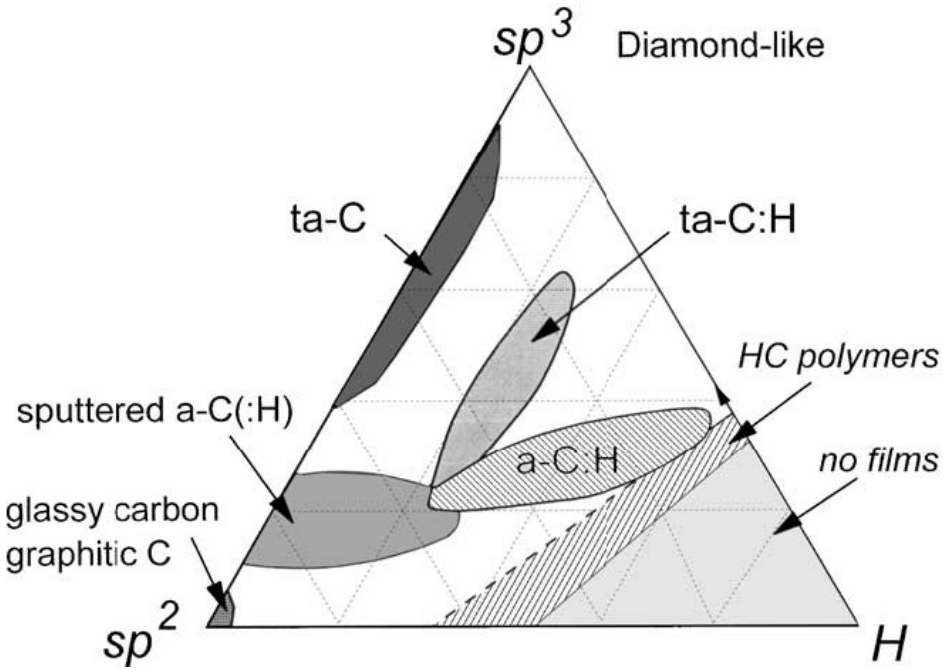

Fig.2 Ternary phase diagram of amorphous carbons (Robertson, 2002)

Warren in his 1934 work (Warren, 1934) carried out for the first time X-ray diffraction studies on carbonaceous materials. However, the first attempt to model the structure of amorphous material has to be addressed to Franklin in 1951 (Franklin, 1951), when she described these material as composed by basic units, small graphitic crystallites containing a few layer planes, which are joined together by crosslinks. The nature of the crosslinks was not specified. An illustration of Franklin's models (Franklin, 1951) is shown in Fig.3.

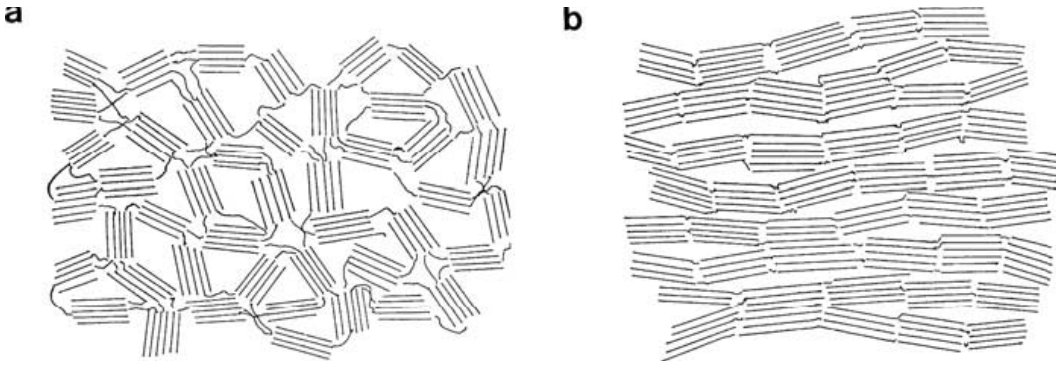

Fig.3 Franklin's representations of (a) non-graphitizing and (b) graphitizing carbons (Franklin, 1951).

With these models she tried to justify the different behaviour of graphitizing and non-graphitizing carbons during thermal annealing in order to convert them in a structure close to that of graphite, indeed by heating at high temperature, the three dimensional crystalline state of graphite, which is

termodinamically the stable phase, should be obtained. Graphitization should occur above 2100°C up to 3000°C , which allows the carbon atoms inside the graphene sheet to rearrange themselves so that they tend to achieve locally the three-dimensional order of graphite with nearly perfect domains. However, during her experiments, for some carbon materials the transformation of such structures into crystalline graphite did not occur, leading to hypothesize the presence of crosslinks between the graphitic domains that prevented this process.

The advent of high-resolution transmission electron microscopy in the 1970s (Oberlin, 1979; Oberlin 1990) allowed to image directly the structure of amorphous carbons. Starting from these pioneering studies, based on diffraction techniques as X-ray Diffraction (XRD) and Transmission Electron Microscopy (TEM), the structure of disordered carbon materials has been viewed as assemblies of basic structural units (BSU) also referred to as crystallites, constituted by few aromatic layers (fringes) of nanometric size (Warren, 1934; Biscoe et al., 1942; Franklin, 1951; Oberlin, 1979). The layers, although parallel to each other, are randomly stacked in a so-called turbostratic structure (Heidenreich et al., 1968), causing an interlayer spacing significantly greater (0.34–0.35) than in graphite (0.33 nm). This is because disordered carbon are composed of graphene layers of varying size characterized by a reciprocal random rotational displacement while graphite is in an ABAB stacking giving a hexagonal crystal. Fig 4 provides a schematic illustration of graphite and a turbostratic carbon.

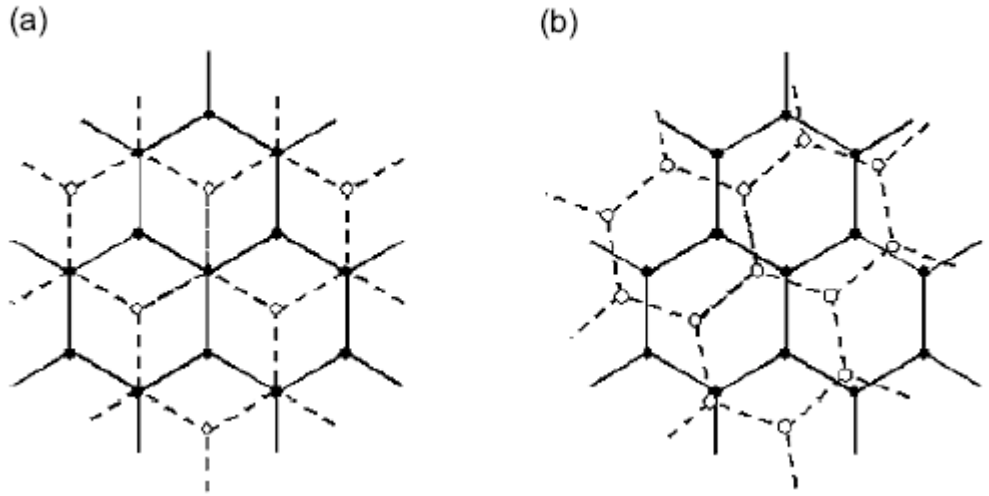

Fig. 4 Schematic illustration of a graphitic (a) and a turbostratic stacking of carbon layer.

Regarding the nature of the crosslinkers, there is still a debate (Harris, 2004; Harris, 2013). Some authors (Ergun et al., 1959; Ergun et al., 1965) after the experimental results obtained by Franklin have suggested that sp^3-bonded atoms may be present in non-graphitizing carbons, justifying in such way the hardness and density of them, entirely incompatible with a graphite-like structure.

They also recommend to describe the so called amorphous carbons as polytype-crystalline and not polycrystalline as they are composed by nanocrystalline domains, but of different type.

The discovery of fullerenes (Kroto et al, 1985) and subsequently of related structures such as carbon nanotubes (Iijima, 1991, Iijima et al., 1993) has given a new perspective for solid carbon structures. Carbons containing pentagonal rings, as well as other non-six-membered rings, among the hexagonal sp^2 carbon network, have shown to be highly stable. Evidence of curved structures from high-resolution TEM studies (Harris, 2005) and of pentagonal arrangement from a new generation of TEMs, able to resolve the atomic spacing (Harris et al. 2008), supported the idea (Harris, 2005) that non-graphitizing carbons may contain also fullerene-like structures.

The main prospective application for amorphous carbons focus on their wide mobility, gap and tribological properties. Studies of amorphous carbon have been widespread since 1971, when Aisenberg and Chabot (Aisenberg et al, 1971) for the first time deposited a thin film of this material, and the field has reached maturity in understanding the growth mechanisms, material properties and usage in industrial applications. Amorphous carbons are commonly employed as protective coatings for magnetic hard disks, razor blades, insulating films, etc (Grill, 1999). Despite the more ordered allotropic forms, from the application point of view amorphous carbon represents a complete success. The unique properties of amorphous carbon consist in the possibility to adjust the properties by choosing the right method of deposition or/and synthesis, making them suitable for the desired application. The class of amorphous carbon is so wide that in this paragraph only an overview on some of them is reported.

Carbon fibers are used in a wide range of applications, ranging from aircraft to sporting equipment and body prosthesis. They are produced by pyrolysis of organic precursors, the most common of which are polyacrylonitrile (PAN) and mesophase pitch. Depending upon the precursors and manufacturing processes, layer planes in carbon fibers may be either turbostratic, graphitic, or a hybrid structure (Harris, 2005; Huang, 2009).

Char coal, i.e not graphitizing carbon, due to their adsorptive property (Harris, 2013), are widely used in the purification of air and water (Patrick, 1995; Marsh et al., 2006) and in the clean-up of waste gases from industry.

Soot is the carbonaceous aerosol resulting from incomplete combustion. Carbon black, which is an industrially manufactured form of soot produced on a large scale, is used as a filler in rubber products and as a component in ink for printers. The first X-ray diffraction studies on carbon black and soot particles were carried out by Warren in the 1930s and 1940s (Warren, 1934; Biscoe et al., 1942), who described carbon black as an heterogeneous mixture of particles composed by single graphite layers up to graphite crystals made up of several stacked layers.

A detailed knowledge of the spectral behavior and nanoscale structure of soot particles is object of studies in many fields of research like environmental science, to calculate the global warming of the atmosphere produced by combustion processes (Bond et al., 2006), in astrophysics, since carbonaceous grains are a dominant component of interstellar dust and soot particles seem to be a good laboratory analogues (Jäger et al., 1998; Henning et al., 2004), in combustion, where the formation of condensed-phase materials has been studied (Haynes et al., 1981; Homann, 1985; Howard, 1991; Richter et al., 2000; Bockhorn et al., 2009).

1.3 Synthesis Methods of carbon materials

Carbon materials show characteristics which are strictly related to the manufacturing process.
Besides pyrolytic synthesis from organic materials (Franklin 1951; Jenkins et al., 1970; Harris, 2005; Huang, 2009), several methods have been set up and tested through years such as arc discharge, chemical vapour deposition, laser ablation and flame synthesis.
In the laser ablation technology a laser beam is focused onto a metal-graphite composite target which is placed in a high-temperature furnace (Guo et al., 1995). At high laser flux, the material is typically converted to a plasma. The laser beam scans across the target surface under computer control to maintain a smooth and uniform face for vaporization.
In the arc discharge a vapour is created between two carbon electrodes, usually graphite. The anode is either pure graphite or contains metals. After the triggering of the arc between two electrodes, a plasma is formed consisting of the mixture of carbon vapor, the rare gas (helium or argon), and the vapours of catalysts. The plasma can be stabilized for a long reaction time by controlling the distance between the electrodes by means of the voltage (25–40 V) control. The plasma arc-discharge method is historically the first carbon nanotube synthesis method. It led to the discovery of carbon nanotubes by Iijima. (Iijima, 1991). Arc-discharge and laser ablation methods for the growth of carbon nanotubes have been actively pursued in the past decades. Both methods involve the condensation of carbon atoms generated from evaporation of solid carbon sources. However, these techniques produce a complex mixture of components and requires further purification to separate carbon nanotubes from soot and residual catalytic metals present in the crude product.
Chemical vapour deposition (CVD) is a deposition process where chemical precursors are transported in the vapour phase to decompose on a heated substrate to form a film. The deposition involves homogeneous gas phase reactions, which occur in the gas phase, and/or heterogeneous chemical reactions which occur on/near the vicinity of a heated surface leading to the formation of powders or films, respectively (Choy, 2003). CVD has become the major method of film deposition

for the semiconductor industry due to its high throughput and purity. It seems to be the most promising method for possible industrial scale-up of nanomaterials synthesis , due to its ability to control and vary the coating microstructure by varying the process parameters, however the generation of a controlled high temperature environment and the use of substrate/catalysts still affect the final cost of the process.

The inexpensive synthesis of carbon solids possessing desired structures, composition and properties continues to be a challenge to chemists, material scientists and engineers.

Combustion as a method of material synthesis also has a rich history. Combustion synthesis makes use of highly exothermic oxidation reactions to achieve a high temperature environment.

Titania and silica are produced almost exclusively by flame processes (Ulrich, 1984).

Regarding carbon material, the flame synthesis of carbonaceous particles has been considered for years only an undesidered process due to their pollutant character. With the start of the nano-age, there has been tremendous interest in the combustion synthesis of materials because it is simple, fast, self-sustained and energetically economic compared to the conventional routes used to prepare carbon materials (Pope et al., 1993; Vander Wal, 2000; Merchan-Merchan et al., 2002; Savaliev et al., 2003; Merchan-Merchan et al., 2004, Merchan-Merchan et al., 2010).

The flame volume provides a carbon-rich chemically reactive environment able to generate nanostructures during short residence times in a continuous single-step process (Merchan-Merchan et al., 2010). The formation and growth of nanomaterials occur in the gas phase and the change of operative conditions, like the ratio between fuel and oxidant (D'Anna et al., 2009a), the mixing degree (Merchan-Merchan et al., 2002), the nature of the fuel (Santamaria et al. 2010; Sirignano et al. 2011; Russo et al., 2013a; Alfè et al., 2009; Carpentier et al., 2012) and the residence time inside the flame reactor (Russo et al., 2013a; Alfè et al., 2009), are quite effective in changing the structural properties of the carbon products.

A flame can be also envisioned as a particle generator to produce nanomaterials suitable for further modifications. Indeed, carbon particles produced with a conventional premixed flame have been fed to a plug flow reactor to coagulate and produce particles with determined size having the same composition of those produced in combustion (Sirignano et al., 2013).

Since the presence of so many parameters affecting the final form of the produced nanoparticles, a clear comprehension of their mechanism of formation is needed to optimize the process and achieve the desired products.

Beyond their common origin in flames, flame soot formation and nanomaterial synthesis by flames share many common characteristics. Nuclei and clusters, formed in the gas phase, further grow to nanoparticles by surface reaction, coagulation and coalescence, and finally by aggregation into

fractal structures (Roth, 2007). Each of the carbon particle formation steps in the flame will be analyzed and discussed in detail.

1.3.1 Flame synthesis of carbon materials

Recently the notable progress that has been made in the intervening years in the comprehension of combustion formed carbon particles formation has been summarized (Bockhorn et al., 2009). The combustion scientific community has shown to have reached maturity thanks to its heterogeneity, which largely involves physicists and chemists beside of engineers. However, a deep and complete knowledge of all mechanisms involved in particle formation is not achieved yet (Bockhorn et al., 2009; D'Anna, 2009b; Wang, 2011).

In particular, particle inception at high-temperature, i.e. the step which leads to the formation of three-dimensional structures starting from gas phase molecules, remains one of the less understood step in the soot formation process.

Thousands of species and tens of thousands of reactions ranging from pyrolysis, oxidation and recombination may be considered for practical fuels like gasoline, kerosene and diesel (Westbrook et al, 2005). During oxidation and pyrolysis, hydrocarbon fuel generates small fragments which react to form oxidized and pyrolytic products depending on oxygen availability.

A fraction of the hydrocarbon fragments can react forming the first aromatic ring. Two reaction pathways are considered for the formation of phenyl radical and benzene: the addition of n-C_4H_3 and n-C_4H_5 to C_2H_2 (Frenklach et al. 1990; Frenklach, 2002), leading to phenyl and benzene + H, respectively, and more likely the self-combination of propargyl radicals (Miller et al.,1992).

The growth of planar PAH, starting from smaller aromatic hydrocarbons, through H-atom abstraction and acetylene addition reactions (H-Abstraction aCetylene Addition or HACA mechanism, (Frenklach, 2002) is too slow to account for rates observed for larger PAH formation and soot nucleation (Richter et al., 2000; Wang 2011).

D'Anna et al. (D'Anna et al., 2000) developed a new detailed kinetic mechanism for aromatic growth, which emphasizes the role of resonantly stabilized radicals, that are relatively stable due to the delocalization of the unpaired electron, and can therefore attain high concentrations in combustion, becoming attractive as building blocks for higher MW aromers. Even though it is now possible to depict benzene and light PAH formation processes in hydrocarbon flames with a reasonable degree of accuracy, the transition from heavy PAH molecules to nascent soot particles is in need of further research.

A basic understanding of PAH growth and clustering kinetics is crucial for a critical analysis and prediction of particle formation in flames, but chemical details on the formation of nascent soot particles are relatively poorly understood, mostly because of experimental difficulties. Indeed, the efficient identification of species with molecular masses less than about 300 amu produced at different stages of the growth process has been provided using gas chromatography. By contrast, the main problem regards the identification and characterization of heavier MW species, since conventional diagnostic techniques are not useful for the analysis of species in this MW range, where intermediate compounds between PAH and early soot particles fall (Ciajolo in Bockhorn et al., 2009). To overcome this problem and probe the nature and concentration of high molecular mass species, mass spectrometry (Alfè et al., 2008; Dobbins et al., 1995; Apicella et al., 2007; Faccinetto 2011; Grotheer et al., 2011) and optical diagnostics (D'Alessio et al.,1992; P. Minutolo et al.,1996; Apicella et al., 2004; Miller et al., 2013; Ciajolo et al.,1998; Ciajolo et al., 2001; Russo et al., 2012; Russo et al., 2013b), performed in situ or after sample extraction, have been carried out. Chemical and spectroscopic analysis give an indication of the chemical nature of soot precursors and show that at some size flame-PAHs begin to stick together to form nanoparticles that can be thought as three-dimensional structures composed by interacting PAH. Stacked PAH structures are preferentially formed at low temperatures and low radical concentrations. On the other hand, adjacent and/or facing aromatic structures linked by aliphatic bonds are favoured when chemical growth mechanism is enhanced, i.e. at higher temperatures and higher radical concentrations (Homann 1998, D'Anna 2009b).

Once the first particle is formed, it can grow through surface reaction. Molecular growth is responsible for the soot loading, i.e. the formation of large amount of particulate in terms of volume fraction. In particular, the addition of acetylene follows a reaction pathway similar to the HACA mechanism found and described for the gas phase (Frenklach et al., 1994). However, literature values for the carbon rate addition from acetylene to soot may be too high when for the observed soot growth rate the contribution of other reactants, like PAH or tars, is not taken into account since they may contribute significantly to soot growth (Howard, 1991).

Primary particles characterized by a very small size tend to form a single larger particle. This process can be associated with coalescence after that the identity of the sticking particles is lost (Dobbins et al., 1987). This causes the rapid broadening and splitting in two modes for the size distribution (D'Alessio et al, 2005).

Transmission electron microscopy (TEM) identifies mature soot as fractal aggregates composed of nearly spherical primary particles or spherules (Alfè et al., 2009; Dobbins et al., 1987; Zhang et al.,

1998). Aggregates are formed from coagulation of primary particles or smaller aggregates, which have no longer the capability to give coalescent coagulation.
At higher residence times under pyrolytic conditions in the postflame zone, formed particles and/or aggregates undergo functional group elimination, ring condensation and fusion leading to growth and alignment of polyaromatic layers. This process converts the initially amorphous soot material to a progressively more graphitic carbon material, resembling onion-like structures.
Even in extra-terrestrial soot condensation processes, the soot formation and the role of PAHs (side product or precursor) are not sufficiently understood (Jäger et al., 2006). Researches in interstellar carbons are trying to apply and adapt the knowledge reached in combustion science to describe the growth and evolution of carbon nanograins in space (Carpentier et al, 2012). These fields of research have shown to have a lot of common points and a stronger cooperation in future would be fruitful to solve shared issues.
As discussed in this paragraph and highlighted in the Anacapri workshop (Bockhorn et al., 2009) a great deal of attention has to be placed on the mechanism of soot inception. An issue closely related to this problem is the nature and chemical composition of nascent particles, that have shown to be different from the mature soot (D'Alessio in Bockhorn et al., 2009). To address this and related questions, chemical nature and composition of these particles is a fundamental step to develop new detailed kinetic mechanism. Progress in chemical analysis of incipient soot constitutes a major step in this direction.

1.4 Characterization of carbon materials

Investigations of nanosized object have been gone on in parallel with efforts to design and manipulate matter on a similar scale. With both characterization and fabrication tools capable of handling the nanometer size regime, it is possible to systematically manufacture devices with desired nanoscale dimensions, examine the results of synthesis process and carefully characterize the material properties. In this manner, the influence of nanostructure size on the mechanical, electrical, optical, magnetic and chemical properties of a multitude of materials can be investigated.
While carbon allotropes have a well-defined structure, a disordered carbonaceous material is fully characterized only when the amount of sp^2 and sp^3 bonds, hydrogen and the degree of sp^2 clustering are known (Ferrari et al., 2000).
In spite of the unique features of XRD and TEM techniques in exploring the internal structure of carbon materials, it has to be emphasized that this kind of analysis is circumscribed to the determination of basic structural unit (BSU) characteristics, i.e. to the more ordered, quasi-

crystalline portion of carbon materials (Vander Wal et al., 2003; Llamas-Jansa et al., 2007; Alfè et al., 2009, Russo et al., 2013a). Therefore, such images tend to have a ribbon-like appearance. However, because only a part of the structure is imaged, this appearance can be misleading and the true three-dimensional structure may be more cage-like than ribbon-like. This is a very important point and must always be borne in mind when analyzing images of graphitic carbons (Harris, 2005). Moreover, the XRD and HR-TEM imaging gives two-dimensional information about a three-dimensional object orthogonally projected on the screen.

Recent advancements in High-Resolution Transmission-Electron Microscopy (HRTEM) imaging analysis have allowed the individuation of single layers, properly defined as non-stacked layers [Galvez et al., 2002]. Also these non-stacked layers have to be cross-linked in some way to justify their insolubility [Galvez et al., 2002; Vander Wal et al., 2003; Palotas et al., 1996], whatever the solvent.

The nature of the crosslinking cannot be inferred by diffraction-based techniques since they image aromatic systems whereas do not "see" the possible sp^2, sp^3 bonding as well as the aliphatic functionalities. For instance, the sp^2 clustering degree of different carbons, estimated by optical band gap analysis [Llamas-Jansa et al., 2007] and temperature programmed oxidation method [Aso et al., 2004], have shown to be different from the size of aromatic layer (L_a) estimated by HRTEM analysis.

A good agreement has instead been found comparing the values of La estimated by Raman Spectroscopy and TEM taking into account the effect of layers curvature (Larouche et al., 2010). Moreover, the quasi-invariance of the fringe length as well as of the other BSU parameters (interlayer spacing, number of stacked layers) (Galvez et al., 2002; Alfè et al., 2009; Llamas-Jansa et al., 2007; Alfè et al., 2010) is not consistent with the strong variations of other structural properties (H/C, reactivity, UV–Visible and infrared features, etc.) observed for combustion-formed carbon material as a function of process conditions as temperature, fuel nature, etc (Russo et al., 2013a).

One of the major challenges of studying disordered carbons is, thus, to determine the appropriate spectral indicators to correlate with the nanostructure of these materials. Thus, even though HR-TEM is a powerful tool for analyzing the order of carbon materials, the use of other techniques, in conjunction with HR-TEM analysis, is necessary to understand the carbon structure and follow the structural transformations due to the change of the process synthesis conditions.

1.5 Aim and content of the thesis

The relationship between synthesis/combustion conditions and carbon properties such as size, chemical composition, optical properties and internal structural organization is fundamental in order to produce carbonaceous materials with tailored properties and to obtain experimental evidence for further improvements in the kinetic models for soot formation.

In this thesis work the properties of carbon materials synthesized in combustion processes, specifically in well-controlled premixed flames, were analysed in detail in order to get information on the complex, still undefined, structure of soot and on the effect of combustion parameters and chemical environment on the formation mechanism.

Advanced diagnostic tools have been developed and implemented on carbon particulate sampled in premixed flames burning different fuels in controlled sooting conditions. In particular, this thesis work has been also devoted to the upgrade and the exploitation of the diagnostic potentialities of spectroscopic methods as UV-Visible spectroscopy, FT-IR spectroscopy and Raman spectroscopy for the quantitative and qualitative characterization of carbon materials and their related micro- and nano-structure.

Microscopy (HR-TEM), solvent extraction and chemical analysis/separation methods as elemental analysis and chromatography have been also used to deeply characterize carbon materials.

In short, this PhD thesis is focused on the study of the structural characteristics of carbon particulate matter, synthesized in the well-controlled combustion conditions of a premixed fuel-rich flame, where it is possible to study the parameters affecting their formation and, consequently, controlling their features. In this context the main objectives of this thesis are: i) to explore the diagnostic potentialities of fast and non-destructive spectroscopic tools for carbon characterization, ii) to get a deeper understanding of the formation mechanism of carbon materials in flames with the perspective of controlling and modulating the properties of carbon materials obtained.

2 Spectroscopic characterization of Carbon Materials

The ternary phase diagram of the C-H system [Robertson, 1996; Ferrari et al, 2000] emphasises that two key parameters determine the structure and the properties of carbon materials: the fraction of sp^2-bonded carbon sites and the hydrogen content. Structural characterization of carbon materials focuses strongly on these two parameters. However, the ordering and clustering of sp^2 sites is a third significant factor, affecting the structural and the electronic properties. Various characterization methods have been developed to determine these structural parameters. Among them, the use of optical features have been in deeper investigated in the frame of this thesis.

2.1 Spectroscopy

Spectroscopy probes the interaction of electromagnetic radiation with matter in terms of absorption, emission and scattering of light.

These interactions can cause redirection of the radiation and/or transitions between the energy levels of atoms or molecules. Three main phenomena can be distinguished:

- Absorption: a transition from a lower level to a higher level with transfer of energy from the radiation field to an absorber;
- Emission: a transition from a higher level to a lower level with transfer of energy from the emitter to the radiation field;
- Scattering: redirection of light due to its interaction with matter. Scattering might or might not occur with a transfer of energy, i.e., the scattered radiation might or might not have a different wavelength compared to the light incident on the sample.

Different regions of the electromagnetic spectrum provide different kinds of information as a result of such interactions.

2.1.1 Absorption spectroscopy

When matter is exposed to optical light, the combined effects of absorption and elastic scattering (Rayleigh scattering) can cause a net loss of energy from the incident light beam and it is referred to as extinction. If a homogeneous mean is considered and the intensity of an incident monochromatic

radiation and the emerging radiation intensity are defined with I_0 and I, respectively, the total energy removed can be derived from the Lambert-Beer law:

$$\ln\left(\frac{I}{I_0}\right) = -K_{ext}(\lambda) * L$$

where K_{ext} is the extinction coefficient at the specific wavelength λ and L is the optic path. If a non-scattering homogeneous medium is considered, the Beer Lambert law can be simplified and the loss in intensity due to absorption, as light travels through the medium, is given by:

$$\ln\left(\frac{I}{I_0}\right) = -\varepsilon_{abs}(\lambda) * C * L$$

where ε_{abs} is the molar absorption coefficient at the specific wavelength λ and C is the molar concentration of the absorber. Thus the Beer-Lambert law states that the amount of light absorbed at a given wavelength depends to the properties of the material through which the light is travelling, the concentration of the absorbing species and the path length.

2.1.1.1 UV-Visible spectroscopy

The UV-visible absorption is caused by electronic transitions between bonding and anti-bonding orbitals. Since the σ states form very localized bonds, which determine a short range order, they are less sensitive to structural variations than the π states. In fact, the delocalization of the π electrons of the sp^2 clusters introduces a medium range order and determines a strong link between electronic and structural properties in carbons. Indeed electronic properties are controlled by medium-range order, specifically, the number of sp^2-bonded rings (Robertson, 1991) that are adjacent or clustered together. Only processes that affect sp^2 cluster size and quality can change the absorption properties. Thus, UV-Visible spectroscopy of carbon materials has shown to be a very powerful diagnostic tool for investigating their structural characteristic (Llamas-Jansa et al., 2007; Tomita et al. 2004; Mennella et al., 1995; Duley et al., 1998; Henning et al., 2004; Robertson et al., 1987; Robertson, 1991; Robertson, 2002; Galvez et al., 2002; Schnaiter et al., 2003; Jäger et al., 1999; Minutolo et al., 1996; Tregrossi et al., 2010; Schnaiter et al., 2006; Russo et al., 2012; Russo et al., 2013b) since optical properties are important signatures of their structure/composition. Combining information obtained by the analysis of specific optical parameters, as the UV-Visible maximum position, optical bang gap and mass absorption coefficient, it is possible to follow the evolution of aromatic clusters and get insights in the carbon structure.

UV-Visible maximum position

The $\pi-\pi^*$ transitions, due to sp^2 hybridization, provide an absorption band located in the UV-Visible range between 180 and 280nm (Llamas-Jansa et al., 2007]. A second band falling in the far UV toward 100nm is attributed to $\sigma-\sigma^*$ electronic transitions. The UV-Visible maximum position has shown to shift toward the visible as the sp^2 character increases, i.e. as the dimensional growth of the graphene sp^2 layers occurs (Llamas-Jansa et al. 2007; Tomita et al., 2002; Mennella et al., 1995). In particular Mennella et al. (Mennella et al. 1995) have clearly showed this effect performing UV-Visible spectroscopy on carbon samples produced by arc discharge and further annealed. As the annealing temperature increases the UV band shifts toward the visible and the band gap decreases, testifying that the sample has undergone to graphitization process that has led to an aromatic growth. However, during the graphitization/aromatization the increase of some other structural parameters as the number of stacked graphitic layers (Duley et al., 2002) and the curvature of aromatic layers (Henning et al., 20049 can cause the shift of the band position in the opposite direction, i.e. toward the UV region.

The extinction spectra of polycyclic aromatic hydrocarbon (PAH) molecules, with varying degrees of hydrogenation, ionization, and defects, have been calculated by Duley et al. (Duley et al., 2002), showing that as the number of stacked PAH increases, the UV band moves toward the UV region. The deviation from planarity of the graphene layers, due to an increase of odd member ring, is correlated with the formation of mixed hybridisation states through the deformation of the π bonds and the subsequent rehybridization of the carbon atom (Henning et al., 2004). This affects the electronic transitions between the π-orbitals which have no longer a pure π-orbital character and are now expected to occur in the UV range at higher energies.

Considering the structural parameters that influence this optical feature, UV-Visible maximum position has shown to be a useful proxy to get details on the carbon network structure in terms of sp^2 and sp^3 sites and size and arrangement of the aromatic units.

Band gap

Band-gap theory was first used by Tauc et al. (Tauc et al., 1966) to explain the absorption behavior of germanium. The optical gap is the energy required for an electron to reach the first excited state: the difference between the highest-energy occupied molecular orbital and the lowest-energy unoccupied molecular orbital. The absorbance A follows the Tauc relationship:

$$\sqrt{A*E} = B*(E - E_g)$$

where E is the energy of the incident radiation, B is a constant, and Eg is the optical gap. In practice, Eg is determined by plotting $\sqrt{A*E}$ as a function of E and extrapolating to zero absorption. According to the model developed by Robertson and Robertson and O'Really (Robertson et al., 1987) the decrease of the energy band gap measured on the visible tail of UV-Visible spectra of carbons based material is a good signature of the increase of aromatic system size that characterized the materials. The optical gap for benzene, with one ring, corresponds to a wavelength of about 200 nm. As adjacent rings are added, the optical gap decreases and photons of lower energy or longer wavelength can be absorbed. For material with many adjacent aromatic rings, the optical gap approaches zero. If the sp^2 sites form planar graphitic clusters, the band gap was found to be given by a simple relation:

$$E_g \approx \frac{6}{M^{1/2}}$$

where M is the number of sixfold rings in the cluster. However, this relationship is not longer valid for distorted clusters, since band gap is also controlled by the distortion of rings or chains, and the size of the clusters is no more related to the bang gap with the simple relation reported above (Robertson 1995; Robertson 1997; Robertson 2002; Lee et al., 1994). Even though the discrepancies between the calculated and measured structural parameters confirm that the model developed by Robertson and Robertson and O'Reilly fails to describe quantitatively the internal structure of disordered materials containing graphene layers with a variety of sizes and shapes (Llamas-Jansa et al., 2007), the band gap can still be considered a parameter for the qualitatively evolution and growth of aromatic clusters, as it decreases with increasing sp^2 size.

Mass absorption coefficient

The mass absorption coefficient is a measurement of how strongly a chemical species absorbs light at a given wavelength, per unit mass. Bond et al. (Bond et al., 2006) have provided a wide range of values for the absorptive properties of light-absorbing carbon, that is generally termed soot in combustion science and by the Intergovernmental Panel on Climate Change. These values mainly come from the extensive combustion literature on this topic and the variability of absorptive properties of carbonaceous particles can be attributed to the use of different combustion sources and operating conditions. Indeed, it has to be reminded that many morphological and physico-chemical parameters are known to affect in a complex manner the absorption coefficient and there is still a

big debate about the interpretation and reliable evaluation of absorption (extinction) coefficient of carbon materials (Bond et al., 2006).

Attempts to explain the absorptive properties of carbon by using elemental composition, mainly H/C (hydrogen-to-carbon) ratio, span several decades. Millikan (Millikan, 1961) reported changes in the absorptive properties of flame-generated carbon with H/C ratio. Since only processes that affect sp^2 cluster size and quality can change the absorptive properties, the role of sp^2 bonds and cluster size explains why H/C ratio is a reasonable, but imperfect proxy of absorption. Moderate annealing can be used to modify the sp^2 nanostructure almost independently of the sp^3 phase, this causes a change in the electronic and optical properties even though overall chemical composition remains constant (Chhowalla et al., 2000). The need to identify critical aspects of morphology, that affect absorption, drives to a systematic study on soot with different structural properties, produced and characterized with the same experimental methodology, to understand how the structure can influence mass absorption.

Since a reliable range of optical properties of soot particles will not be provided to climate models, scattering , absorption, and radiative forcing calculations will remain similarly uncertain.

2.1.1.2 FT-IR spectroscopy

Infrared spectroscopy detects the vibration characteristics of chemical functional groups in a sample. When an infrared light interacts with the matter, chemical bonds could stretch, contract and bend. As a results of this interaction a chemical functional group tends to absorbs infrared radiation in a specific wavenumber range almost regardless of the structure that surrounds it. Thus, the wavelength of light absorbed is characteristic only of the chemical bond whatever the sample. Because the strength of the absorption is proportional to the concentration, FTIR can be used for some quantitative analyses.

Briefly, in FT-IR spectra of carbonaceous materials one clearly distinguishes three main absorption regions. The high-frequency bands around 3000 cm^{-1} are due to the stretching vibrations of the C—H bond in its different configurations, while in the medium-frequency range the absorption of the carbon skeleton results in a broad combination of peaks between 1600 and 1000 cm^{-1}. A third group of bands is found, between 600 and 1000 cm^{-1}, characteristic of the aromatic C-H out-of-plane bending modes.

Regarding hydrogen bond characterization, FT-IR analysis of the C–H vibrational modes has considerable value for structural investigations due to the different nature of C–H vibrations in the 3200-2800cm^{-1} wavenumber range. Indeed, in this spectral region methyl C-H_3, methylene C-H_2

and methine C-H stretches arise together with aromatic C=C-H stretch, allowing to discriminate the presence of these different types of hydrogen (Dischler et al., 1983). Although elemental analysis can provide hydrogen content, more details on the carbon structure can be derived not only distinguishing the hydrogen bonds nature, but also quantifying the amount of aromatic and aliphatic hydrogen. To this regard to each C-H stretching mode corresponds a different absorption strength, thus the C-H bond stretch band has to be deconvoluted into its component absorption peaks and each peak multiplied by the appropriate absorption strength. Ristein et al. (Ristein et al., 1998) did this, using bond strengths derived from molecules. However, the absorption strength and position of methyl group has shown to be dependent even in simple molecules from the hybridization state of neighbour carbon atoms (Jacob et al., 1996, Ristein et al., 1998). This consideration has represented a stumbling block for the development of a procedure for the quantification of hydrogen content from FT-IR spectroscopy.

A more careful correlation between functional groups absorption features, in terms of peak shape, position, width, intensity, and the electronic configuration of their surrounding atoms should be investigated. In this way what was considered a drawback could become a sensitive tools giving indications about the neighbour molecular configuration in which the functional group are inserted. Thus, in this thesis work the diagnostic potentialities of FT-IR spectroscopy will be entirely exploited, and not solely limited to a qualitative identification of hydrogen bonds.

2.1.2 Raman spectroscopy

An additional phenomenon arising from the interaction of light with matter is the Raman scattering, a process having net effects of scattering photons, but changing their frequency. The difference in energy between the incoming and scattered photon corresponds to the energy difference between vibrational energy levels of the molecule. The different vibrational mode of a molecule can be thus identified by recognizing Raman shifts in the inelastically scattered light spectrum.

Raman spectroscopy of carbon materials is able to determine, through the determination of specific parameters, the short, medium, and long range bonding structure of disordered carbons, where short-range order refers to the hybridization level, medium-range order is mainly used to describe bonding structure in graphite-like materials (i.e., aromatic rings or others) and long-range order refers to the number of aromatic rings in a graphitic cluster.

A single crystal of graphite has a single Raman active mode, which is centred at 1580 cm^{-1}, labelled G band (Tuinstra et al., 1970). This band involves the in-plane bond-stretching motion of C sp^2 atoms. Thus, this mode does not require the presence of sixfold rings. It always lies in the range

1500–1630 cm^{-1} in aromatic and olefinic molecules. One of the most unusual properties of graphite is that the spectrum of micro-crystalline graphite materials shows additional peaks that are not observed in large single crystals. The first order spectrum of micro-crystalline graphite shows additional bands at 1350 cm^{-1} and 1620 cm^{-1} called D and D' respectively. These peaks arise due to the loss of long range in plane symmetry. The D peak is a breathing mode of C sp^2 aromatic atoms. Thus, this is strictly connected to the presence of sixfold aromatic rings. This mode is forbidden in perfect graphite and only becomes active in the presence of disorder. The D' peak is activated by lattice surface defects.

Tuinstra & Koenig (Tuinstra et al., 1970) showed that the D mode intensity increases linearly with decreasing size of graphite crystals L_a:

$$\frac{I(D)}{I(G)} = \frac{C(\lambda)}{L_a}$$

However, increasing the defects and reducing L_a below 2 nm, this relationship is no longer valid.

This can be explained remembering that the D peak needs both aromatic rings and disorder to arise. Starting from graphite, at a fixed λ, as the disorder is generated, the D peaks is activated due to the presence of aromatic rings in an imperfect crystalline structure, so I(D)/I(G) will increase with increasing disorder in a purely aromatic network according to Tuinstra-Koenig relationship. For more disordered carbon, clusters decrease in number and become smaller and more distorted; this corresponds to a loss in aromaticity and to the rise of disorder due to the presence of odd-member rings and chains. While the G peak is related to the motion of all sp^2 sites, the I(D) can not increase longer with respect to I(G) because one requirement for its rise, i.e. aromaticity, is disappearing. Disorder is so high that the number of rings per cluster is very low and the fraction of chain and/or odd member rings group rises so the Tuinstra-Koening relationship will not be longer valid. For small L_a, the D mode strength is proportional to the probability of finding a sixfold ring in the cluster, that is, proportional to the cluster area. Thus, in amorphous carbons the development of a D peak indicates ordering, exactly opposite to the case of graphite.

$$\frac{I(D)}{I(G)} = C'(\lambda) * L_a^{\,2}$$

The width of the G and D peaks also scales with disorder (Robertson, 2002). For a given cluster size, the width of the G peak is proportional to the bond-angle disorder at sp^2 sites. However, in amorphous carbon with an sp^3 content up to 10–20%, an increasing sp^2 content, even though not via an ordered sp^2 matrix, can cause a decrease of the gap and an increase in its FWHM (Ferrari et al., 2000).

On the basis of the G peak position two types of the materials can be discriminated. In materials with only sp^2 rings, the G peak position is located at 1580-1600 cm^{-1}. The increase of the sp^3 content up to 20% causes a decrease in the G position and its increase for sp^3 content higher than 20%. In those materials also containing sp^2 chains the G peak position is higher than 1600 cm^{-1} . This high G peak position can only be due to short C=C bonded chains, since C=C stretching vibration in ethylene is at 1630 cm^{-1}. This is a direct evidence of the presence of sp^2 chains in carbon materials. Thus, Raman can gives indications on sp^3 and sp^2 sites, and on the sp^2 sites in form of rings or chains. (Ferrari et al., 2000)

These observations regarding the change of the Raman spectra parameters with the structural evolution of carbon based materials have been summarized in the three-stage model proposed by Ferrari (Ferrari et al., 2000).

The amorphization trajectory discussed by Ferrari moves from relatively ordered carbons to disordered ones. What happens if an ordering trajectory has to be followed?

Examples of an ordering trajectory are deposition at high temperature, annealing after deposition, low-dose ion implantation of ta-C, or unfiltered deposition processes.

Following the amorphization trajectory there is a slight conversion of sp^2 in sp^3.

Generally, the sp^2 configuration varies consistently with the sp^2 fraction. During a room-temperature deposition, the sp^2 and sp^3 phases are linked together, forcing the sp^2 phase to evolve continuously with increasing sp^3 content. In other treatments, such as annealing or high-temperature deposition the sp^2 configuration can be changed independently on the sp^2:sp^3 ratio. These cases favour clustering of sp^2 sites into fairly-ordered aromatic rings and Visible Raman spectroscopy is much more sensitive to clustering than to conversion. This effect causes an hysteresis leading to a not unique relation between I(D)/I(G) or the G position and sp^3 fraction (Ferrari et al., 2000).

In Visible Raman spectra the cross-section of the sp^2 phase is much higher (50–250 times for 514.5 nm) than that of the sp^3 phase (Wada et al, 1980). Thus, the clustering and disorder of the sp^2 phase are the main factors affecting peak positions, width, and intensity. In principle, the sp^2 clustering can vary independently of the sp^3 content., this means that one visible Raman spectrum could correspond to various films with different sp^3 content. Since C-C sp^3 vibrations can be directly detected by UV Raman spectroscopy, combining a visible Raman spectrum with a UV Raman spectrum has shown to be helpful in resolving this problem (Ferrari et al., 2001).

In the frame of this thesis only the first order features, arising in the 1000-2000 cm^{-1} region, of combustion-formed carbonaceous species will be discussed and analysed because of the absence of well-defined second-order Raman peaks for this kind of carbons.

However, further informations regarding more ordered materials such as graphene, can be obtained from the second order region, where sharp peaks are present. The D peak overtone, the 2D peak, located at about 2700 cm^{-1}, has shown to change in shape, position and intensity with the number of graphene layers (Ferrari, 2007).

3 Synthesis of carbon species in premixed laminar flames

Considering the chemical complexity of combustion phenomena [Westbrook et al, 2005] along with the fluido-dynamic drawback characterizing real combustion systems, like engine, gas turbine, ecc.., laminar premixed flame is the experimental system chosen in many combustion laboratories.
The premixed flame offers great advantages in the study of flame structures for theoretical and modelling purpose. Indeed, a premixed laminar flame, in which fuel and oxidiser are fully mixed, eventually with an inert gas, prior to combustion, is a one-dimensional problem, where chemistry and transport are simplified allowing a relatively high experimental accessibility.
A premixed flame can be considered belonging to the family of plug flow reactors (PFR). This underlies a correspondence between spatial coordinate and residence time allowing to follow and determine the time scale of the processes involved. By changing operative conditions, it is possible to investigate the effects of parameters, such as temperature, equivalent air/fuel ratio (ϕ), fuel nature, residence time, etc., on the flame structure and on the formation, coagulation and growth of high molecular mass structures.
From the point of view of numerical techniques, computing laminar premixed flames is a first step toward more complex configurations, so experimental results are necessary for validation and development of detailed kinetic modelling of soot formation. In the frame of this thesis, fuel-rich premixed flames of methane, ethylene and benzene, as representative of fuel with different structure, have been investigated. Part of the experimental work was also devoted to the study of the temperature effect on soot structure for the three hydrocarbon fuels in one defined ϕ ratio condition. Joining together all the experimental results obtained, the effect of the fuel nature on soot structure produced in premixed flame, burning in similar sooting condition and in a narrow temperature range, has been investigated.

3.1 Premixed laminar flame model

The structure of a premixed laminar flame has been investigated in depth by Fristrom (Fristrom et al., 1965), who schematically divided it in four zones: unburned, preheat, reaction and burned gas zone. The unburned fed mixture delivered to the preheat zone, is warmed up by upstream heat transfer from the reaction zone. Preheat zone can reach temperature even higher than 1000K,

leading to a first mild fuel decomposition. In the reaction zone the fuel, partially decomposed/oxidized, is rapidly consumed according to the oxidiser content and the bulk of chemical potential is released. At such high temperatures the presence of a large radical and ions pool enhances the reaction rate. After this zone the main and stable gas already attain almost their maximum concentration while intermediate species usually steeply decrease. However, temperature is still high and, unburned fuel, light hydrocarbons, aromatic species and radicals radicals like OH, H are present,. In this region, the inception of soot particle starts in the so called "pyrolytic" zone. Operating with ϕ ratio higher than 1 even when oxygen is still present, unburned fuel and its fragments can attain so high concentrations that pyrolytic routes leading to soot precursors can be much more effective than the oxidative routes. The overlapping of the oxidation and pyrolytic zone is a crucial aspect in the interpretation of soot structure analysis.

3.2 Experimental apparatus

Premixed flames burning at atmospheric pressure of methane, ethylene and benzene were produced on a water-cooled sintered-bronze McKenna (Holthuis & Associates) burner (d=60mm). The flames were stabilized by a horizontal steel plate positioned about 30 mm height above the burner.

The burner can be used for the study of flames burning both gaseous and liquid fuels of high volatility. In the case of liquid fuels they are pre-vaporized and the cooling temperature of the burner is kept above the dew point of the fed mixture. The atmospheric-pressure laminar premixed flat flames operated on this burner can be considered one-dimensional reacting systems, so it can be assumed that the flame is completely described when the temperature and concentration profiles along the flame axis are known. The burner moves vertically in order to allow sampling and measurements at different heights above burner (i.e. at different residence times).

The main operating combustion parameters of each studied flame are reported in Tab. 1.

Flame label	Fuel	% fuel	% N_2	Φ	v_0, *cm/s*	Tmax		
						K	rt, *ms*	*HAB, mm*
LT-M	Methane	54.5		2.4	4	1650	12	2.2
HT-M		54.5		2.4	5	1770	9	2.2
LT-E	Ethylene	44.4		2.4	3	1620	19	2.5
HT-E		44.4		2.4	4	1700	9	1.7
LT-B	Benzene	5.7	72.7	2	3	1720	27	3.5
HT-B		5.7	72.7	2	4	1810	15	3

Tab.1 Operative conditions and main combustion parameters

The methane and ethylene flames were burned in oxygen at a fixed equivalence ratio $\phi = 2.4$. In the case of benzene flames it was necessary to operate in diluted conditions (72.7% N_2) and at a lower equivalence ratio (ϕ=2.0) in order to get stable flames with temperature conditions and soot yields rather similar to those obtained in methane and ethylene flames.
By changing the cold gas velocity, v_o, the flame temperature was varied of about 100K in the 1600-1800K range. Indeed, at higher cold gas velocity the heat loss toward the burner surface decreases (Kaskan 1956; Bohm et al., 1988), increasing the temperature.
The flames investigated in this thesis work, listed in Tab.1, are named with a label indicating the temperature and the fuel of the flame, e.g methane flame at lower temperature has been indicated with the acronym LT (lower temperature) M (methane).

3.3 Flame structure characterization

The structure of a premixed flame has been preliminarily determined by using non-intrusive techniques for the temperature measurement described in the following section.

3.3.1 Temperature measurements

Flame temperature was measured using a fast-response silica-coated fine wire Pt/Pt–13% Rh thermocouple: 100μm wires are joint to very short 25μm wires, which are used to realize a very small bead size of about 50μm. In this way the mechanical strength of the larger wires avoids any vibrations. Hence, the temperature profile can be considered quite unperturbed and a reliable reference for adjusting the axial coordinates of intrusive sampling data. A fast-insertion procedure was used to avoid massive soot deposition on the thermocouple bead and the consequent change of the bead size and of the emissivity of the thermocouple junction. Temperature was corrected for the radiative losses (Fristom et al., 1965). The correction can be estimated by equating the heat transferred to the probe from the gas to that lost by radiation:

$$2 * \frac{\lambda}{d} * \left(T_g - T_w\right) = \varepsilon * \sigma * \left(T_c^{\,4} - T_w^{\,4}\right)$$

λ = gas thermal conductivity
d = thermocouple bed diameter
Tg = gas temperature
Tc = temperature measured by thermocouple

ε = thermocouple emissivity

σ = Stefan Boltzmann constant

Tw = room temperature

The uncertainty of the measured temperatures was estimated to be as high as 100K.

3.3.2 In-situ extinction measurements

In-situ extinction measurements have been carried out along the flame axis by means of a 5mW He/Ne laser (λ=632.8nm) and a power meter equipped with a interferential filter to measure the intensity of laser radiation. Since PAHs and aromatic molecules mainly absorb only in the ultraviolet region while soot particles have a strong tail of absorbance in the visible range, using a 632 nm wavelength, is possible to neglect the rate of radiation absorbed by PAHs and condensed species present in the flame and consider the signal reduction due only to the soot absorption.
Once the initial intensity of laser radiation, I_o, is measured, when the flame is interjected, the extinction coefficient, K, can be evaluated as a function of the distance above the burner:

$$K(z) = \frac{1}{L(z)} * \ln \frac{I_o}{I(z)}$$

where L (z) corresponds to the diameter of the flame and I(z) is the radiation intensity measured at the selected height z. In the hypothesis that the radiation scattered and/or reflected from the flame is negligible the reduction of radiation intensity is due only to the soot particle absorption and K is proportional to the soot volume fraction.

3.3.3 Sampling procedure

Even though non-intrusive techniques provide the best reliability, a sampling procedure with intrusive probes is demanded to get insights in the chemical structure of the flame. The sampling mode has to be chosen or adapted in order to answer and fit the experimental needs. In the frame of this thesis, samplings have been realized through suction by an isokinetic probe or/and insertion into the flame of a quartz plate. Both techniques are intrusive and induce an interference on the thermal and fluid-dynamic flame fields, that can be quantified comparing the data with those obtained by non intrusive techniques.

3.3.3.1 Isokinetic-Probe sampling

Gaseous species and particulate, were sampled by a stainless steel, water-cooled, isokinetic probe (i.d. 2mm) inserted vertically into the flame as shown in Fig. 5. A 6-mm o.d. probe was used with a conical tip diameter of 3mm.

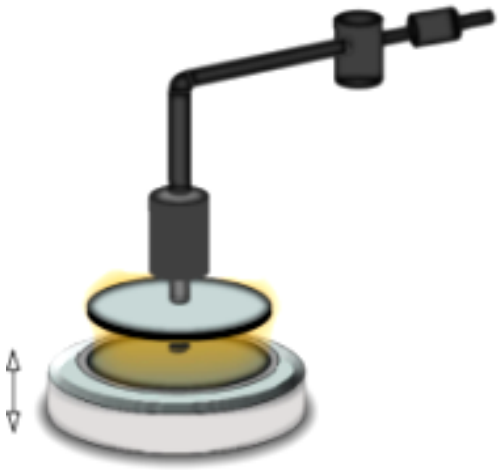

Fig. 5 Isokinetic Probe sampling

Stable gases (O_2, N_2, CO, CO_2, H_2 and C_1-C_6 hydrocarbons) were analyzed by on-line gas-chromatographic analysis. C_1-C_6 hydrocarbons were analyzed on an HP5890A gas chromatograph equipped with a 7515 Chrompack Al2O3/KCl capillary column and a flame ionization detector (FID). O_2, N_2, CO, CO_2, H_2 were analyzed by using a 8700 Altech coaxial column and a thermal conductivity detector on a HP5700A gas chromatograph.

The particulate is collected in an ice-cooled trap and on a teflon filter placed along the sampling line. To get enough amounts of particulate and to estimate reproducibility, each sample was taken from the flame at least thrice and the samples get together for further analysis. The uncertainty on the measured concentrations due both the sampling and analytical procedure was less than 10% at the end of the flame and about 25% at low height above the burner within the main reaction zone. To account for the probe interference on the thermal and fluid-dynamic flame fields, species concentration profiles were shifted upstream by placing the maximum of CO concentration in correspondence of the maximum temperature position. Since operating with ϕ greater than 1 the maximum heat release in the reaction zone should correspond to the partial oxidation of the fuel, i.e. to the maximum concentration of CO.

Probe sampling mode is long time consuming, but allows to obtained massive amount of particulate for chemical and spectroscopic characterization and moreover provide a complete description of the flame structure in terms of species, both gaseous and solid, concentration.

3.3.3.2 Quartz plate insertion

As shown in Fig.6, the total particulate matter has been caught on quartz plates inserted horizontally in the flame for the minimum time (400ms for the ethylene flames and 600ms for the benzene and methane flames according to the soot tendency of each flame) required both to collect a sufficient material for the further characterization and to limit the thermal degradation of the deposited sample at flame temperature (Tregrossi et al., 2010).

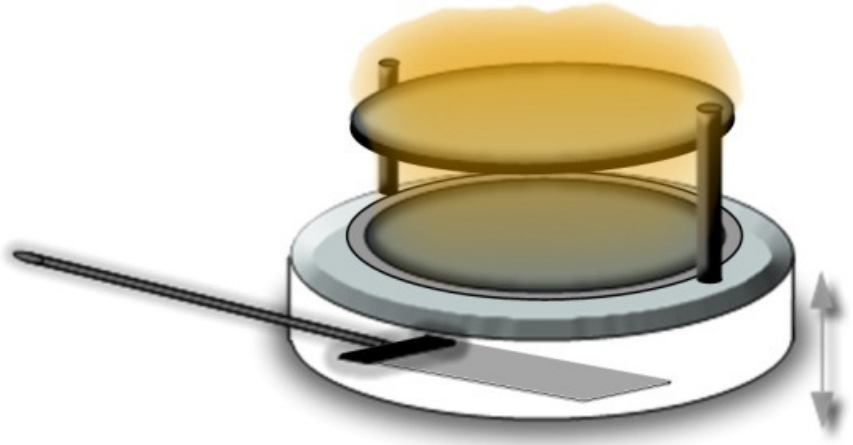

Fig. 6 Quartz plate insertion

While the lower face is used to sample the material inside the flame, the upper one is protected by a glass plate in order to avoid the collection of particulate coming from flame heights above the sampling point.

While in the case of isokinetic sampling particulate is distributed along the sampling line and need to be recovered with a solvent, in this case all the sample is deposited on the quartz plate forming an homogeneous thin film.

The need to exploit all the diagnostic potentialities of UV-Visible spectroscopy has been the driven reason for the development and optimization of sampling by deposition. Quartz is transparent in the UV-Visible range so that the absorbance spectra of the sample deposited on the plate can be measured down to the ultraviolet region, usually forbidden by solvent interference, providing important optical features for the structural characterization (position of UV bump, paragr. 2.1.1.1).

The interference of the sampling can be evaluated comparing and according the extinction profile at 632nm with the absorbance profile of all the collected material at the same wavelength. Quartz plate insertion directly into the flame can not provided enough material for chemical analysis of particulate, but it is particularly suitable for measurements of UV- Visible and Raman spectroscopy on a a homogeneous thin film deposited on suitable support material.

3.3.4 Sample treatments

Combustion-formed carbon particulate is constituted of many components different in size, structure and composition. Carbon particulate matter derived from combustion is characterized by a polydisperse size distribution in a wide size range, up to hundreds of nanometers, it is thus necessary to separate the contribution of species having different size and composition to shed some light on the their properties.

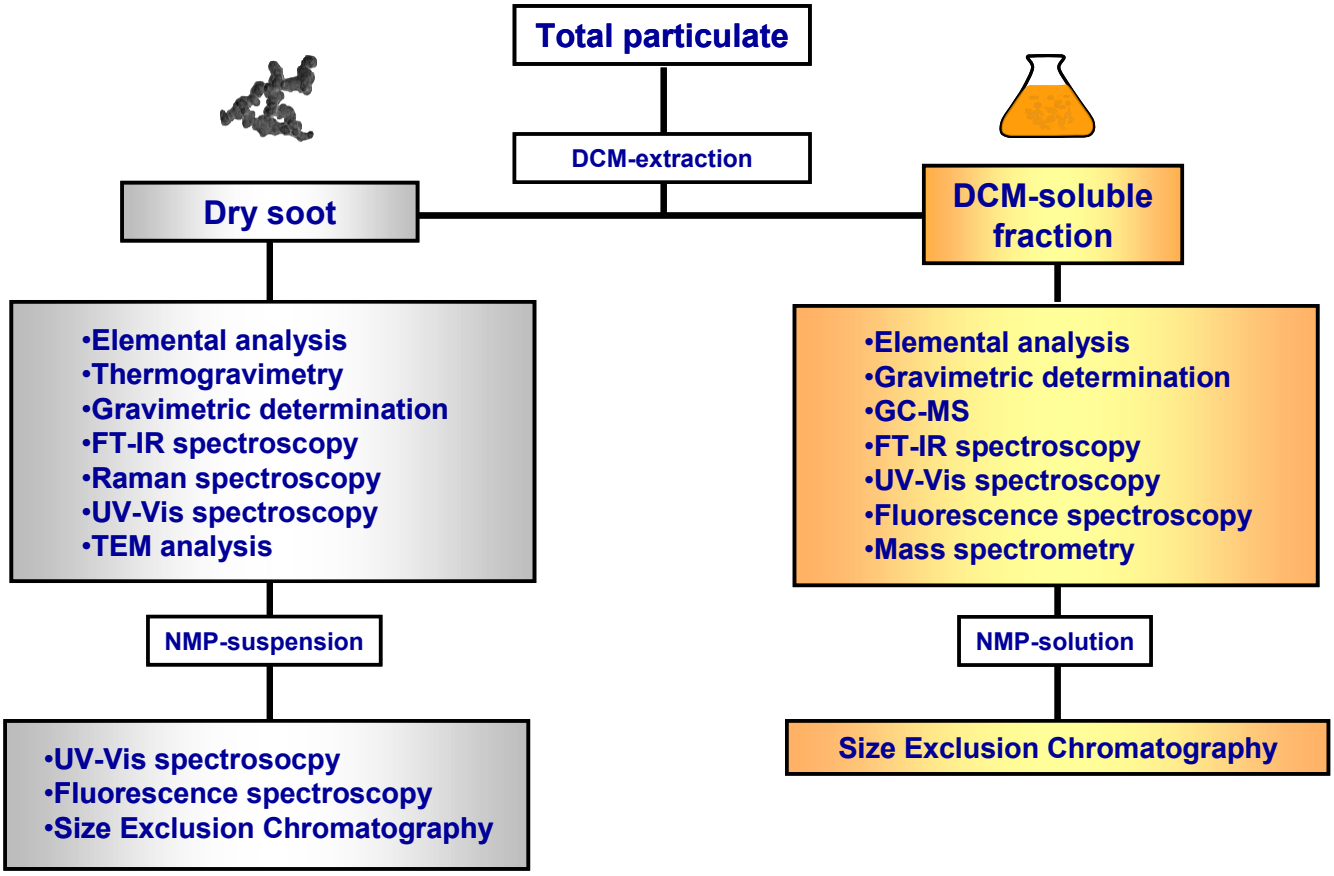

Fig.7 Analytical scheme of carbon particulate matter characterization

Whatever the sampling mode, a first partitioning is obtained by DCM extraction in two fractions, dichloromethane (DCM)-soluble and dry soot fraction.. DCM-soluble fraction is composed of low-

MW species from 100 up to 1E6 u. Both fractions have been analysed with different diagnostic tools, summarized in Fig.7, to get insight in their structure and composition.
The DCM-soluble fraction, dried under vacuum, and soot were weighed and divided by the total volume of gases sampled by isokinetic sampling technique, in order to obtain their concentration profile along the flame. Further separation in narrower MW range fractions has been obtained via Size exclusion Chromatography (see. 3.3.5.2).

3.3.5 Diagnostic techniques

The spectroscopic diagnostic tools used in this thesis have been deeply described in chapter 2. Experimental details about them are described in this section.
Additional diagnostic tools have been used to support the interpretation and the assignment of optical results for resolving the "puzzling" problem of combustion-formed carbon particulate in terms of its size, structure and composition..

3.3.5.1 Gas chromatography-mass spectrometry

Species with molecular masses up to 300u, belonging to the DCM-soluble fraction, were identified by gas chromatography/mass spectrometry (GC-MS) on an HP5890 gas chromatograph equipped with an HP-5MS crosslinked 5% PhMe siloxane 30m x 0.25mm x 0.25μm film thickness column coupled with an HP5975 mass spectrometer with an electron impact/chemical ionization ion source. The species identification was made by comparison with mass spectrum in Wiley computer library with 138.000 spectra.
GC-MS analysis allowed to distinguish three main classes of molecules inside the DCM-soluble fraction: PAH, substituted aromatics (such as phenylacetylene, styrene) and oxo-aromatic compounds (such as substituted phenols, benzaldeyde and benzofurane).
PAH have been quantified individually by using the factors response of standard mixtures of twenty-five PAH. For an approximate quantification of some substituted-PAH and oxo-aromatic species a mean response factor of the standard PAH mixture and of phenol has been used, respectively. In this way also the concentration of the heavier compounds can be obtained by difference between the concentration of the DCM-soluble fraction, obtained by gravimetric determination, and of species with a MW lower than 300uma, obtained by GC-MS analysis.

3.3.5.2 Size exclusion chromatography

Size Exclusion Chromatography (SEC) was carried out for the evaluation of the molecular weight (MW) distribution of the DCM-soluble fraction and dry soot.
SEC is a chromatographic method that allows separating molecules in a solution according to their size (namely, their hydrodynamic volume). Particles of different size elute through a stationary phase, usually a column filled with particle of a porous solid, at different velocities. The different elution times are related to the volume that the analyte can cross: a very large molecule can cross only the inter-particle volume so it elutes soon while a small molecule can penetrate also inside the pores and elutes later.
A HP1050 High Pressure Liquid Chromatograph (HPLC) using N-methyl-2-pyrrolidone (NMP) as eluent was used for the SEC analysis. The HPLC was equipped with a Diode Array Detector able to measure on-line UV-Visible spectra of the MW-segregated fractions from 250nm up to 600nm. SEC calibration curve for MW evaluation has been based on polystyrene standards (PS) and on carbonaceous samples whose MW has been evaluated from the measured Dynamic Light Scattering particle diameter considering a density of 1.8g/cm^3 and spherical shape (D'Anna et al., 2009).
The MW distribution of dry soot and DCM-soluble fraction was measured in a wide MW range (1E5-1E10u) by using a 30cm*7.5mm o.d. Jordi Gel divinylbenzene Solid Bead "non-porous" column (injection volume of 10µl, flow rate 1ml/min, room temperature). However, on this "non-porous" column the lighter and more abundant PAH components of the DCM–soluble fraction eluted as a single peak below the permeation limit of this column (1E5u) not allowing a reliable MW separation/determination. Thus, a highly cross-linked "individual-pore" (30cm*7.5mm o.d.) PL-gel polystyrene/divinyl benzene column (injection volume of 250µl, flow rate 0.5 mL/min, temperature of 80°C) was used to get the MW distribution of the DCM-soluble fraction in the 100-1E5u range. Size exclusion chromatography not only provide the MW distribution of the DCM-soluble fraction and dry soot but also physically separate their corresponding MW segregated fractions, that can be recovered and further analysed.

3.3.5.3 Atmospheric pressure-laser-desorption ionization-mass spectrometry

Generally speaking, mass spectrometry works by ionizing chemical compounds to generate charged molecules or molecule fragments and measuring their mass to charge ratio. Atmospheric pressure–laser desorption ionization–mass spectrometry (AP–LDI–MS) has the advantage of minimizing the possibility of fragmentation of molecules with respect to the LDI–TOF–MS in which the ion source

is operating at low-pressure. Avoiding massive fragmentation AP–LDI–MS mass spectra are more representative of the MW distributions of carbonaceous mixture. To perform the AP–LDI–MS analysis of the MW-segregated fractions of the DCM-soluble fraction separated by SEC elution in NMP, it was necessary to change the high boiling NMP solvent with a volatile solvent as DCM through liquid-liquid extraction. The samples have been placed on the AP–LDI target plate and heated at 80°C for 15 min in order to ensure the complete evaporation of residual NMP. The intensity of the nitrogen laser (337nm) used for desorption/ionization was about 200 μJ/pulse. A typical analysis consisted of 100–150 co-added spectra collected on the whole spot surface (1–2mm in diameter) in order to average the sample non-homogeneity effect.

3.3.5.4 Elemental and thermogravimetric analysis

Thermogravimetric analysis (TGA) is commonly employed to determine characteristics of materials and multicomponent systems, such as thermal and oxidative stability and moisture and volatiles content. It measures the amount and rate of change in the weight of a material as a function of temperature or time in a controlled atmosphere. Thermogravimetric analysis of soot was carried out on a Perkin–Elmer Pyris1 Thermogravimetric Analyzer in oxidative environment (air, 30ml min-1) from 30°C up to 850°C at 10°C min-1 heating rate.
H/C atomic ratio was measured on a Perkin–Elmer 2400 CHNSO elemental analyzer.

3.3.5.5 High-resolution transmission electron microscopy

High-resolution transmission electron microscopy allows imaging directly the ordered part of the structure of amorphous carbons. Advantages and drawbacks of this technique have been already discussed in paragr 1.4. The measurement were carried out at the Laboratoire de Geologie - Ecole Normal Superieure (CNRS, France) under the supervision of Dr. Jean-Noel Rouzaud.
Soot samples were dispersed in methanol by ultrasonic agitation and dropped onto a carbon lacey grid (20-nm thick carbon coated Cu grids, Spi Supplies). HRTEM in lattice fringe mode was performed on the soot samples using a JEOL 2011 electron microscope operating at 200 kV equipped with a LaB6 filament (resolution in the lattice fringe mode 0.144 nm).
The lattice fringe analysis of the HR-TEM images (magnifications of 500,000X) was exploited to obtain a semi-quantitative evaluation of the soot graphitic layers organization [12, 14, 20]. The lattice fringe analysis was performed on 15-20 images representative of the best structured areas. The number of the analyzed fringes was more than 3000 for each soot sample.

The fringes length, L, was individually measured by considering that a layer could be curved until to a distortion ratio arbitrarily fixed at 40%. L was evaluated by considering all the fringes larger than the size of one aromatic ring (L > 0.246 nm) and all the fringes larger than the size of two fused aromatic rings (L > 0.49 nm). Coherent domains, defined as stacks of N parallel planes were analyzed. The planes are considered stacked when the fringe disorientation is lower than 15% and the distance between fringes is lower than 0.6 nm. The pairs which do not fulfil these conditions are counted as 'non stacked' layers (nsl). La and Lc, corresponding respectively to the diameter and to the height of the coherent domains formed by N stacked layers with an interlayer spacing of d were measured. The calculated standard deviation in the distribution of individual paracrystalline layer spacings was 0.15 nm.

3.3.5.6 Fluorescence Spectroscopy

Fluorescence spectroscopy is an useful diagnostic tool to evaluate polycyclic aromatic hydrocarbon in complex PAH mixture (Lee M.L. et al. 1981).

When an incident light at a suitable wavelength is absorbed by a molecule, the electronic state of the molecule changes from the ground state to the one of the several vibrational levels of the excited electronic state, usually the first excited singlet state, S1.

The fluorescence corresponds to the relaxation of the molecule from the singlet excited state to the singlet ground state with emission of radiation. The fluorescence lifetime is about ~10-8 sec.

Generally speaking, the fluorescence spectrum of PAH mixture excited in the UV region shows two main spectral region: the first one from 300 to 350 nm due to two- and three-ring PAH, and a second one between 350 and 500 nm mainly due to four- and five-ring PAH. (Berlman, 1971). Synchronous fluorescence simplifies the conventional emission spectrum of aromatic mixtures, because each peak corresponds roughly to single components or class of components, offering the possibility of a multicomponent analysis of complex PAH mixtures (Vo-Dinh, T., 1978).

Synchronous fluorescence spectra and fluorescence emission spectra ($\lambda exc = 350nm$) of the DCM-soluble MW segregated fractions were measured in standard 1-cm path-length quartz cells on a Perkin-Elmer LS-50 spectrofluorimeter. In synchronous fluorimetry excitation and emission wavelengths were simultaneously changed and a signal is observed only when $\Delta\lambda$ matches the interval between one absorption band and one emission band. A relatively small $\Delta\lambda$ would favours the emissions from aromatic structures with strong 0–0 transitions, whereas a relatively large $\Delta\lambda$ appears to favour the fluorescence detection of aromatic structures without strong 0–0 transitions

[Lì et al., 1994]. Based on the results from trial experiments, a Δλ of 20 nm was chosen as a good compromise [Apicella et al. ,2004].

3.3.5.7 UV-Visible spectroscopy: experimental details

Ultraviolet-Visible spectra were measured on a HP8453 spectrophotometer. The UV-Visible spectrum in the 190-1100nm wavelength range of the carbonaceous species deposited on the quartz plate was measured before and after dichloromethane (DCM) treatment in order to obtain, respectively, the spectrum of total carbon particulate and dry soot devoid of the DCM-soluble fraction.

UV-Visible spectra of the DCM-soluble fraction have been measured in standard 1-cm path-length quartz cells. The UV absorption of DCM limited the spectra acquisition of the DCM-soluble fraction to the 250-1100nm wavelength detection range.

Additional UV-Visible spectra of DCM-soluble fraction and soot MW-segregated fractions from 250 to 600nm have been provided by SEC coupled with Diode Array Detector.

Soot from isokinetic sampling was dried and weighted, and then suspended in N-methyl-2-pyrrolidinone (NMP) in order to measure the UV-Visible spectra beyond the 260 nm limit of NMP absorption in standard 1-cm path-length quartz cells.

3.3.5.8 FT-IR spectroscopy: experimental details

FT-IR analysis was performed on a Perkin-Elmer 1600 FT-IR spectrophotometer.

FT-IR analysis focused in the 3300-2700cm^{-1} range was carried out on solutions of known concentration (100ppm) of standard species and CS dissolved in carbon tetrachloride that is a solvent transparent in this wavelength region.

FT-IR analysis in the 3400-600cm^{-1} range of solid standard and carbon materials were made on sample dispersions prepared by mixing and grinding the samples in KBr pellets (0.25-0.5 wt %). The KBr dispersions were compressed at 10Ton for 10 minutes into a thin disks. For liquid analysis a cell with an optical path of 1 cm has been used, while for KBr disk a mean value of 0.035 cm (standard deviation of 15%) was measured.

The experimental error is higher for the solid spectra due to the uncertainty of the evaluation of the disk thickness and to the water absorbed on KBr responsible of a peak around 3200 cm -1 which renders more difficult a right evaluation of stretching peak height due to the imperfect baseline determination.

The experimental error is less then 10% for liquid solution and around 20% for KBr dispersion.

3.3.5.9 Raman spectroscopy: experimental details

Raman spectroscopy has been performed at the Nanomaterials and Spectroscopy Group of the Electrical Engineering Department of Cambridge University (UK) under the supervision of Prof. Andrea Carlo Ferrari. Raman spectroscopy has been performed on soot sampled on quartz plate after DCM treatment.

Micro Raman spectra are acquired with a Renishaw 1000 at 457nm, 514nm, 633nm using a 100X objective and less than 1 mW on the sample. Raman spectroscopy with an excitation wavelength of 244nm has been also performed with a 40X objective.

4 Experimental Results

4.1 Flame structures characterization

An overall description of the structure of the flames studied in this thesis is reported in Figs. 8 and 9, where the axial profiles of flames temperature and yields of soot and extract of soot in dichloromethane (DCM-soluble fraction) are reported. The methane and ethylene flames were burned in oxygen at a fixed equivalence ratio Φ= 2.4. In the case of benzene flames it was necessary to operate in diluted conditions (72.7% N_2) and at a lower equivalence ratio (Φ=2.0) in order to get stable flames with temperature conditions and soot yields rather similar to those obtained in methane and ethylene flames. By changing the cold gas velocity, v_o, [Bohm et al., 1988] the flame temperature was varied of about 100K in the 1600-1800K range, as reported in Fig.8. In these conditions the temperature was observed to steeply rise up to the peak temperature located between 2 and 4mm height above the burner (HAB). Due to the different velocity and temperature conditions it can be noted that at similar HAB correspond significantly different residence times (rt) also reported in Tab.1. For this reason a more reliable comparison between the flame structures has been done in terms of residence time evaluated on the basis of the velocity and flame temperature.

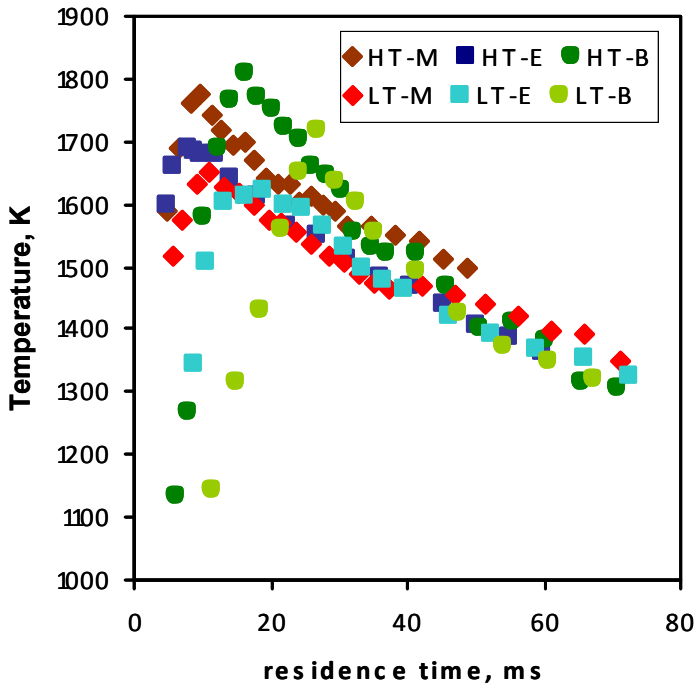

Fig 8 Temperature as a function of residence time for benzene, ethylene and methane flames

In Fig.9 (right part) it can be observed that soot begins to appear just after a few tens of milliseconds, steeply reaching the maximum concentration value at about 30-40 ms in all flame conditions, except for the low temperature ethylene flame (LT-E). In this flame soot profile displaces at longer residence times due to the lower flame temperature/cold gas velocity conditions. The final maximum soot concentration varies in a relatively small concentration range: from 4 (for methane and benzene flames) to 10 mg/NL (for ethylene flames), for effect of the different carbon feed concentration and temperature conditions as well as of different fuel sooting tendency. It is worth to note that soot inception in ethylene and methane flames occurs just after the end of the main reaction region, where oxygen is completely depleted. In benzene flames soot inception occurs at the end of the main reaction region, where significant amounts of unburned oxygen are still present (about 3-6 vol%).

The sooting structures of the investigated flames are compared in the right part of Fig. 9 where soot yields in relation to the fed carbon, are reported as a function of the residence time.

Soot yield profiles follow similar increasing trends along the flames and reach a quite constant value after some tenth of milliseconds. The maximum soot yield spans from a minimum value of 0.01 to about 0.035 in dependence on the fuel and temperature level. In particular, methane at higher temperature (HT-M) exhibits the lowest sooting tendency, whereas benzene at lower flame temperature (LT-B) shows the highest sooting tendency. These findings are in agreement with the well-known larger soot propensity of benzene in respect to other aliphatic fuels and with the effect of the temperature decrease causing the increase of soot yield in high temperature premixed flames [Bohm et al., 1988].

It is worth to note that, preceding and accompanying soot formation, DCM-soluble fraction yield profiles, reported in the left part of Fig. 9, follows increasing trends for methane and ethylene flames as soot is formed attaining to a constant value at the end of the soot formation region [Alfè et al., 2010; Ciajolo et al., 1996]. In Fig. 9 the peculiar benzene flame structure is also well depicted, with the oxidation and precursor mixture region well separated from the soot formation region, as observed in previous work [Tregrossi et al., 1999; Russo et al., 2012]. Indeed, DCM-soluble fraction, mainly constituted of both PAH and oxygen aromatic compounds, is rapidly formed and constitute the predominant component of particulate in the main reaction region. DCM-soluble fraction components undergo in this region an almost complete depletion, before soot inception and growth occur.

Such a sharp distinction between the DCM-soluble fraction and soot formation regions can not been generally observed in fuel-rich premixed flames of aliphatic fuels where DCM-soluble fraction and soot are formed together in the post-flame region.

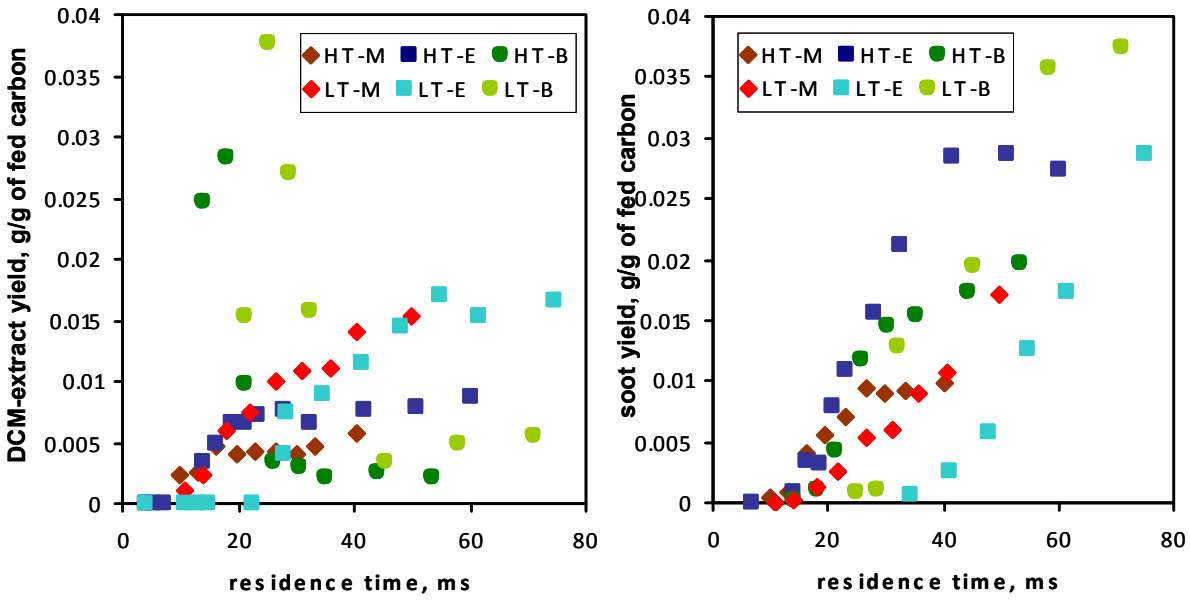

Fig. 9 DCM-soluble fraction (left part) and soot (right part) yields as a function of residence time for benzene, ethylene and methane flames

4.2 MW-segregated fractions characterization of DCM-solubles and soot

The main problem related to the detailed characterization of the combustion-formed carbonaceous species is due to the complexity of their polydisperse size distribution, spreading in a wide size range, up to hundreds of nanometers. The solvent extraction of carbon particulate with DCM allows separating the DCM-soluble fraction, characterized by a relatively low molecular weight range, from the high-MW carbon particulate fraction. However, the conventional chromatographic/mass spectrometric analysis fails to fully analyse even the DCM-soluble fraction due to the presence of a complex matrix of high-MW polymeric aromatic species beside the PAH. Other diagnostic tools are thus necessary for their structural characterization.

The UV-Visible absorption has shown to be a very powerful diagnostic tool for investigating the structural characteristic of carbonaceous species, not amenable for conventional analysis (see 2.1.1.1). By combining information obtained by the analysis of specific optical parameters, as the UV-Visible maximum position and the optical band gap, it is possible to get insights in the structure and carbon network of combustion-formed particulate matter and their analogues.

The optical band gap has been used in a pioneering work by Minutolo et al. (Minutolo et al. 1996) extending the evaluation of the optical gap (E_g) down to the whole UV-Visible region of the

extinction spectra measured on soot particles inside fuel-rich premixed flames of benzene. By this approach the contribution of different size classes of absorbers has been found, demonstrating that the polydisperse size distribution can be in some way inferred, provided that the contribution of species having different size and composition is taken into account for.

Schnaiter et al (Schnaiter et al., 2006) performed the spectral analysis on stage-separated components showing that to different size components correspond different absorption properties. On the basis of Size Exclusion Chromatography coupled with on-line UV-visible spectroscopic analysis, specific features of the Eg and maximum absorption position of spectra of carbon species deposited in methane flames, have been attributed to classes of different MW (Tregrossi et al., 2010).

Llamas-Jansa et applied a deconvolution to carbon black absorption spectra to determine the strength of $\pi-\pi^*$ and $\sigma-\sigma^*$ electronic transitions (Llamas-Jansa et al., 2007). All these approaches have been used as starting point for the development of a reconstruction procedure to evaluate the optical band gap and the UV peak position of the different MW-segregated fractions separated from combustion-formed carbon species. This procedure has been applied to both DCM-soluble fraction and soot in B-LT and E-HT flames. The UV-Visible spectral analysis regards carbonaceous species deposited in the flame just after soot inception (low residence time, LRT) at the minimum residence time required to collect sufficient material for the further characterization and at the end of the flame (high residence time, HRT). At LRT the interval timing from soot inception Δt is the same in both flame (17ms).

4.2.1 MW-segregated fractions of DCM-solubles

DCM-soluble species were separated in selected MW fractions by SEC and also analysed by fluorescence emission spectroscopy and by laser desorption ionization–mass spectrometry (LDI–MS) for determining their aromatic character/composition. These techniques have been performed in order to validate the attribution of some spectral features as obtained by the reconstruction procedure to specific chemical characteristics, validating the reconstruction procedure itself. The experimental results are consistent with the output of the reconstruction procedure and provide significant experimental evidence to give insights in the evolution of carbonaceous species from Polycyclic Aromatic Hydrocarbons (PAH) to soot nuclei and finally to soot aggregates, and corroborate the strong influence of the chemical environment in which soot precursor are formed on the evolution of the graphitization process.

The typical MW distribution of the DCM-soluble fraction, obtained by SEC analysis and reported in Fig.10, shows three main peaks corresponding to the 200-500u, 500-2000u and 1E5-1E7u MW-segregated fractions named P1, P2 and P3a. It is worth to underline that the MW distribution, obtained by SEC analysis, did not show significant differences in both position and width of the peak comparing the benzene and ethylene DCM-soluble fraction MW distribution. Only a slight shift of the P1 peak position toward lower MW (about 20u) was observed for the benzene samples.

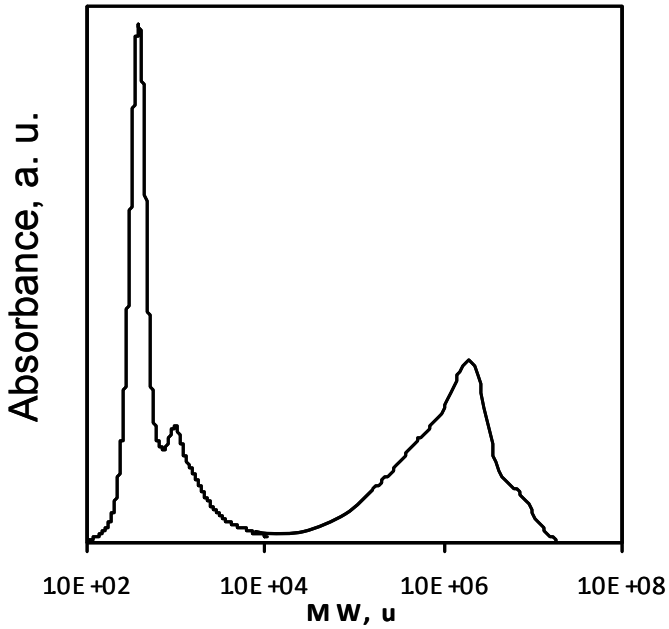

Fig.10 MW distribution obtained by SEC for HT-E LRT DCM-soluble fraction

4.2.1.1 Optical Band Gap Analysis of MW-segregated fractions of DCM-solubles

On the apex of the P1, P2 and P3a peaks, the UV-Visible spectra, named S1, S2 and S3a, are measured by UV-Visible diode array system from 290 to 600 nm. It is worth noting that the on-line spectra measured in different points of each peak, even in the case of the broader P3a peak, did not show significant differences both in terms of spectral features and optical band gap. Thus, to each peak can be associated a MW-segregated fraction constituted of species having similar optical characteristics. By consequence, the spectra measured on the maximum of each peak have been considered for inferring structural information on each MW-segregated fraction.

RT, ms	Δ_t from soot inception, ms		DCM soluble fraction		
			S1 [200-500u]	S2 [500-2000u]	S3a [10E5-10E6u]
LT-B LRT		Eg, eV	2.2	2.2	1.3
42	17				
HT-E LRT		Eg, eV	2.0	2.0	1.3
32	17				
LT-B HRT		Eg, eV	2.3	2.1	1.4
74	49				
HT-E HRT		Eg, eV	2.0	2.0	1.3
60	45				

Tab. 2 Band gap of the DCM-soluble MW-segregated fractions for the LT-B and HT-E flame at LRT and HRT.

Table 2 reports the optical band gaps evaluated on the spectra of MW-segregated fractions of the DCM-soluble fraction. Consistently with the increase of MW going from the P1 to the P3a peaks, it can be seen that the optical band gap decreases from the maximum value of 2, typical of PAH molecules, to the minimum value of 1.3. The spectra S1-S2 of adjacent P1-P2 peaks present the same optical band gap, (Eg~2) typical of 4 up to 10-ring pericondensed PAH. This indicates that in the 200-1E4u MW range the same aromatic moieties are present connected together for giving species with higher MW, but in a such way that they do not electronically interact each other. On this basis, it has been suggested that the peak P2 is composed of clusters/aggregates of P1 aromatic molecules (Sirignano et al., 2010).

The P3a species lie in the 1E5-1E6u MW range and the optical band gap (about 1) evaluated on the S3a spectrum is typical of aromatics with about twenty condensed rings. It has to be excluded that aromatic species with a 1E5-1E6u MW are composed of large-size graphitized PAH since they should be insoluble in DCM.

4.2.1.2 UV-Visible maximum absorption position of MW-segregated fractions of DCM-solubles

The position of the UV maximum absorption is, along with the optical band gap, another spectral parameter important for defining the internal structure of carbonaceous species (see 2.1.1.1).

Because of the interference of the DCM solvent absorption in the UV (up to 260 nm), the UV maximum position cannot be measured on the DCM-soluble fraction, but it has to be determined on

the spectrum obtained by difference between the spectra measured on the quartz plate before and after DCM treatment. Thus, a reliable spectrum of the DCM-soluble fraction has been obtained by joining at 290nm the spectrum obtained by difference from 190 up to 290 nm and the spectrum of the sample dissolved in DCM from 290 up to 600 nm. Also the UV maximum position of the MW-segregated fractions could not be determined owing to the UV interference, down to the 290 nm wavelength, of the NMP, used as solvent and eluent for the SEC analysis. Thus, on the basis of the DCM-soluble fraction spectra, a deconvolution procedure, reported in the following, has been developed for evaluating both the contribution and the position of the maximum absorption of each MW-segregated fraction in the whole 190-600 nm range.

The spectra were reconstructed using the following step by step procedure:

i) In the range 290-600nm the linear combination of the spectra measured on the P1, P2, P3a peaks for DCM-soluble fraction has been performed minimizing the root-mean-square deviation to get the reconstruction of the spectrum of DCM-soluble.

ii) In the range 190-290nm the spectra were reconstructed by using a Gaussian function in the energy domain, using the equality of the absorbance and of the first derivatives values at 290nm as junction conditions with the spectra measured in the 290-600 nm range. The Gaussian functions have been chosen since, in the energy domain, they take into account for statistical phenomena such as the electronic properties of carbon materials (Llamas-Jansa et al., 2007). For the spectra S1 and S2, presenting the fine structure typical of PAH, the first derivative in the 290-600nm was calculated on the continuum background of the spectra.

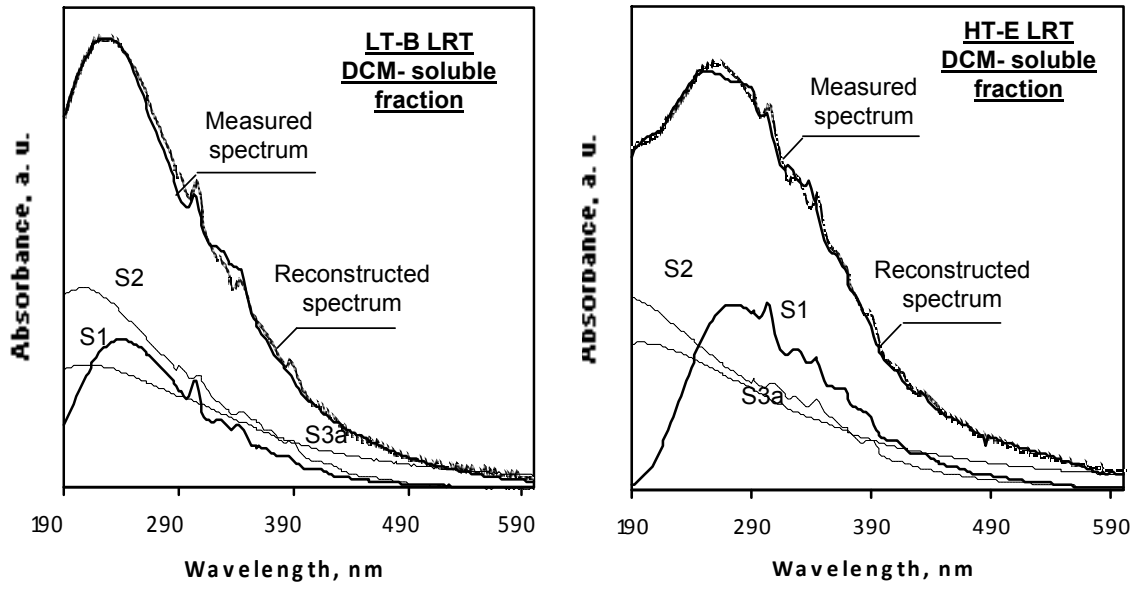

Fig. 11 UV-Visible spectra of the DCM-soluble fraction sampled at LRT in LT-B (left part) and HT-E (right part), in comparison with the output reconstruction procedure.

The typical output of the reconstruction procedure, used for getting the spectra in the whole UV-Visible range (downward to 190nm), is given in Fig.11, reporting the UV-Visible spectra of the DCM-soluble fraction measured for the benzene and ethylene sample at low residence time in comparison with the reconstructed spectrum and the spectra of the relative MW-segregated fractions.

RT, ms	Δ t from soot inception, ms		DCM soluble fraction		
			S1 [200-500u]	S2 [500-2000u]	S3a [10E5-10E6u]
LT-B LRT					
42	17	λ (Amax), nm	240	206	211
HT-E LRT					
32	17	λ (Amax), nm	273	<190	200
LT-B HRT					
74	49	λ (Amax), nm	247	204	222
HT-E HRT					
60	45	λ (Amax), nm	276	<190	200

Tab.3. UV peak position of the DCM-soluble MW-segregated fractions in the LT-B and HT-E flame at LRT and HRT.

The maximum absorption positions of the MW-segregated fractions spectra as evaluated from the reconstruction procedure are reported in tab.3 for the DCM-soluble species sampled at low (LRT) and high (HRT) residence times in the benzene and ethylene flames. The maximum absorption position for the benzene at about 240nm appears to be shifted toward lower wavelengths in comparison to ethylene (about 270nm). Considering that the spectrum is relative to the 200-500 u fraction, mainly constituted of PAH, this means that the PAH formed in the benzene flame are smaller in comparison to the ethylene flame [Wasserfallen et al., 2006; Fetzer, 2000]. Consistently with this result, the P1 peak showed the maximum MW to be slightly shifted toward lower MW for the benzene sample. This is also in agreement with the GC-MS analysis of the DCM-soluble fraction of the benzene sample demonstrating the greater abundance of three, four-ring PAH in respect to five- to seven-ring PAH.

The spectrum S2 of the 500 to 2000u fraction, for both benzene and ethylene samples, exhibits a broader shape in comparison to the S1 spectrum and presents the same optical band gap value (about 2), i.e. the same size of aromatic units, of the S1 spectrum measured for the 200-500u

species (P1 peak). It can be noticed that the maximum absorption of the S2 spectrum, placed at about 200nm, is largely shifted toward the UV in comparison to the maximum absorption (240-270nm) of S1 spectrum. These observations indicate that the same aromatic moieties present in the 200-500u species are clustered together in such way that the aromatic units do not electronically interact each other. Specifically, the shift of the UV band position toward the UV region of the S2 spectrum and the broad shape of the UV spectrum, typical of polymeric aromatic materials [Alfè et al., 2008], suggest that the 500-2000u species (P2 peak) are composed of small clusters/aggregates (dimers, trimers) of the 200-500u PAH units connected by sp^3 carbon bonding.

The spectra S3a exhibits a quite unstructured spectral shape typical of large (>10 rings) aromatic systems and consistent with the low optical band gap (around 1). Comparing S1 and S3a, the maximum absorption peak of larger size PAH should be shifted toward the visible at higher wavenumber in comparison with S1, whereas S3a maximum absorption appears to be located in the UV (about 200 nm). It can be concluded that the 1E5-1E6 u species are mainly in form of aromatic moieties clustered together by sp^3 carbon bonding that also allows the solubilization in DCM of such high MW species. In the benzene case the S2 and S3b UV peak position is located at higher values in comparison with ethylene.

The species up to 1000u (P1 and P2 peaks) are amenable for further analysis as fluorescence emission and mass spectrometry that have been used to give further information on the chemical nature of these products corroborating the attribution of specific chemical composition obtained by the above described spectral reconstruction procedure.

4.2.1.3 Fluorescence spectroscopy of MW-segregated fractions of DCM-solubles

Provided that the features of the fluorescence spectra of each MW-segregated fraction did not significantly change along the flame, the fluorescence spectra reported in the following are relative to the MW-segregated fractions of the LRT B-LT and E-HT samples.

Normalized fluorescence emission spectra at λexc= 350nm of the P1, P2 and P3a peaks, as separated by SEC, are reported in Fig.12.

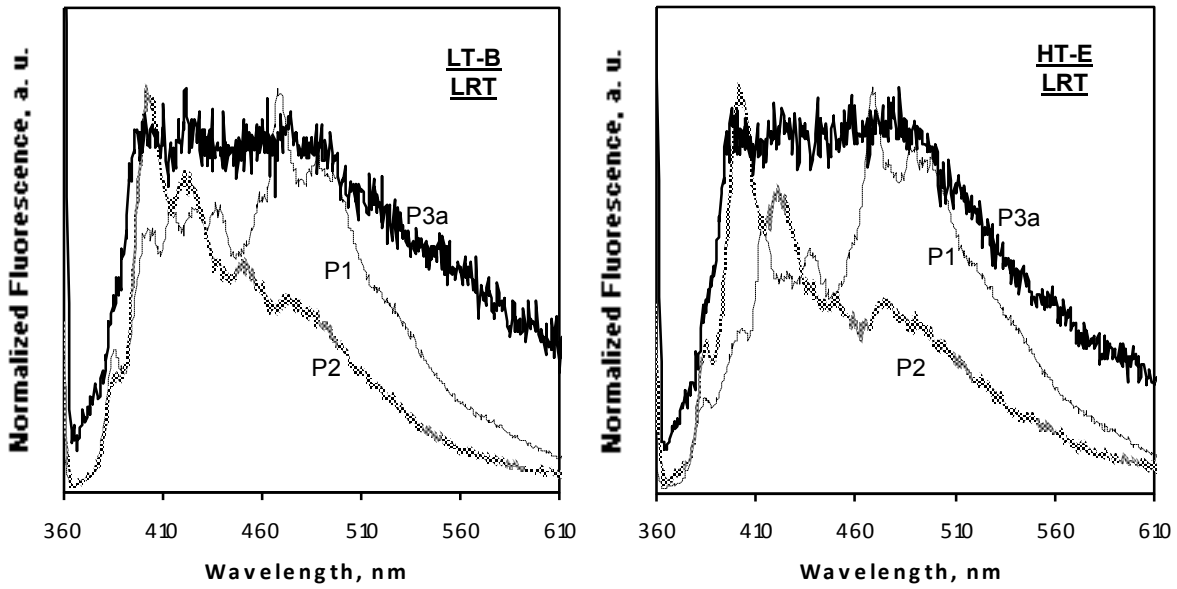

Fig. 12 Normalized fluorescence emission spectra at λexc = 350nm of the MW-segregated fractions (P1, P2 and P3a) at LRT in LT-B (left part) and HT-E (right part).

Generally, the fluorescence spectrum of PAH excited in the UV (up to 300nm) shows two main spectral regions: the first one from 300 to 350nm due to two- and three-ring PAH, and a second one between 350 and 500nm mainly due to larger PAH. [Berlman, 1971]. The emission spectra have been measured at 350nm that is the minimum excitation wavelength allowed to avoid the interference of NMP solvent fluorescence. But, the spectrum at λexc = 350nm relative to the P1 peak does not put well in evidence the greater presence of low-MW PAH in the benzene sample suggested by the spectral analysis.

Synchronous fluorescence simplifies the conventional emission spectrum of aromatic mixtures, because each peak roughly corresponds to single components or class of components, offering the possibility of a multicomponent analysis of complex PAH mixtures (Vo-Dinh, 1978).

The single peaks are directly correlated to specific aromatic ring systems and synchronous signals occur at higher wavelengths as the ring number increases. The synchronous fluorescence spectra, therefore, have a particular diagnostic value when used as a screening technique.

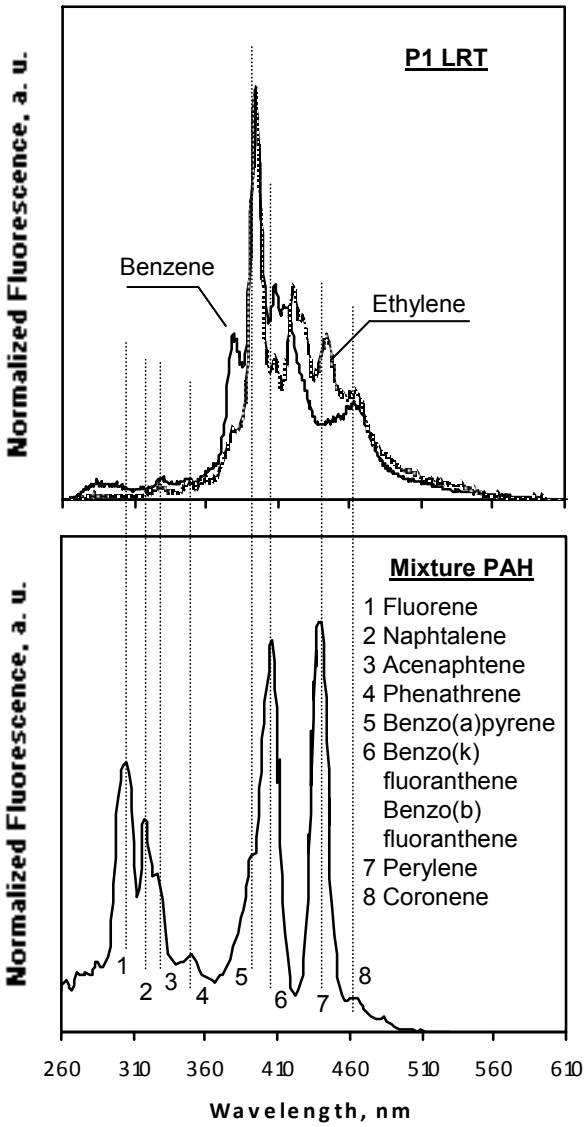

Fig.13. Normalized synchronous fluorescence at Δλ of 20 nm of benzene and ethylene LRT P1 fraction (upper part) and of a mixture of PAH (lower part)

In Fig.13, comparing the synchronous fluorescence of benzene and ethylene LRT P1 peaks with the synchronous analysis of a standard PAH mixture, the slight richness in five- up to eight- ring PAH in the ethylene sample is clearly shown, confirming the results obtained by the reconstruction procedure. Regarding the difference between P1 and P2 in the fluorescence emission spectra at λexc = 350nm (Fig.12), the possible effect of alkylic chains in dimers or trimers constituting the P2 peak could cause the shift of the P2 emission spectra in the UV region, in agreement with the UV-Visible spectroscopy (Fig. 11). Another possible explanation regards to the fact that light PAH, abundantly formed in flame, escape to the deposition on the quartz plate. The GC-MS analysis of the DCM-soluble fraction recovered from the deposited sample, showing the very low abundance of two-, three-ring PAH and the richness in four- to seven-ring PAH. Interestingly enough, the flame-

formed PAH, as measured by isokinetic probe-sampling and GC-MS analysis, have shown to be mainly constituted of light two-three-ring PAH (Apicella et al., 2002). Two-, three- ring PAH, linked to form heavier compounds, can not escape anymore, and could cause a blue shift in the emission spectra.
The broadness and the extension toward longer wavelengths of the emission spectra of the P3a peak (Fig. 12) is consistent with the high and wide MW of these species.

4.2.1.4 AP–LDI mass spectrometry of low-MW-segregated fractions of DCM-solubles

The AP-LDI mass spectra of P1 peak were found to be focused in the m/z 200-500 range with the maximum at about m/z 300. They consist of a sequence of major ions with a spacing of 24–26 u superimposed on a sequence of minor ions that present the same spacing of 24–26 u; the sequence of minor peaks is displaced at 12 u relatively to the sequence of the major ions. The sequence with both 12 and 24 u mass increments is typical of PAH molecules and has been previously observed by MS analysis of DCM-soluble fraction of particulate sampled of premixed flames of ethylene (Apicella et al., 2007). The AP–LDI mass spectrum of P2 peak shows a continuous sequence of masses also in the m/z 300–2000 range typical of polymeric structures (Rodgers et al., 2004). The shape of the mass spectra is thus consistent with the chemical attribution to polymeric structures done by UV-Visible spectroscopy, whereas the MW range detected by MS is much lower and not consistent with the MW attributed by SEC. The discrepancy is due to the high tendency to fragmentation of polymeric materials in the desorption and ionization phases of the mass spectrometric analysis. (Hortal et al., 2008). However, the mass spectrum of fragments is in any case informative of the original polymer.
The results of the AP–LDI–MS analysis in terms of weighted averages of the mass measured for the P1 and P2 peaks at LRT and HRT are reported in Tab.4.
The ranges selected to calculate the mean values were the ranges assigned to P1 and P2 peak by SEC fractionation.
The mean mass values for P1 peaks show a slight richness in heavier PAH in the ethylene flame, on the opposite the P2 peak clearly shows the presence of heavier masses in the benzene samples. This is in agreement with the spectral trends obtained by reconstruction procedure.

Flame	Weighted Average MW			
	Peak P1 (200-500 u)		Peak P2 (500-2000 u)	
	LRT	HRT	LRT	HRT
LT-B	350	350	915	905
HT-E	355	370	780	850

Tab.4 Weighted averages MW as measured by AP–LDI–MS for the P1 and P2 peaks at LRT and HRT in the LT-B and HT-E flames.

4.2.2 MW-segregated fractions of soot

SEC analysis of the dry soot, recovered from the quartz by NMP treatment after DCM washing, has been performed obtaining the MW distribution, reported in Fig.14.

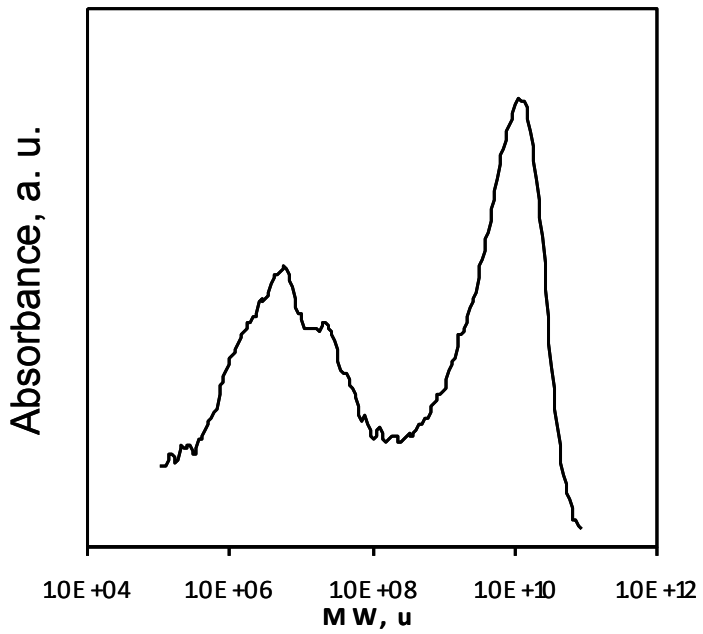

Fig. 14 MW distribution obtained by SEC for HT-E LRT soot

The MW distribution of dry soot fraction extended over the high-MW range (1E5-1E11u) with a broad peak occurring in MW region, 1E5-1E8u, partially coincident with the peak P3a and, for analogy named P3b. The predominance of a large MW peak (named P4) ranging from 1E9 to 1E11u and having the MW maximum located at about 1E10u was noticeable.

4.2.2.1 Optical Band Gap Analysis of MW-segregated fractions of soot

On the apex of these peaks, the UV-Visible spectra, named S3b and S4, are measured by UV-Visible diode array system from 290 to 600 nm. In spite of their broad and structured shape, the on-line spectra measured in different points of each peak did not show significant differences both in terms of spectral features and optical band gap.

RT, ms	Δ t from soot inception, ms		Dry soot	
			S3b [10E5-10E8u]	S4 [10E9-10E11u]
LT-B LRT				
42	17	Eg, eV	1.0	0.29
HT-E LRT				
32	17	Eg, eV	1.1	0.31
LT-B HRT				
74	49	Eg, eV	0.9	0.2
HT-E HRT				
60	45	Eg, eV	1.0	0.25

Tab. 5 Band gap of the soot MW-segregated fractions in the LT-B and HT-E flame at LRT and HRT.

Information on structural variations in terms of dimension of aromatic size system can be obtained from the analysis of the optical band gaps at different residence time reported in tab. 5. The optical band gap values of peak P3b are quite constant along both flames, even if lower values have been evaluated in the benzene flames. On the other hand, the optical band gap of the highest MW species (1E10u), belonging to the dry soot (peak P4), clearly decreases at higher flame heights, reaching also in this case a lower value for the benzene flame. From the analysis of the band gap profile along the flame axis it can be concluded that only the large particles from 1E8 to 1E11, undergo dehydrogenation/condensation reactions, modifying their internal structure during the particle formation process.

4.2.2.2 UV-Visible maximum absorption position of MW-segregated fractions of soot

As mentioned before more information on the arrangement of the aromatic islands can be obtained through the analysis of the UV-visible maximum position of each MW segregated fractions of soot. Soot spectra are directly measured on the quartz plate after DCM treatment of the total carbonaceous species deposited

The spectra were reconstructed using the procedure described in details in 4.2.1.2.

Briefly, soot spectrum has been reconstructed in the range 290-600 nm by the linear combination of the spectra measured on the P3b and P4 peaks, then in the range 190-290nm Gaussian functions have been used.

The typical output of the reconstruction procedure, used for getting the spectra in the whole UV-Visible range (downward to 190nm), is given in Fig. 15, reporting the UV-Visible spectra of soot sample at low residence times in the benzene and ethylene flame in comparison with the reconstructed spectrum and the spectra of the relative MW-segregated fractions.

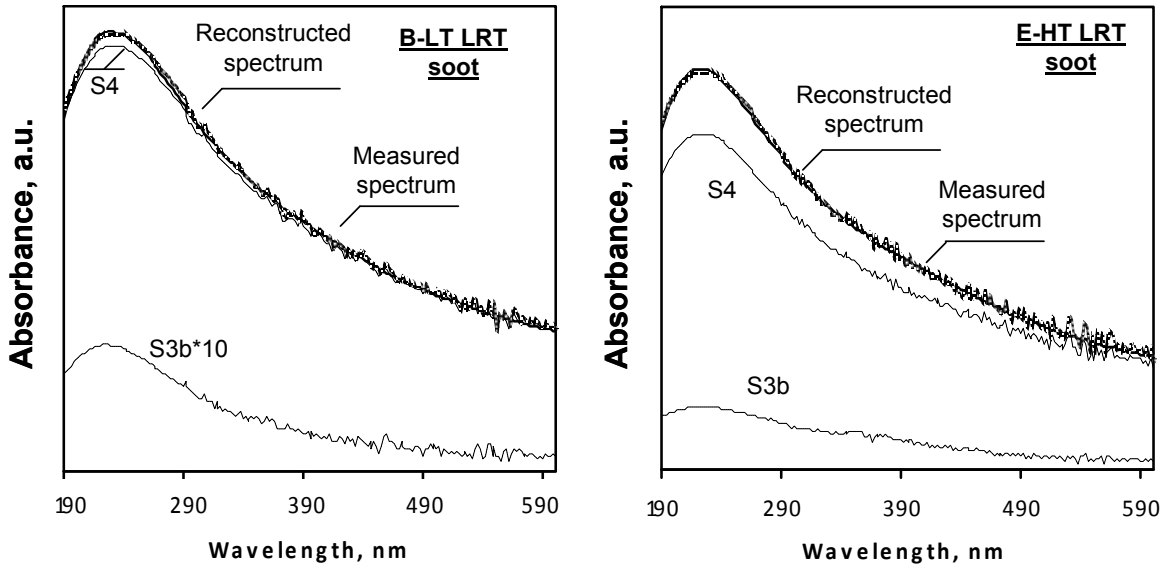

Fig. 15 UV-Visible spectra of the soot sampled at LRT in LT-B (left part) and HT-E (right part), in comparison with the output reconstruction procedure.

The maximum absorption positions of the MW-segregated fractions spectra as evaluated from the reconstruction procedure are reported in tab. 6 for soot sampled at low (LRT) and high (HRT) residence times in the benzene and ethylene flames.

The spectra S3b, relative to species in the wide 1E5 to 1E8u MW range, exhibit a quite unstructured spectral shape typical of large (>10 rings) aromatic systems and consistent with the low optical band gap (around 1). For both ethylene and benzene samples, the maximum absorption position of the 1E5-1E6u (see 4.2.1.2) is shifted toward the UV (maximum at about 200 nm) in respect to the maximum absorption position of the peak P3b (maximum at 225 nm) indicating the larger sp^3 character of the 1E5-1E6u species of the peak P3a. Reminding that the P3a peak belongs to the DCM-soluble fraction whereas the P3b belongs to the insoluble soot fraction, just the larger sp^3 (aliphatic) character of the 1E5-1E6u in respect to the peak P3b, justifies the solubility of these high MW species in DCM.

RT, ms	*Δt from soot inception, ms*		**Dry soot**	
			S3b [10E5-10E8u]	*S4 [10E9-10E11u]*
LT-B LRT				
42	*17*	*λ(Amax), nm*	*226*	*230*
HT-E LRT				
32	*17*	*λ(Amax), nm*	*223*	*223*
LT-B HRT				
74	*49*	*λ(Amax), nm*	*226*	*244*
HT-E HRT				
60	*45*	*λ(Amax), nm*	*223*	*235*

Tab. 6 UV peak position of soot MW-segregated fractions in the LT-B and HT-E flame at LRT and HRT.

Moreover, all the spectral features, regarding the DCM-soluble MW segregated fraction (see 4.2.1.2) and P3b, do not exhibit any variation for effect of the residence time increase. This testifies that the species up to 1E8 u do not undergo internal structure transformations during the soot formation process.

On the opposite both the maximum absorption position and the optical ban gap of the 1E8-1E11u drastically change along the flame. Indeed, the UV maximum position of S4 spectra of the 1E8-1E11u clearly moves toward the visible (up to about 240nm) along the flame whereas the optical band gap value decreases. Both these trends demonstrate the occurrence of graphitization processes pertaining to these large MW species/particles.

Comparing these features for benzene and ethylene samples, the lower final values of band gap and the highest UV maximum position of the spectrum S4 observed for benzene in comparison to ethylene can be also noted. This suggests the larger aromatic character of benzene soot in respect to ethylene soot especially at higher residence times.

4.2.3 Contribution of MW segregated fractions to the spectral absorption of carbon particulate

Each MW-segregated fraction, contribute to the absorption spectra of the total particulate, measured directly on the quartz plate before DCM treatment. Table 7 reports the contribution of each MW-segregated fraction to the absorbance measured at 350nm of the total deposited carbonaceous species.

RT, ms	Δ t from soot inception, ms		DCM soluble fraction			Dry soot	
			S1 [200-500u]	S2 [500-2000u]	S3a [10E5-10E6u]	S3b [10E5-10E8u]	S4 [10E9-10E11u]
LT-B LRT							
42	17	Abs%@350nm	2.6	3.9	3.5	1.6	88.4
HT-E LRT							
32	17	Abs%@350nm	19.2	7.7	9.7	9.8	53.5
LT-B HRT							
74	49	Abs%@350nm	3.2	2.6	3.2	0.1	90.9
HT-E HRT							
60	45	Abs%@350nm	4.4	2.2	5.1	3.1	85.24

Table 7 Percentage contribution of the MW-segregated fractions at 350nm evaluated for the DCM-soluble and dry soot fractions of the carbonaceous species deposited in the LT-B and HT-E flame at LRT and HRT.

For the LRT and HRT benzene samples the peak P4 almost completely takes into account for the absorption at 350nm of the total deposited carbonaceous species, whereas in the ethylene flame only at HRT the contribution of P4 species to the absorption at 350nm is quite predominant, confirming the rapid almost undetectable passage to well-formed soot particles in benzene flames.

4.3 Soot characterization

4.3.1 Microscopic analysis

TEM images of methane soot show not-perfectly spherical particles imbedded in an amorphous coalesced material, as shown in Fig. 16.

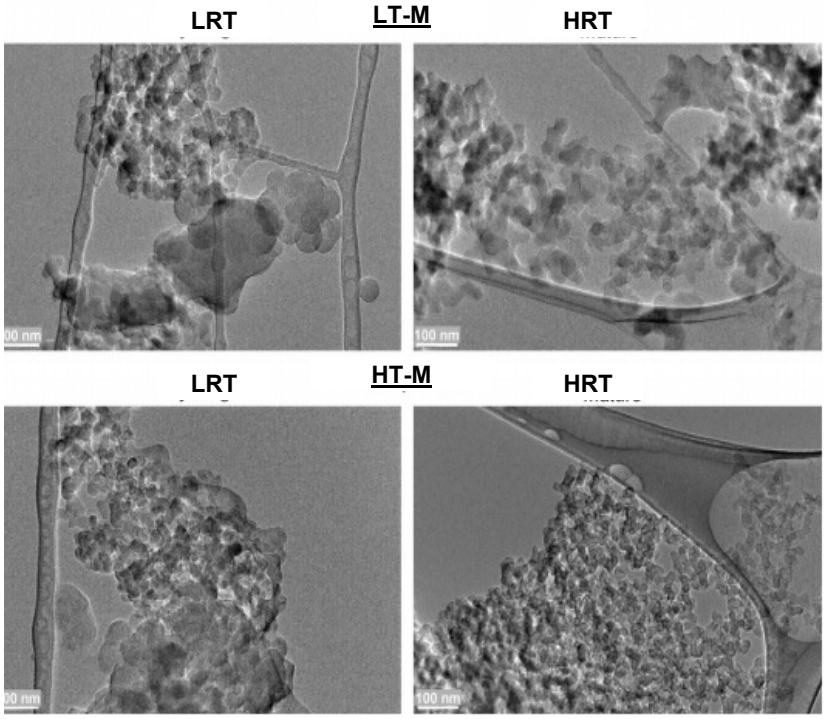

Fig.16 TEM images of LRT and HRT soot formed in LT-M (upper part) and HT-M (lower part) flames. Adapted from Alfè et al., 2010

The reduction of amorphous material and small differences in the soot nanostructure can be observed in both temperature conditions (LT-M and HT-M) except for a development of some well structured onion-like structures observed in the higher temperature conditions (HT-M) [Alfè et al., 2010]. As previously found [Alfè et al., 2009], also the primary particles from ethylene flames studied in this work are found to be not perfectly spherical and imbedded in amorphous coalesced material; however, a progressive structural order development, in terms of the increase of a concentric organization of the stacked graphitic layers around an amorphous core, is observed.
In contrast, benzene soot, reported in Fig.17, even at LRT exhibits well-rounded particles.

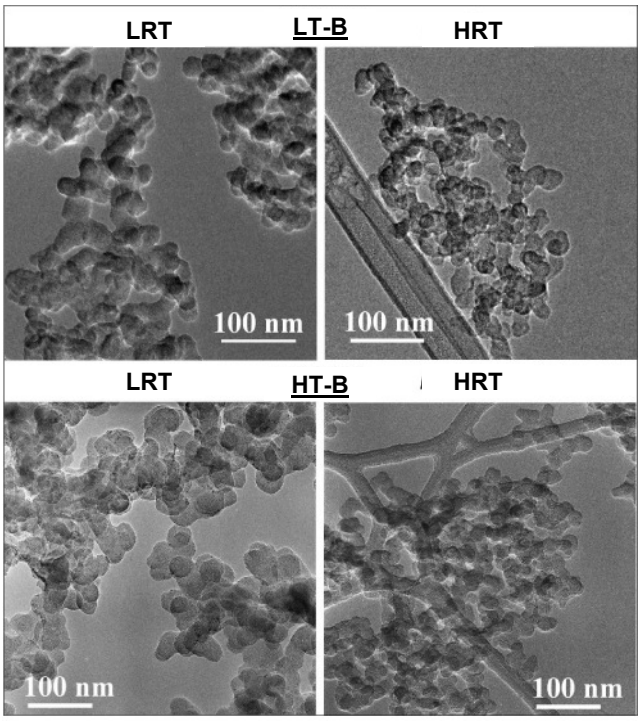

Fig.17 TEM images of LRT and HRT soot formed in LT-B (upper part) and HT-B (lower part) flames.

In benzene soot a definite development of onion-like structures as soot ages can be noted in agreement with previous work [Alfè et al., 2009]. In the high-temperature benzene flame (HT-B) this effect is more noticeable, moreover concentric shell nanostructures result to be particularly evident in HRT soot.

Table 8 reports the main structural parameters measured by lattice fringe analysis on all soot samples collected just after the inception and at the end of soot formation region.

In agreement with previously published work on various carbon materials [Oberlin, 1990; Santamaria et al., 2010; Alfè et al., 2009; Vander Wal et al., 2003; Palotas et al., 1996] it can be generally observed that the BSU are constituted of about 2-3 stacked layers having a layer length much below 1 nm. The spacing of the layers is quite constant (0.38 nm) and larger than the graphitic spacing of 0.335 nm, due to the turbostratic character of flame-formed soot [Alfè et al., 2009; Alfè et al., 2010].

Flame label	rt (ms)	L (nm)[a]	L (nm)[b]	La (nm)	d (nm)	Lc (nm)	N	% nsl
LT-M	18	0.45	0.70	0.28	0.39	0.49	2.30	66.8
	50	0.50	0.74	0.34	0.38	0.62	2.60	51.1
HT-M	17	0.46	0.72	0.30	0.40	0.54	2.40	59.6
	41	0.57	0.82	0.39	0.39	0.69	2.80	38.2
LT-E	48	0.49	0.74	0.32	0.38	0.55	2.50	60.9
	75	0.57	0.81	0.38	0.38	0.73	2.90	38.8
HT-E	22	0.49	0.74	0.31	0.39	0.58	2.50	54.4
	60	0.52	0.94	0.35	0.38	0.63	2.70	44.2
LT-B	29	0.52	0.77	0.36	0.38	0.65	2.70	46.9
	74	0.60	0.86	0.45	0.38	0.70	2.90	37.8
HT-B	18	0.55	0.80	0.36	0.38	0.59	2.60	55.4
	55	0.59	0.87	0.47	0.38	0.70	2.90	41.2

Tab. 8 Structural parameters of soot by HR-TEM analysis. L^a has been evaluated for fringes >0.246nm and a distortion ratio Θ = 15%. L^b has been evaluated for fringes >0.49 and a Θ = 40%. La, d, Lc, N and %nsl have been evaluated for fringes>0.246nm and Θ = 15%

A slight increase of the layer length can be noted for effect of the temperature field and aging, whereas a more sensitive parameter appears to be the percentage of non-stacked layers (nsl) in respect to the total number of layers. Overall, the high percentage of non-stacked layers testifies the large disorder degree of soot particles. The nsl percentage is higher (50-60%) for the young soot at low temperature and lower (30-40%) for the mature soot at high flame temperature. Regarding the fuel effect, it can be assessed that the higher order extent, in terms of layer size and nsl percentage, is exhibited by benzene soot in comparison to methane soot exhibiting the larger disorder degree. Among these fuels, ethylene soot presents an intermediate order degree.

4.3.2 Elemental and thermogravimetric analysis

The H/C atomic ratio of soot, reported in Fig. 18, is a very good signature of the soot dehydrogenation process.

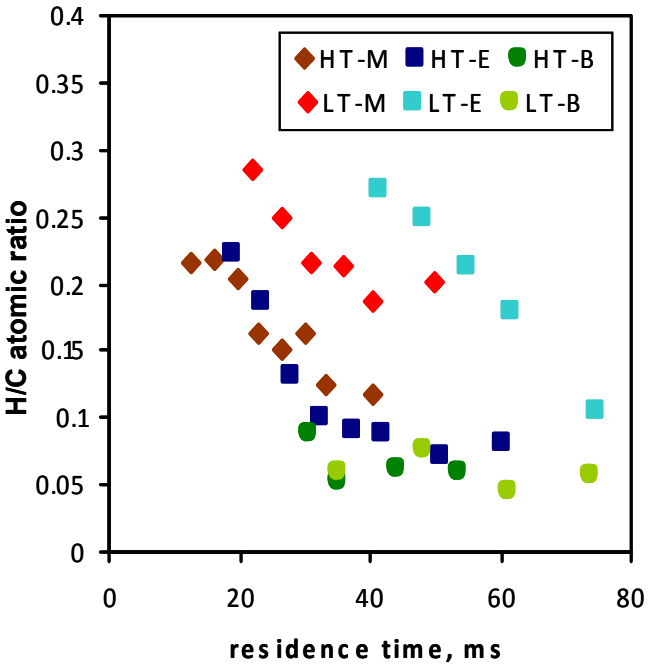

Fig. 18. H/C atomic ratio of soot for methane, ethylene and benzene flames as a function of the residence time.

For the methane and ethylene flames the H/C shows the usual trend steeply decreasing as a function of the residence time. As also expected, lower H/C ratios can be observed in the higher temperature conditions (HT-E and HT-M), nevertheless it is noticeable that methane soot keeps on high amounts of hydrogen at longer residence times whichever the temperature (LT-M and HT-M). On the opposite, the H/C ratio of benzene soot in both temperature conditions (LT-B and HT-B) is very low and quite constant along the flames. Only ethylene soot reaches such low H/C values, undergoing a more fully dehydrogenation process in high temperature conditions (HT-E).

It will be shown in the following that the high content of hydrogen of methane soot, from the beginning to the end of the flame, is mainly due to aliphatic hydrogen, mainly in form of methylene CH_2 groups, as measured by FT-IR spectroscopy. This can be attributed to the chemical environment, rich of unburned methane fuel, hydrogen and light aliphatic hydrocarbon products, in which soot inception occurs. By consequence, in the first nuclei of methane soot the intervention of aliphatic groups is massive and causes the high disordered structure. The significant persistence of methylene groups, even for higher temperature conditions, suggests that methylene groups act as cross-linkers cementing the aromatic layers and limiting the occurrence of further dehydrogenation/graphitization process in the investigated residence time range. It can be suggested that methane soot behaves as the so-called non-graphitizing carbon for which the graphitization process, in turn resulting in the absorption coefficient increase, occurs to a lower extent [Franklin, 1951]. However, it cannot be excluded that the lower dehydrogenation of methane soot is due to the

chemical and thermal environment in which methane soot is formed and transformed. In any case, just the methylene groups and the higher microporosity of methane soot causes it to be more susceptive to oxidation as confirmed by the lower combustion temperature of methane soot measured by oxidative thermogravimetry, in comparison to benzene and ethylene soot [Alfè et al. 2009; Alfè et al. 2010].

Benzene soot is more aromatic from the beginning presenting a negligible content of hydrogen, mainly aromatic hydrogen, since it nucleates before the complete depletion of benzene fuel and oxygen, in a very reactive chemical environment rich of aromatic radicals and species, and poor of hydrogen and light aliphatic hydrocarbons. It incorporates low amount of hydrogen and aliphatic species and is also less liable to oxidation [Alfè et al. 2009; Alfè et al. 2010]. Ethylene soot presents an intermediate behavior since it is formed in an environment rich of both light aliphatic and aromatic (benzene) hydrocarbons. Thus, soot presents from the beginning a structure with an order intermediate between methane and benzene soot, the presence of both aliphatic and aromatic hydrogen and it is prone to undergo an almost fully dehydrogenation and graphitization process.

4.3.3 Raman spectroscopy

Raman spectroscopy is a suitable technique to differentiate sp^2 carbon structures and for probing disorder in carbon materials (Ferrari et al., 2000).

Generally, the visible Raman spectra of amorphous/disordered carbons show two prominent features: the so-called G or graphite peak, around 1600 cm^{-1}, and the D or defect peak, around 1350 cm^{-1}, and some minor modulations usually around 1100–1200 cm^{-1} and 1400–1500 cm^{-1}.

In this thesis, Raman spectroscopy has been applied to the carbon particulate deposited on a quartz plate at high and low residence times in selected flames of methane (HT-M), ethylene (HT-E) and benzene (LT-B) having similar flame temperatures. Raman spectra have been measured on the particulate, stripped of adsorbed hydrocarbons by DCM extraction, to avoid their interference on the spectral features related to solid carbon structures. Typical Raman spectra measured with 514 nm excitation wavelength are shown in Fig. 19. In the same figure the Raman spectrum of the quartz plate is also reported to ascribe to the substrate some spikes and peaks present in the sample spectra. The spectra exhibit two broad and strongly overlapping bands peaking at ~ 1350 cm^{-1} (D peak) and ~ 1600 cm^{-1} (G peak) typical of carbon materials (see 2.1.2). Spectral parameters significant of soot nanostructure, as the position of D and G bands, their full widths at half maximum (FWHM) and the ratio of their intensity (I(D)/I(G)) vary in dependence of the different carbon arrangements and offer the possibility to derive structural information.

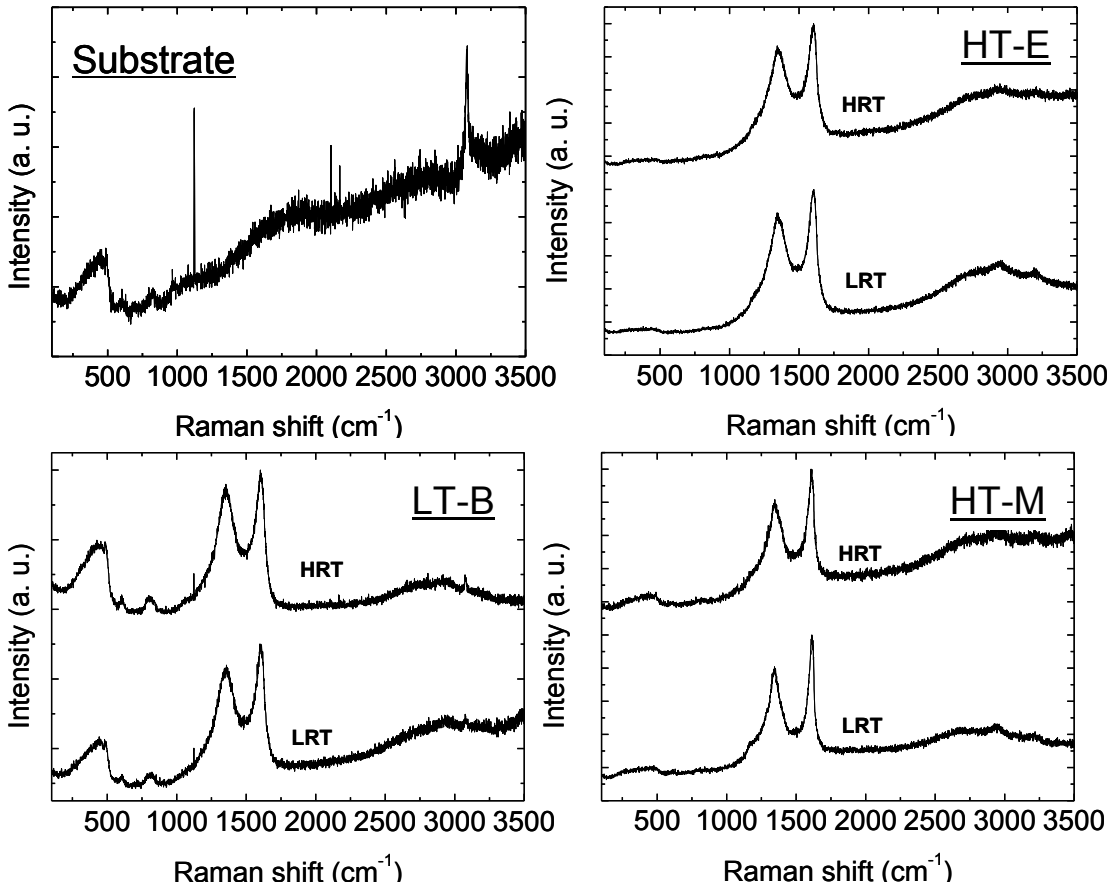

Fig. 19 Raman spectra of substrate (quartz plate) and soot sampled in LT-B, HT-E and HT-M at LRT and HRT and measured with 514 nm excitation line.

The I(D)/I(G) ratio is the main feature that is generally taken into consideration when studying disorder by means of Raman spectroscopy. However, disorder also causes the position shift and the broadening of the Raman peaks. By consequence, the evolution of the Raman peak width and frequency shifts are additional signatures of disorder degree in carbon structures. These spectral parameters exhibit also a significant dependence on the excitation wavelength. Indeed, multi-wavelength Raman spectra have shown to be useful to distinguish the different types of amorphous carbons and to derive their structural and mechanical properties (Ferrari et al., 2001; Casiraghi et al., 2005). Thus, Raman spectra of soot samples have been measured at different excitation wavelengths, namely at 457 nm, 514 nm and 633 nm.

The spectral parameters are usually obtained by deconvolution (curve-fitting) procedures. The simplest fit consists of two Lorentzians or two Gaussians for the two prominent Raman features, D and G peaks. A simple two symmetric-line fit is not always suitable, since in particular conditions the minor contributions at around 1100–1200 cm^{-1} and 1400–1500 cm^{-1} can rise and a multi-peak fit

is necessary. The five-band fitting of all first-order Raman bands (G, D1, D2, D3, and D4 at about 1580, 1350, 1500, 1620, and 1200 cm^{-1}) has been also applied by Sadesky for soot and related carbonaceous materials (Sadezky et al., 2005). However, the difficulty in separating the overlapping G, D2, and D3 bands as well as in discriminating the weak D4 band is the major source of uncertainties in the peak fitting. To reduce the uncertainties in the peak fitting, the location of each band should be, thus, constrained (Soewono et al., 2011).

In this thesis a two-band fitting method has been applied based on a Breit-Wigner-Fano (BWF) function for the G peak and a Lorentzian function for the D peak for the Raman spectra obtained with 457nm and 514nm exciting lines. An additional Lorentzian function has been used to fit a clear peak at around 1200cm-1 observed in the Raman spectra with exciting line of 633 nm. In Fig. 20 the good fitting of Raman spectra of soot measured with 457 nm, 514 nm and 633 nm exciting lines is shown.

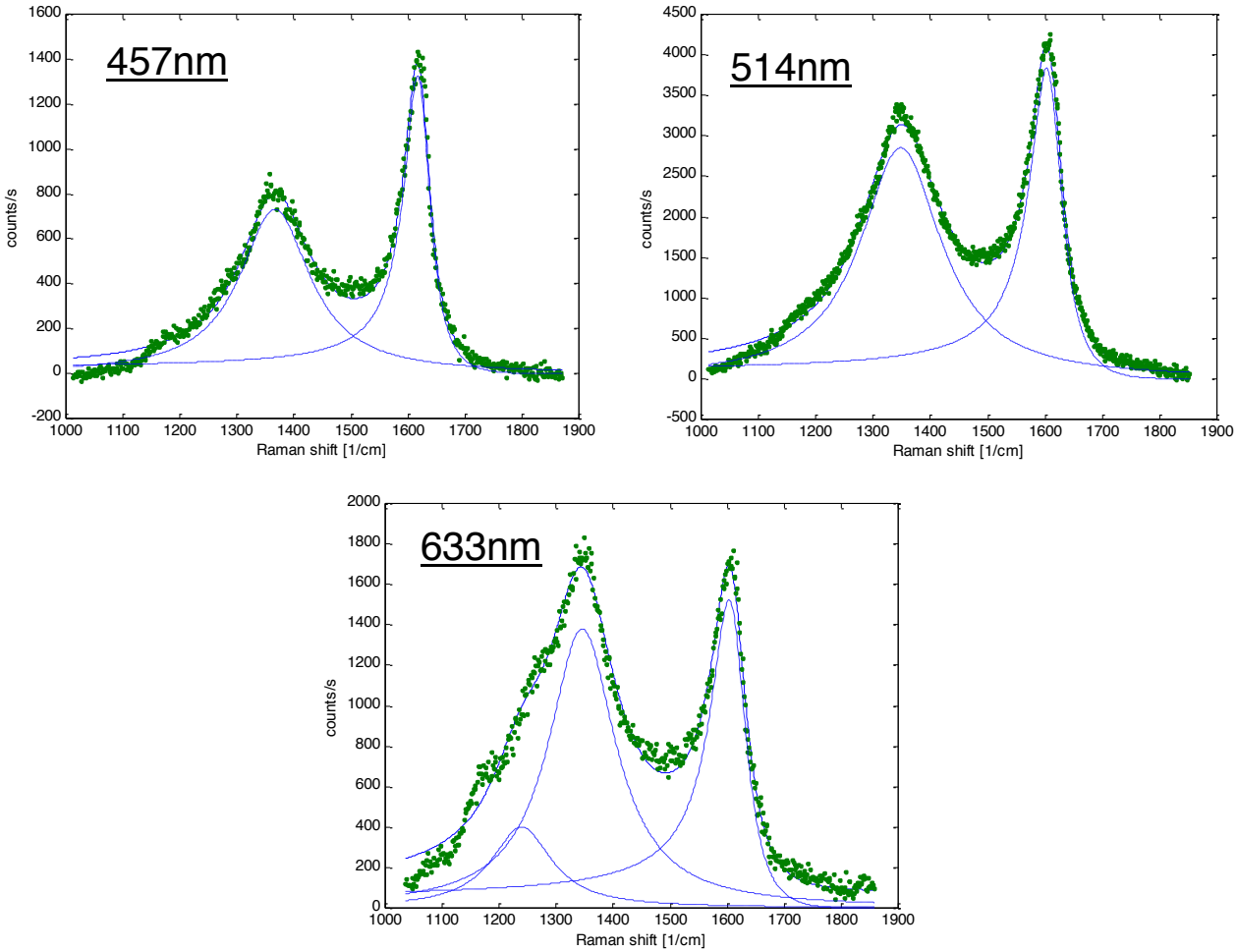

Fig. 20 Typical curve fit of soot Raman spectra at 457 nm, 514 nm and 633 nm exciting lines.

To follow soot transformation involving changes of the structural carbon order, the position of D and G peaks of visible Raman spectra measured at 457 nm, 514 nm and 633 nm excitation

wavelength are summarized in Figs. 21-22 as a function of the residence time of methane, ethylene and benzene flames.

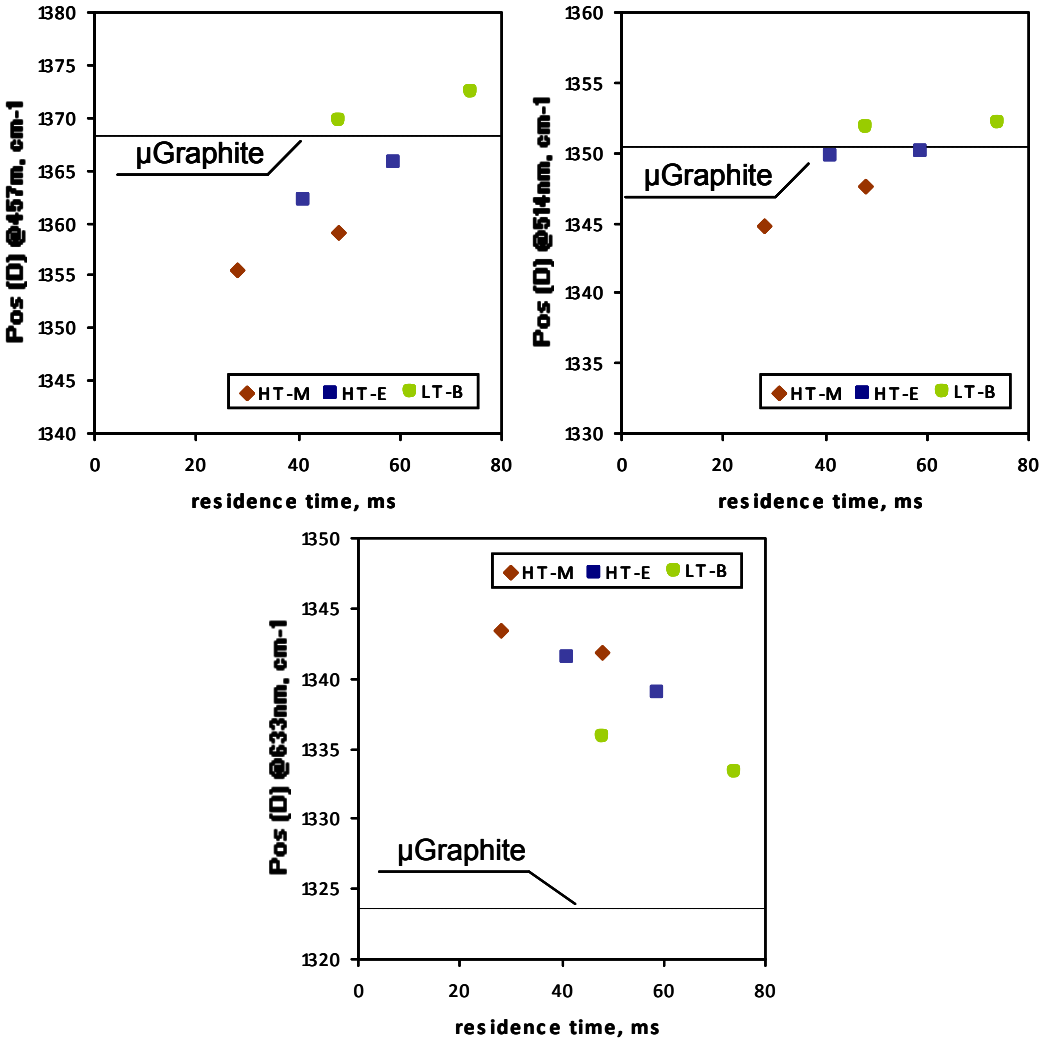

Fig. 21 Position of D peak in Raman spectra, measured with an excitation wavelength of 457nm, 514 nm and 633 nm, of µgraphite (Reich et al., 2004) and of soot sampled in LT-B, HT-E and HT-M as a function of the residence time.

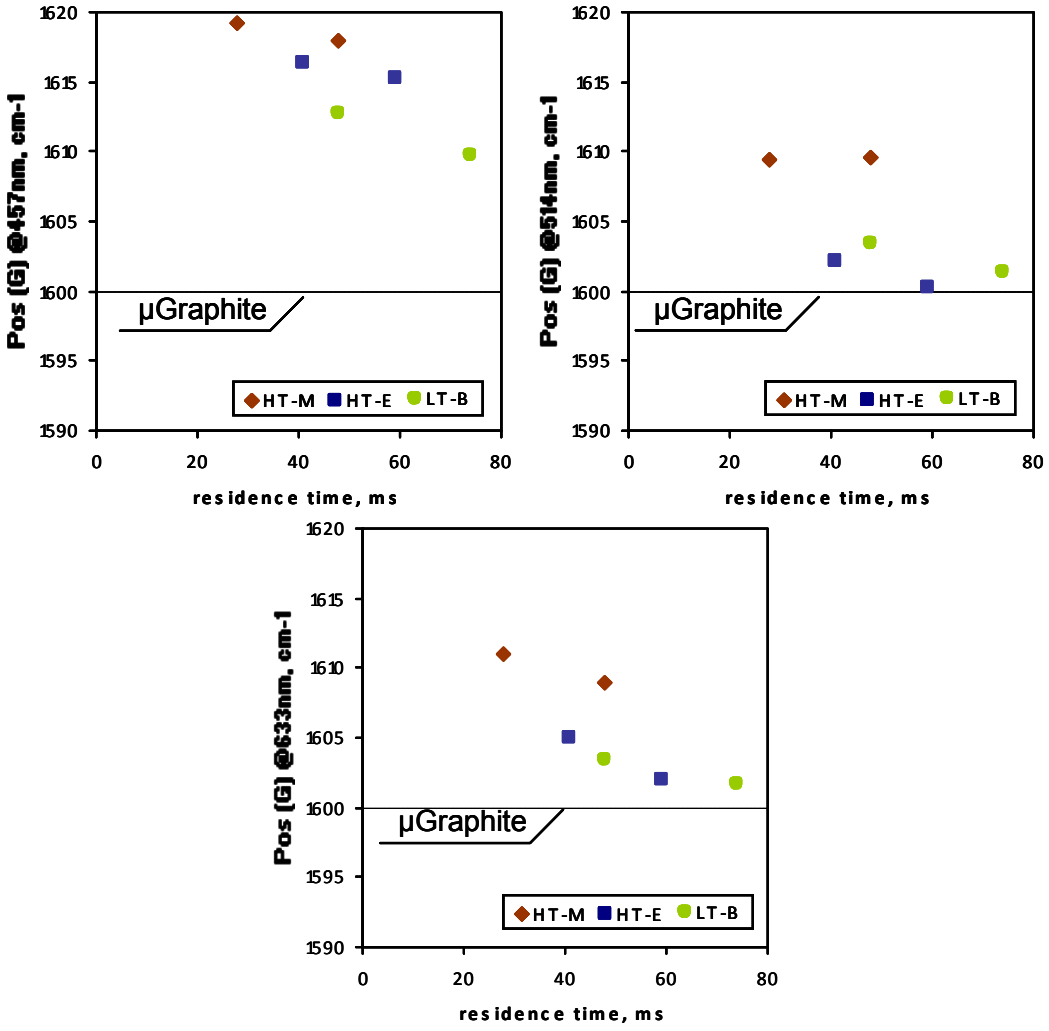

Fig. 22 Position G peak in Raman spectra, measured with an excitation wavelength of 457 nm, 514 nm and 633 nm, of µgraphite (Reich et al., 2004) and of soot sampled in LT-B, ,HT-E and HT-M as a function of the residence time.

Raman spectra have been also measured down in the UV using an excitation wavelength of 244 nm. However, the UV Raman presented some problems mainly due to the high background at this wavelength. In order to get a significant signal, a very high acquisition time (120 s) was necessary. Furthermore, the power on the sample was kept well below 1 mW and the samples were placed on a spinner rotating at high speed (>3000 rpm) in order to avoid damage to the sample for effect of the UV light. As shown in Fig. 23 the quartz plate has a strong signal and all the UV Raman spectra have been corrected for this contribution and for signal due to the instrumental optics. Only a clear G peak can be noticed in the lower part of Fig. 23 where a typical UV Raman spectrum is reported.

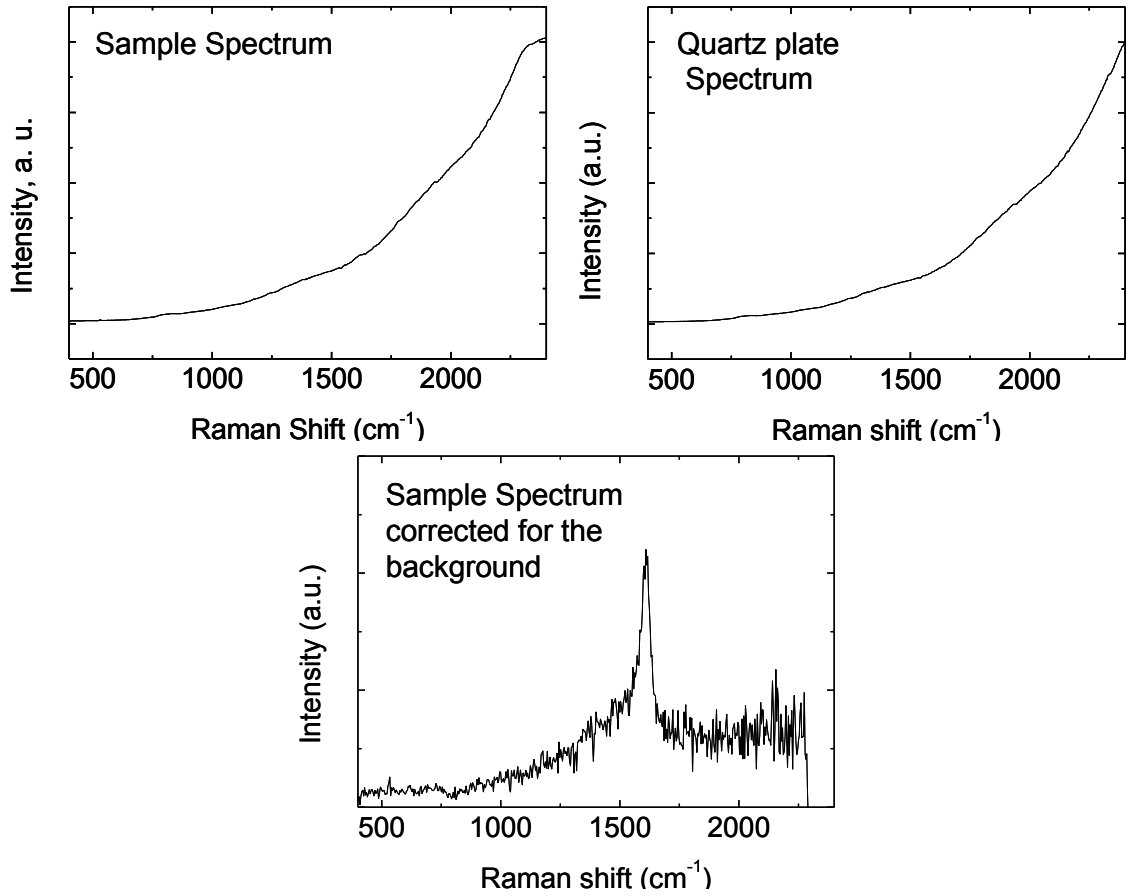

Fig. 23 Typical soot Raman spectrum (top left part) compared with quartz plate Raman spectrum (Top right part) measured with an excitation wavelength of 244 nm. In the low part is reported the UV Raman spectrum of soot corrected for background signal.

Actually, UV Raman measurements appear to be unable to give complete information on the disorder in respect to the visible Raman and only the G peak position measured in the UV could be derived and taken in consideration.

Overall, the variation of the position of D and G peaks of Raman spectra of soot at different residence times and for whichever excitation wavelengths (Figs. 21-22), indicates the occurrence of structural transformation of soot during its formation/growth as the residence time increases.

The different values and trends of the peak position as a function of the excitation wavelength have been interpreted referring to the micrographite (μGraphite) Raman parameters (Reich et al., 2004) since μgraphite is a graphitic carbon having a relatively high level of order, but still presenting the D peak.

Overall, it can be noted that the position of D peak increases or decreases with the residence time in dependence of the excitation wavelength. The increase or decrease appears to be related to the general tendency of the D peak to move toward the μGraphite D peak position which is itself

variable as a function of the excitation wavelength (Fig. 21). It can be also noticed that benzene and methane soot exhibit, respectively, the nearest and farthest D peak position value in comparison to the μGraphite D peak position. These findings indicate the progress of soot graphitization as residence time increases, and the higher and lower order degree of benzene and methane soot, respectively.

In comparison to the D peak position, more regular trends can be observed for the G peak position (Fig. 22) that appears to decrease with residence time, whichever is the excitation wavelength.

In graphitic carbon structures as graphite and μgraphite, the G peak position is placed at 1580 cm^{-1} and 1600 cm^{-1} , respectively, whereas the G peak is located well beyond 1600 cm^{-1} in disordered carbon materials also containing sp^2 chains (Ferrari et al., 2001). Thus the observed G peak location above 1600 cm^{-1} (Fig. 22) indicates that, beside to sp^2 phases in forms of rings, there is a significant contribution of sp^2 segments not organized in aromatic rings. It is also observed that, whichever the excitation wavelength, the G peak position of soot downshifts as the residence time increases, approaching to the values of μgraphite. This testifies the graphitization process occurrence in agreement with the trend of the D peak position before described. Regarding the fuel effect, only the higher disorder of methane soot can be observed given its higher G peak position in respect to ethylene and benzene soot having similar and lower values of G peak position.

By reporting the position of G and D peaks as a function of the excitation wavelength (Figs. 24-25) the rate of change of the peak position with the excitation wavelength, named dispersion (Casiraghi et al., 2005), can be followed giving an overall view of the structural information on soot samples grouped together. It is worth to remark that the G peak position for ordered materials, as graphite and μgraphite, does not show any dispersion, being constant the position of G, whichever the excitation wavelength.

Using this parametric representation, the dispersion of the G peak position for all soot samples in respect to the constant value of μgraphite, also reported in Fig.24, can be followed. It appears more clearly that the G peak position is higher than 1600 cm^{-1} and increases as wavelength decreases from 633 nm down to 457 nm.

Indeed, the G peak dispersion of soot samples has to arise from the resonant selection of sp^2 clusters of different sizes at different excitation energies (Casiraghi, 2005). Thus, the G peak dispersion of soot in the 633-457 nm range demonstrates that soot is a highly disordered carbon with a wide range of aromatic and not aromatic sp^2 configurations with different local band gaps (Casiraghi, 2005).

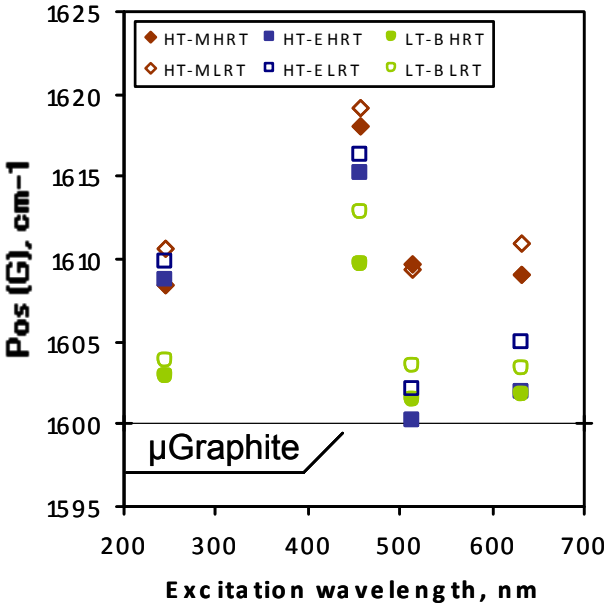

Fig. 24 The position of G peak in function of the excitation wavelength of μgraphite (Reich et al., 2004) and soot sampled in LT-B, HT-E and HT-M flames.

This result is confirmed by the appearance of a peak at around 1200 cm^{-1} assigned to trans-polyacetylene segments lying in grain boundaries (Ferrari et al., 2001b), proving the presence of sp^2 bonds not in form of aromatic rings. The intensity of this peak is enhanced at higher excitation wavelengths in the visible region, thus it can be clearly detected only at 633nm (Fig. 20).

In contrast with the increase of G peak position from 633 to 457 nm, it is worth to note that the position of G decreases going toward 244 nm, probably because of spectra manipulation with multiple subtracting of backgrounds or due to not visible damages to the sample occurring during UV Raman measurements. More careful measurements will be necessary to extend the study of the Raman spectral features wavelength dependence to the UV range.

Unlike the G peak dispersion of ordered carbon materials, in previous work it has been found that the D peak exhibits the maximum dispersion for microcrystalline and nanocrystalline graphite, and the dispersion of disordered carbon materials decreases for increasing disorder, i.e. the dispersion of D is proportional to order (Ferrari et al, 2001).

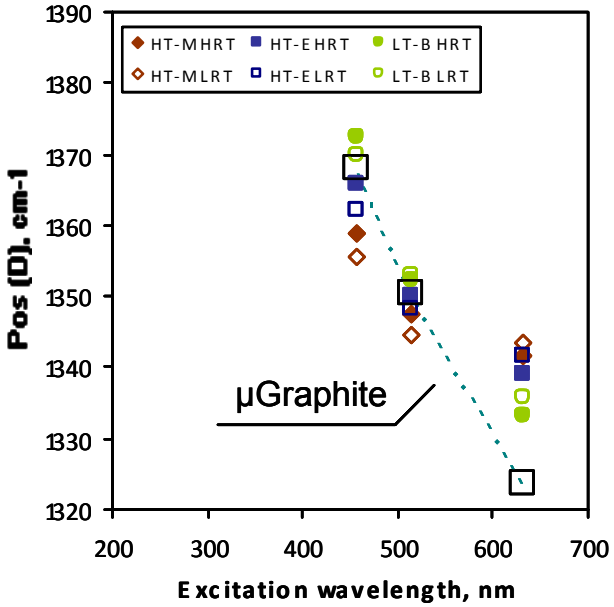

Fig. 25 The position of D peak in function of the excitation wavelength of µgraphite (Reich et al., 2004) and soot sampled in LT-B, HT-E and HT-M flames.

The increase of D peak position of soot, reported as a function of the excitation wavelength in Figure 25, follows the increase of µgraphite from 633 to 457 nm, but with a different dispersion. Moreover, the higher and the lower dispersion of D position can be observed in benzene and in methane soot, respectively. This indicates that the dispersion of D peak position appears to be more sensitive to the structural order in soot sample in respect to the G dispersion (Fig. 24).

The I(D)/I(G) ratio, reported in Fig. 26 for 457 nm, 514 nm and 633 nm excitation wavelength, shows that I(D)/I(G) strongly increases going from lower to higher excitation wavelengths. It has been found that I(D)/I(G) decreases as the graphite crystallite size increases for nanocrystalline graphitic carbon with a cluster size (L_a) larger than 2 nm, (Tuinstra et al., 1970; Ferrari et al., 2000), while I(D)/I(G) increases as the graphite crystallite size increases for disordered carbons with L_a lower than 2 nm, (see 2.1.2) (Chhowalla et al. 2000; Ferrari et al., 2000). Considering the results obtained by HR-TEM (see 4.3.1), graphite crystallite size in soot samples is characterized by L_a lower than 1 nm. At high excitation wavelength, the D peak is mainly due to larger aromatic clusters, thus the I(D)/I(G) ratio is bigger at higher excitation wavelength because bigger clusters give the largest contribution (Ferrari et al., 2000; Ferrari et al., 2001). Thus, the increase of the I(D)/I(G) ratio with the excitation wavelength and as the residence time increases, indicates an increase of the crystalline size, i.e. an increase of the soot structural order, particularly for the benzene soot (LT-B).

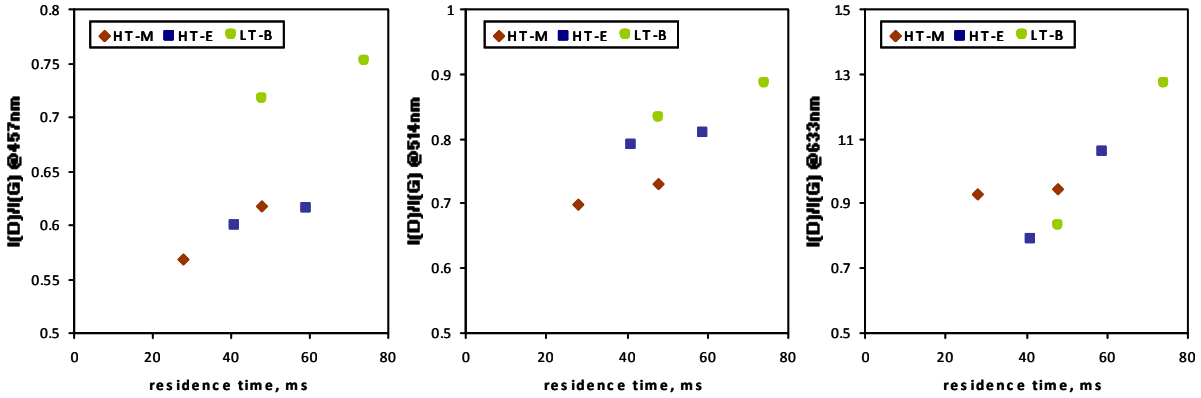

Fig. 26 I(D)/I(G) ratio derived from Raman spectra measured with an excitation wavelength of 633 nm, 514 nm and 457nm for soot sampled in LT-B, HT-E and HT-M as a function of the residence time.

Overall, both the I(D)/I(G) ratio and D peak dispersion trends above described indicate the rise of order as residence time increases and a more aromatic and ordered character of benzene soot in comparison with ethylene and methane soot.

This result is not confirmed by the other parameter considered to be significant of order, namely the FWHM of G peak. Indeed, the FWHM of G peak for a given cluster size should generally decreases as the order increases (Casiraghi et al., 2005).

Thus, the increase of G peak FWHM of soot with residence time, reported in Fig. 27, was unexpected. At the same way it was unexpected that the FWHM of G peak is even higher for benzene soot (Fig. 27). These results can be explained by taking into account for the formation of a greater size variety of clusters as soot formation proceeds, since it has been found that a wider variety of cluster size, in the case of disordered materials, causes a broader line width (Schwan et al., 1996).

The FWHM of D peak also reported in Fig. 27 for sake of completeness, do not show regular trends both as a function of residence time and fuel identity.

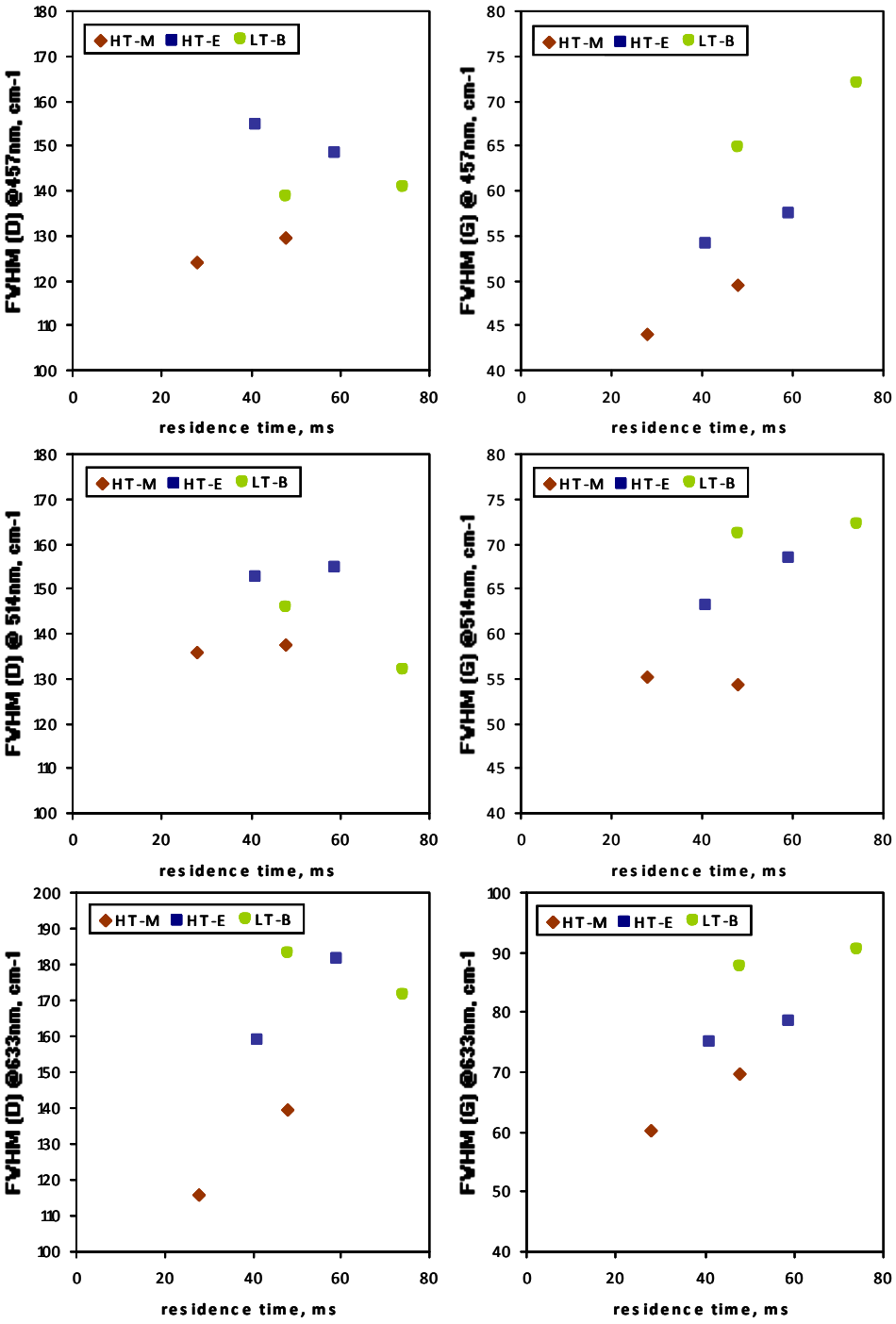

Fig. 27 FWHM of D (left part) and of G (right part) peaks derived from Raman spectra measured with an excitation wavelength of 457 nm, 514 nm and 633 nm for soot sampled in LT-B, HT-E and HT-M as a function of the residence time.

In conclusion, some of the difficulties in interpreting Raman spectra of soot studied in this thesis arise from the complexity of soot nanostructure that appears not adequately represented by a single index corresponding to the degree of graphitization. Nevertheless, it has to be underlined that, to our

knowledge, there are no multiwavelength Raman data for flame-formed soot. In this part of the thesis work it has been shown that the Raman spectroscopic tool appears promising for probing order/disorder also in such complex carbon materials. Further work is necessary to put together all the parameters that could be derived from Raman spectra of soot in order to give an overall and coherent description of the soot structural properties as a function of the combustion parameters.

4.3.4 UV-Visible mass absorption coefficient of soot

In Fig 28 the mass absorption coefficient is reported. It can be noted the increase of the absorption coefficient of benzene soot and the quite small variations and very low values of methane absorption coefficient. Only at the end of the flame ethylene soot reaches values similar to those of benzene. However methane soot has showed to undergo to a strong dehydrogenation (see 4.3.2), even if it starts from higher hydrogen content in comparison with benzene soot.

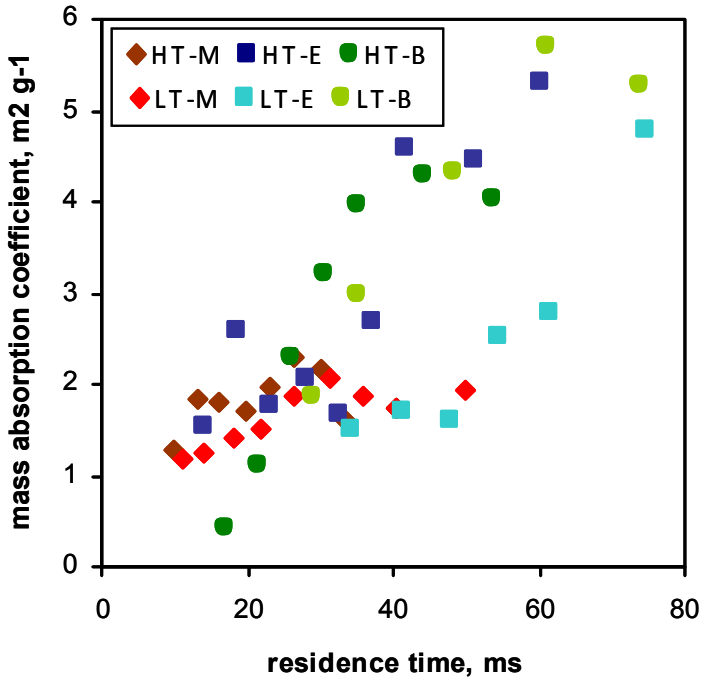

Fig. 28 Mass absorption coefficient of soot for methane, ethylene and benzene flames as a function of the residence time.

To compound the interpretation of these contrasting data is the observation of the increase of the absorption coefficient of ethylene soot to final values comparable to benzene soot, in correspondence of the strong decrease of H/C. The key to understanding these different behaviors

lies on the correlation between the absorption coefficient and the H/C atomic ratio reported in Fig. 29.

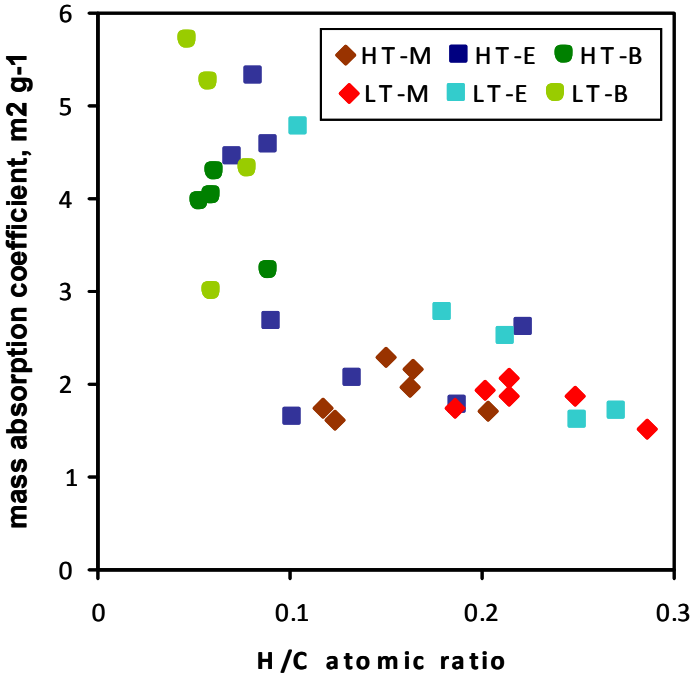

Fig. 29 Correlation between mass specific absorption and H/C atomic ratio of soot for methane, ethylene and benzene flames.

It appears clear that the specific absorption of soot is not sensitive to the variations of H/C in the range from 0.3 down to 0.1, typical of highly hydrogenated soot as methane soot (LT-M and HT-M) and young ethylene soot. As soon as soot dehydrogenates, entering in the lower range of H/C (below 0.1), a sharp increase of the absorption coefficient can be observed, in particular for the HT-E, HT-B and LT-B samples. Since only processes that affect sp^2 cluster size and quality can change the absorptive properties, H/C ratio is a reasonable but imperfect proxy of absorption.

It has to be reminded that many morphological and physico-chemical parameters are known to affect in a complex manner the absorption coefficient and there is still a big debate about the interpretation and reliable evaluation of absorption (extinction) coefficient of carbon materials [Bond at al., 2006; Williams et al., 2007]. However, just focusing on the effect of the elemental composition of carbon materials, it has been assessed that the change of hydrogen level corresponds to the variation of the sp^2/sp^3 ratio in the small- and large-size ring aromatic units leading to the modification of electronic levels responsible for the molecular absorption. These data demonstrate that this should occur only below a critical H/C value of about 0.1 appearing as a threshold value below which most of the soot graphitization occurs and that the absorption coefficient is sensitive to follow this process.

4.3.5 Quantitative FT-IR analysis of carbon materials

As concerns the hydrogen content the evaluation of the absolute value of hydrogen is generally done by combustion analysis (see 4.3.2). However, to give detail on the carbon structure it is important to discriminate between the hydrogen linked to aromatic and aliphatic carbon. Just to this regard, FT-IR analysis of the C–H vibrational modes has considerable value for structural investigations owing to the localized nature of C–H vibrations in the MID range (from 4000 to 400 cm-1). In particular, the peaks in the region around 3000 cm^{-1} can be chosen because they give information on the amount of symmetric and antisymmetric C-H stretching (aromatic and aliphatic). However, just the sensitivity of the frequency and absorption intensity of C-H vibrations to the nature of C–C backbone causes a large variability of response factors generally hindering the quantitative analysis of hydrogen discriminated in aliphatic and aromatic hydrogen.

In the frame of this thesis, a detailed procedure for the quantitative FT-IR analysis of aromatic and aliphatic hydrogen has been set up by using different standard aromatic and aliphatic species and implemented on hydrogen-rich (H/C molar ratio from 0.6 to 1) and hydrogen-poor (H/C molar ratio from 0.1 to 0.3) carbon materials. Carbon materials produced from organic precursors and/or relevant in combustion field as naphthalene pitch, fuel oil asphaltenes and the extractable fraction of flame-formed particulate matter have been analyzed as hydrogen-rich carbon material. Fullerenic soot, carbon black and flame-formed soot have been considered as representative hydrogen-poor carbon materials.

The procedure involved the use of H-C stretch peaks in the 3100-2900 cm^{-1} as well as the peaks due to aromatic C-H out-of-plane bending modes located in the 600-1000 cm^{-1} region. The value of total hydrogen obtained with the FT-IR procedure has been compared with elemental analysis of the same samples to verify the reliability of the FT-IR analysis.

4.3.5.1 Samples and materials

FT-IR analysis was performed to quantify the hydrogen content in carbonaceous materials with a H/C atomic ratio varying from 0.1 to 1.

Standard aromatic and aliphatic compounds were purchased from Sigma-Aldrich.

Hydrogen-rich carbons as naphthalene pitch and asphaltenes, having atomic H/C atomic ratio respectively of 0.6 and 0.95, were used. Naphthalene pitch (Mitsubishi Gas-Chemical Company) is a carbon solid prepared by pyrolysis of naphthalene at 600°C, using HF/BF3 as catalyst [Mochida et al., 1988]. It is considered to be constituted of aromatic units of 0.6–1.5 nm in diameter linked by

phenyl–phenyl or methylene bridges to give a MW in the m/z 400–1000 range as measured by mass spectrometry (Alfè et al., 2008). Asphaltenes were obtained by heptane insolubilization of a commercial heavy fuel oil. They are considered to consists of small fused-ring systems with aliphatic chains (Hortal et al., 2007; Mullins et al., 2012).

Carbon black and fullerenic soot were used as hydrogen-poor carbon materials having a very low H/C atomic ratio (<0.1). Carbon black (Phillips Petroleum) was classified on the basis of ASTM classification as N110 (10–20 nm) carbon black. Fullerenic soot (Aldrich Chemical Company Inc.) was obtained from resistive heating of graphite.

Soot and adsorbed condensed species were obtained from carbon particulates sampled at low (LRT) and high residence time (HRT) in LT-E flame (Russo et al., 2013a). The particulate matter was extracted with dichloromethane to separate soot from DCM-soluble fraction, that strongly interferes in the FT-IR analysis of soot (Carpentier et al., 2012; Santamaria et al., 2010). Thus, their extraction allows the FT-IR analysis of tethered hydrogen of soot with higher (LRT LT-E soot) and lower (HRT LT-E soot) hydrogen content. DCM-soluble fraction, extracted from HRT LT-E particulate, presents a quite constant H/C atomic ratio of about 0.5 independently on the residence time (Ciajolo et al, 1996) and is representative of tarry carbon material mainly constituted of hydrogen-rich compounds as Polycyclic Aromatic hydrocarbons (PAH) (200-400 u) and clusters/aggregates of PAH (400-1000u) (Alfè et al., 2008).

4.3.5.2 Main features of FT-IR spectra and structural insights of carbon materials

Hydrogen-poor and hydrogen-rich carbonaceous materials relevant in the combustion field have been chosen as test cases for developing and implementing the hydrogen quantification procedure based on the FT-IR spectral analysis. Specifically, carbon black and soot sampled at low and high residence times of LT-E flame have been considered as representative of hydrogen-poor carbon materials (H/C<0.3). Fullerenic carbon is also reported as extreme and typical case of hydrogen-free carbon having some peculiar spectral features useful for getting insights on the structure of carbon materials and on the evolution of soot for effect of dehydrogenation/growth process occurring as a function of the residence time.

Naphthalene pitch, heavy fuel oil asphaltenes and DCM-soluble fraction extracted from flame-formed particulate matter have been analyzed as hydrogen-rich carbon materials (0.6< H/C <1). Among them, DCM-soluble fraction was in form of tarry material soluble in CCl_4 so that for them the testing of the calibration factors evaluated on liquid solutions of standards was allowed.

All FT-IR spectra of the carbonaceous materials presented a continuum background, increasing from lower to higher wavenumbers, due to electronic transitions. To put in evidence the vibration bands superimposed on the background, the continuum has been subtracted from the spectra. These spectra, shifted of arbitrary values on the vertical axis for clarity, are compared in Fig. 30.

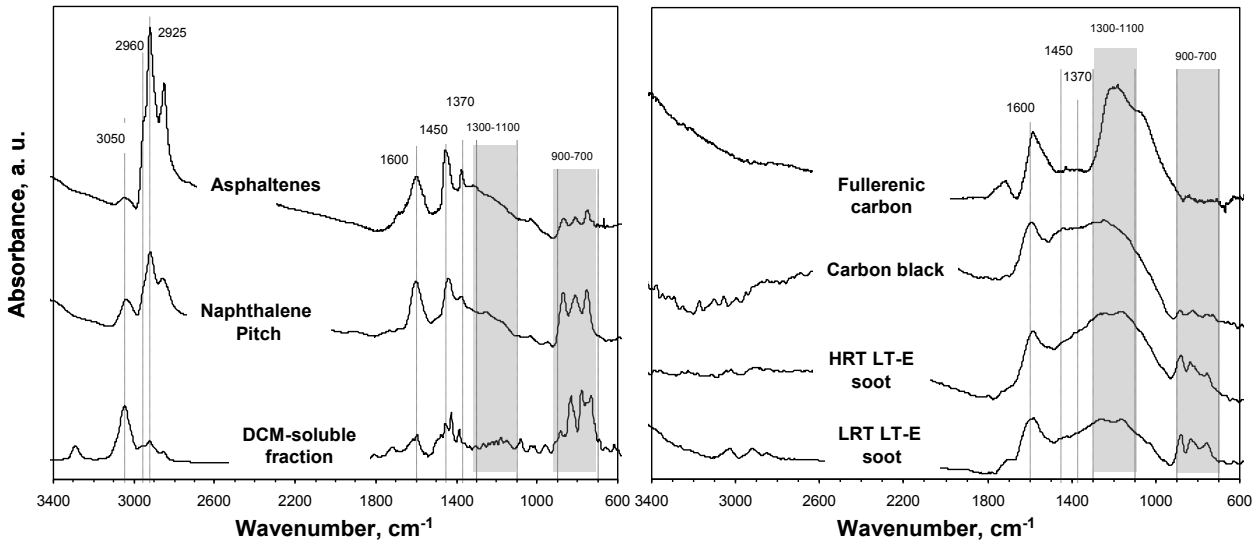

Fig. 30 FT-IR spectra of hydrogen-rich (left part) and hydrogen poor carbons (right part)

Hydrogen-rich carbons exhibit the predominance of both the C-H stretch (in the 3100-2800 cm^{-1}) and the aromatic C-H bending peaks (900-600 cm^{-1}) (left part of Fig. 30). Moreover, it can be also observed that the ratio between the aromatic and aliphatic C-H stretch peaks is very high for the DCM-soluble fraction species, due to the high content of unsubstituted small- to medium-size PAH, and much lower for naphthalene pitch and asphaltenes that are mainly constituted of highly-condensed and substituted- aromatic species.

The higher presence of aromatic and aliphatic C-H stretch peaks cannot be directly related, respectively, to the aromaticity and aliphaticity of carbon-rich materials, as it refers only to hydrogen bound to carbon. Typically, carbon-rich species as large condensed aromatic systems and/or aromatic systems substituted or crosslinked by aliphatic carbon in substitution of the peripheral aromatic hydrogen, present a lower intensity of the aromatic C-H stretch peak as observed in the case of naphthalene pitch and, in particular of asphaltenes (left part of Fig. 30). It can be noted that to the lower ratio between the aromatic and aliphatic C-H stretch peaks of naphthalene pitch and asphaltenes, corresponds the rise of the 1600, 1450 and 1370 cm^{-1} peaks. The 1600 cm^{-1} peak, due to the C=C (sp^2) stretching mode, is generally activated in the presence of the irregularity/dissymmetry of the aromatic moiety caused by whichever kind of substitution (Akhter et al., 1985; Galvez et al., 2002). The band at 1450 cm^{-1} involves both C=C stretching mode and

CH2 and CH3 bending motion, the latter giving rise also to the 1370 cm^{-1} band (Carpentier et al., 2012). In the case of asphaltenes, where the aliphatic stretch band is very high, the dissymmetry is mainly caused by substitution of peripheral aromatic hydrogens with aliphatic groups. In the case of naphthalene pitch the higher dissymmetry of carbon network due to the presence of CH2 groups bridging aromatic moieties or forming non-hexagonal rings is suggested in the following detailed analysis of the peaks due to the symmetric CH2- stretch.

The absorption in the 1600-1000 cm^{-1} region becomes predominant in the whole spectra of carbon black and soot (right part of Fig. 30) and the peaks at 1470 and 1370 cm^{-1} disappear merged in a broader massif in the 1300-1100 cm-1 region of higher intensity as hydrogen content decreases. Similarly, as with Raman the whole 1600-1000 cm^{-1} band has been named defect band and assigned to sp^3 defects at the edge, in form of aliphatic crosslinkage, and in form of non-hexagonal rings within the aromatic sp^2 sheet (Carpentier et al., 2012). The dominance of sp^2 over sp^3 coordination (Muller et al., 2007) and the low optical band gap of carbon black and soot (Russo et al., 2013a) allows to ascribe also this band to the sp^2 bonds and the variety of sp^2 clusters (Rodil, 2005).

For the fullerenic carbon, the 1300-1000 cm^{-1} band appears to be clearly distinct in respect to the 1600 cm-1 peak and shifted toward lower wavenumber, i.e. at 1200 cm^{-1} (Fig. 30). The presence of odd-carbon number ring is known to cause the bending/curvature of graphene structures typically present in soot sampled in fullerene-forming premixed benzene flames (Grieco et al., 2000). In agreement with this finding, benzene soot has shown to present the 1300-1100 cm^{-1} band more shifted toward 1200 cm^{-1} already at early residence times (Russo et al., 2012). At a lower extent the shift of the band toward 1200 cm^{-1} can be noticed also in the soot that has undergone dehydrogenation/annealing at longer residence times (HRT LT-E soot) (Fig. 30).

4.3.5.3. FT-IR analysis of hydrogen in carbon materials

For hydrogen-rich carbons, the analysis of both aromatic and aliphatic hydrogen has been performed in the infrared spectral region located in the high frequency region, where peaks due to sp^2 aromatic C–H stretch (3100-3040 cm^{-1}) and to sp^3 C-H stretch (3000-2800 cm^{-1}) occur (Fig. 30). For hydrogen-poor carbons having very low C-H stretch signals, the aromatic C-H bending peaks (900-600 cm-1) have been used for the analysis of aromatic hydrogen.

As previously observed (Santamaria et al., 2010; Ciajolo et al., 1998; Pino et al., 2008; Galvez et al., 2002; Schnaiter et al., 1999), the aromatic C-H stretch of carbon materials typically occurs as a broad unique peak at about 3050 cm^{-1}. The different vibrations of aliphatic CH3, CH2 and CH groups, in the 3000-2800 cm^{-1}, typical of free molecules, are not clearly resolved and they are

present in form of a broad absorption peaked at 2925 cm^{-1}. Nevertheless, the coupling of vibrations can be considered negligible, as assessed in previous work on amorphous carbons (Ristein et al., 1998), justifying the transfer of vibration frequencies from standard molecules to the disordered carbons analyzed in this work.

The deconvolution of the FT-IR spectra by sum of gaussian profiles, has been carried out in the 3150-2750 cm-1 region for the precise assignment of the bands and for the quantitative evaluation of both aliphatic and aromatic hydrogen content on the basis of the height of each individual band. The deconvolution has been implemented on the spectra of carbon materials exhibiting a high C-H stretch signal/noise (asphaltenes, naphthalene pitch, DCM-soluble fraction and LRT LT-E soot) as shown in Fig 31 where their spectra and deconvolution profiles are reported.

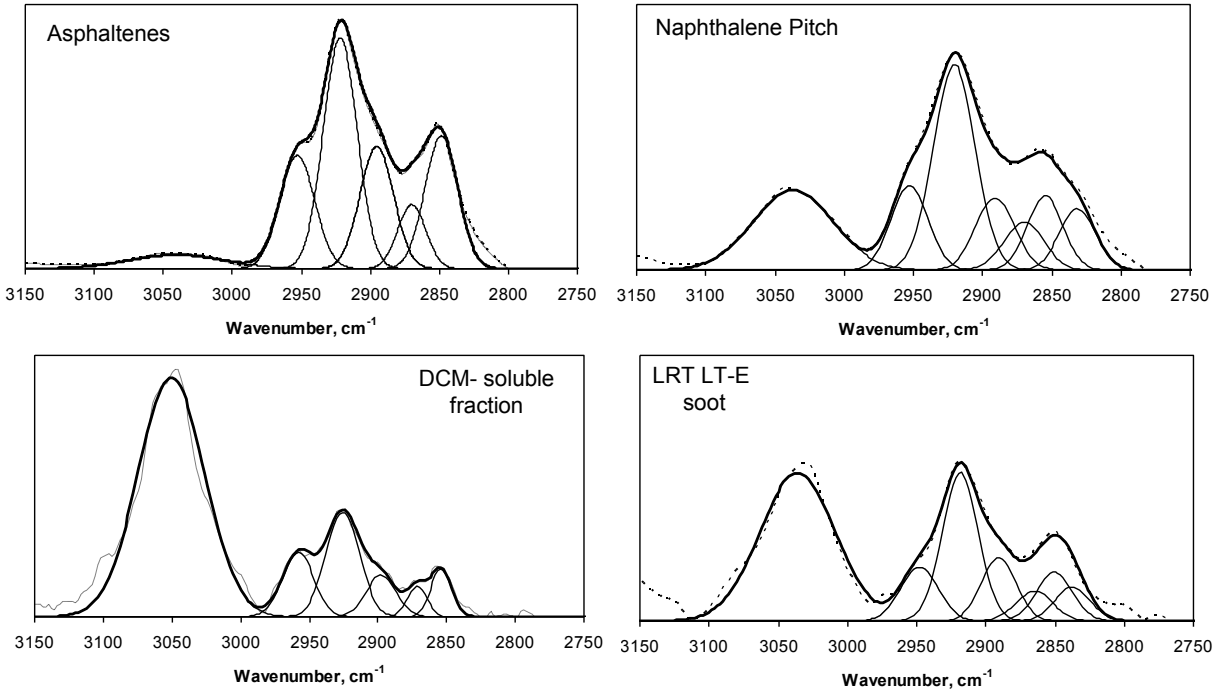

Fig. 31. FT-IR spectra (dashed lines) of carbon materials in the C-H stretch region. The individual Gaussians obtained by deconvolution of the spectrum as a sum of Gaussian bands are also reported (continuous line).

The peaks at 2870 and at 2960 cm^{-1} are assigned to the symmetric and asymmetric -CH3 stretch respectively. The peaks at 2855 cm^{-1} and at 2925cm^{-1} are respectively due to asymmetric and symmetric stretch of -CH2 groups belonging to aliphatic chains. The peak at about 2895 cm^{-1} is assigned to aliphatic C-H stretch of a tertiary carbon atom, even though it has to be considered that also the symmetric –CH2 Fermi resonance arises at this wavenumber (Conboy et al., 1997; Carpentier et al., 2012).

Interestingly enough, an additional peak around 2830 cm^{-1} comes out from the deconvolution of the spectra of naphthalene pitch and LRT LT-E soot sample. From the detailed analysis of each stretch peak in comparison with standard species, which will be shown in the following sections, this peak is attributed to the symmetric stretch of -CH2 groups bridging aromatic rings, possibly forming non-hexagonal rings.

For the quantification of aromatic and aliphatic hydrogen, the C-H stretch peak positions were allowed to vary in a range enough wide to include the observed position and widths of each peak. The main features of the peaks used for the deconvolution are reported in Table 9. It can be noticed that going from hydrogen-rich to hydrogen-poor carbons, the symmetric stretch peak width increases, approaching values as those reported in previous work on soot carbon (Pino et al., 2008).

		C=C-H	$C\text{-}H3_{asym}$	$C\text{-}H2_{asym}$	C-H	$C\text{-}H3_{sym}$	$C\text{-}H2_{sym}$	$C\text{-}H2^{bridge}_{sym}$
Asphaltenes	wavenumber (cm^{-1})	3041	2953	2922	2895	2870	2849	
	bandwidth (cm^{-1})	35	13	12	12	10	12	
Naphthalene Pitch	wavenumber (cm^{-1})	3037	2953	2920	2891	2870	2855	2831
	bandwidth (cm^{-1})	29	13	15	14	14	13	13
DCM-soluble fraction	wavenumber (cm^{-1})	3050	2958	2926	2898	2872	2854	
	bandwidth (cm^{-1})	24	11	12	11	7	8	
LRT LT-E Soot	wavenumber (cm^{-1})	3036	2948	2918	2891	2865	2850	2838
	bandwidth (cm^{-1})	27	13	13	12	13	13	13
Standards	wavenumber (cm^{-1})	3053	2962	2924	2890	2871	2859	2834
	bandwidth (cm^{-1})	17	9	10	13	6	6	5

Tab.9 Centres and widths of Gaussian functions coming out from the deconvolution of FT-IR spectra of carbon samples in the C-H stretching region.

The selection of standard species used for the evaluation of aromatic and aliphatic hydrogen (CH3, CH2, CH) has been performed after an accurate analysis of the position, shape and intensity of peaks of standard species in comparison with the same peaks of carbon materials. The C-H stretch peaks have to be attributed to alkyl groups linked to aromatic moieties rather than to pure aliphatic hydrocarbons that are quite absent in both hydrogen-poor carbons and in hydrogen-rich carbons as DCM-soluble fraction species, asphaltenes and naphthalene pitch, composed of PAH and high molecular weight aromatics (Apicella et al., 2004; Alfè et al., 2008). By consequence, the standard species selected for the calibration factor evaluation of aromatic and aliphatic hydrogen include only the aromatic and alkyl-substituted aromatics listed in Table 10 along with the calculated calibration factors evaluated as follows.

For a mole of given standard St, the number of hydrogen H for a certain type of functionality f, n_{Hf}^{St}, has been calculated as $n_f^{st} * n_{Hf}$ where n_f^{St} is the number of functionalities present in the standard s

and n_{Hf} is the number of hydrogens present in the specific functionality, i.e. 3 for the methyl functionality.

The calibration factor, derived from the spectra of a standard St for the functionality f, is defined as reported in formula 1, where C^{St} is the standard concentration (μg/ ml_{CCl4} for liquid solution and μg/ mg_{KBr} for Kbr dispersion), L^{St} is the optical path equal to 1 cm for solutions and to the average width of the KBr disks (0.035 cm), MW^{St} is the standard molecular weight, AW_H is the atomic hydrogen weight and I_f^{St} is the height of the peak corresponding to the specific functionality.

$$CF_f^{St} = \frac{C^{St} * n_{Hf}^{St} * AW_H}{I_f^{St} * MW^{St} * L^{St}} \qquad (1)$$

CF^{st} is expressed in μg_H*cm/ml_{CCl4} for liquid solution and in μg_H*cm/mg_{KBr} for KBr dispersion.

When for a specific functionality more CF, derived from different standards, are available and these are suitable for the examined sample, an average $\overline{CF}$ has been used.

Given a sample S, with a certain concentration C^S expressed in $\mu g^S/ml_{CCl4}$ for liquid solution and in $\mu g^S/mg_{KBr}$ for KBr dispersion, the weight fraction of hydrogen W_{Hf}^S for a specific functionality is given by:

$$W_{Hf}^S = \frac{I^S * \overline{CF_f}}{C^S * L^S}$$

where L^S and I^S are respectively the optical path and the height of the peak corresponding to the specific functionality f in the sample spectrum. The total weight hydrogen fraction W_H^S for m hydrogen functionalities present in the sample is given by $W_H^S = \sum_{f=1}^{m} W_{Hf}^S$

Due to the absence of other kind of atoms, the weight fraction of carbon has been derived for difference to calculate the H/C atomic ratio.

The similarity of calibration factors of species analyzed in both liquid and solid phase, reported in Table 10, allows the use of CF derived also from standard species in liquid solution as n-propyl-benzene and isopropyl-benzene, for the evaluation of hydrogen in solid dispersions of the samples.

standard	CF [μg*cm/ml$_{CCl4}$, (μg*cm/mg$_{KBr}$)]			
	C-H3 (2960)	C-H2 (2925)	C-H (2895)	C=C-H [3100-3040]
1-methyl pyrene				89.2, (106.2)
9-methylanthracene				138.7, (159.1)
acenaphthene		61.2, (60.0)		113.2, (142.0)
anthracene				119, (151.4)
benzo(a)pyrene				144.5, (132.2)
isopropyl-benzene	34.5		25.4	
n-propyl-benzene	26.5	39.4		

Tab.10. Hydrogen calibration factors of standard species in the C-H stretching region. Calibration factors evaluated from solid dispersions are given in parentheses.

Aromatic hydrogen (C-H stretch) (3050 cm^{-1})

Among aromatics listed in Table 10, n-propyl- and isopropyl-benzene as well as benzene, coronene and phenanthrene (not reported in the table), were not considered for the aromatic hydrogen quantification since they exhibit multiple peaks in the 3100-3000 cm^{-1} wavelength range. It can be seen that the aromatic C-H calibration factors range from about 100 to 150 (Table 10). Figure 32 reports the spectra of some aromatic standard species in the 3150-2800 cm^{-1} region. It can be noted that the peak position of the aromatic C-H stretch (right part of Fig.32) varies in 3060-3040 cm^{-1} range in dependence on the species. This variability justifies the large width of aromatic C-H stretching peak measured in the samples (Tab.9) since peaks due to different aromatic species are present causing their merging in a unique broad absorption peaked around 3050 cm^{-1}.

Aliphatic hydrogen (-CH3 stretch) (2960 cm^{-1})

The aliphatic hydrogen, present in form of -CH3, has been evaluated considering the CF of the peak at 2960 cm-1 due to the asymmetric –CH3 stretch (Table 10). This peak appears in n-propyl- and isopropyl-benzene (left part of Fig.32).

By contrast, this peak appears to be located at 2930 cm^{-1} in methyl-substituted PAH like 9-methyl-anthracene, 9-10-dimethyl-anthracene, 3,6-dimethyl-phenanthrene and 1-methyl-pyrene, whose spectra are reported in Fig. 33. Moreover, the -CH3 stretch peak of alkyl-substituted anthracenes is broader in comparison to n-propyl-benzene and presented a very high calibration factor (~130). This peak is even splitted in two sharp peaks around 2930 cm^{-1} for 1-methyl-pyrene. The great variability in the -CH3 stretching calibration factors is not surprising since it has been found that for this mode the calibration factor depends on the hybridization of neighbour carbon atoms. (Jacob et al., 1996, Ristein et al., 1998).

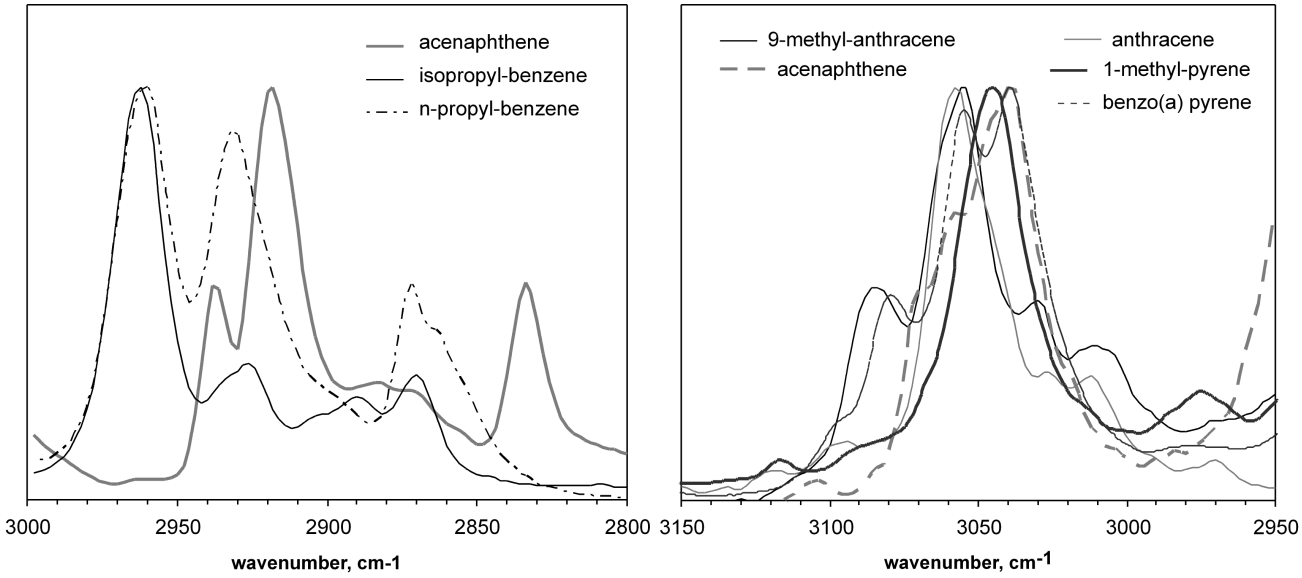

Fig. 32 FT-IR spectra of selected standard species, dissolved in CCl_4,in the C-H stretching region (3150-2800 cm^{-1})

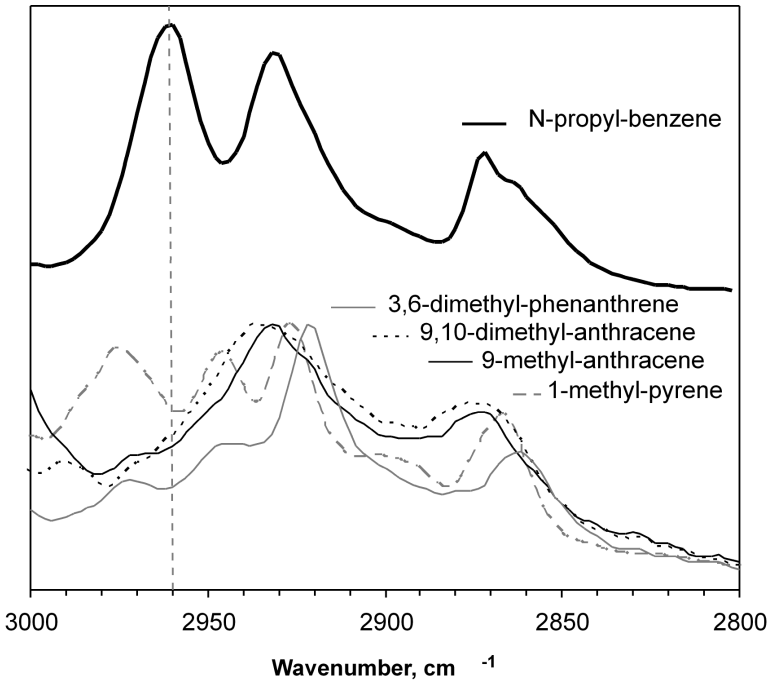

Fig. 33 FT-IR spectra of N-propyl benzene and some methyl-substituted PAH in the 3000-2800cm^{-1} range.

When the –CH3 group is directly linked to an aromatic ring, the -CH3 stretch peak shifts at lower wavenumber and the strength of this vibration strongly decreases, leading to a very high calibration factor and thus, to an overestimation of the hydrogen content. By consequence, the presence in the samples of methyl groups directly linked to the aromatic moieties can be excluded and the

calibration factors of –CH3 groups of the alkyl chains of n-propyl-benzene and isopropyl-benzene, have been assumed to be more reliable for the -CH3 evaluation of carbon samples.

Aliphatic hydrogen (-CH2 stretch) (2925 cm-1)

The quantification of aliphatic hydrogen present in form of –CH2 has been done on the predominant peak located at 2925 cm^{-1} due to the asymmetric stretch of –CH2.

As mentioned before, for some carbons as naphthalene pitch and LRT LT-E soot (Fig 31) it has been necessary to add another Gaussian function with a maximum around 2830 cm^{-1}. This peak can be attributed to -CH2 groups bridging aromatic rings and forming odd-carbon number rings enclosed in the aromatic network. This attribution is corroborated by the spectrum of acenaphthene containing two -CH2 groups bridging two condensed aromatic rings, also reported in Fig. 32. In fact, it can be noted that the symmetric -CH2 stretch of acenaphthene is shifted at lower wavenumber (2839 cm^{-1} instead of 2850 cm^{-1}), indicating a peculiar behaviour of this type of CH2. (Pino et al., 2008; Gotoh et al., 1999). To take into account for the different nature of the –CH2 groups, a CF for the 2925 cm^{-1} stretch of 49.7 $\mu g*cm*mg_{KBr}$,averaged between acenapthene and n-proyl-benzene, has been used for naphthalene pitch and LRT LT-E soot, while for asphaltenes and DCM-soluble fraction, the CF of the 2925 cm^{-1} stretch of n-propyl-benzene has been used.

Aliphatic hydrogen (-CH stretch) (2895 cm^{-1})

The peak at 2895 cm^{-1} has been ascribed to the tertiary aliphatic C-H stretch (Table 9) and the CF of isopropyl-benzene has been used for the quantification of this kind of hydrogen (Table 10). The possible contribution of the symmetric –CH2 Fermi resonance, resulting from interaction of an overtone of the –CH2 bending mode with the –CH2 symmetric stretch, at this wavenumber (Conboy et al., 1997) has been discarded since overtones are usually of very low intensity.

Main features and calibration factors of the C-H bending peaks (900-700 cm^{-1})

The quantitative procedure based on the C-H stretch evaluation can not be applied to hydrogen-poor materials as carbon black and HRT LT-E soot having an H/C ratio lower than 0.1 and showing very weak negligible C-H stretch peaks (right part of Fig. 30). However, for these carbon samples, the aromatic C-H bending vibrations of isolated and adjacent hydrogens of aromatic systems appear to persist in the range between 900 and 700 cm^{-1}. This indicates that these vibrations are much stronger than the corresponding stretching vibrations and can be used to quantify the aromatic hydrogen when the stretching signal is too low to be detected, or when the presence of water makes

difficult a right evaluation of aromatic stretching peak height due to the distorted baseline for effect of O-H stretch peak at around 3200 cm^{-1}.

It is well known that the aromatic hydrogens present the so-called out-of-plane (OPLA) bending peaks in relation to the substitution pattern of the aromatic system. As shown in Fig. 34, reporting the spectra focused in the 950-650 cm^{-1}, the OPLA peaks occur at decreasing frequencies according to the number of CH bonds involved in the vibration that are located at the edge of the polyaromatic system and named solo, duo, trio and quatro (Centrone et al., 2005). The assignments of each OPLA bending peak and the CF have been done on spectra of representative aromatic standard species, reported in Table 11.

	CF (μg_H*cm/mg_{KBr})			
standard	C=C-H [890-870]	C=C-H [850-810]	C=C-H [790-750]	C=C-H [750-720]
1-methyl-pyrene		8.6	18.9	
9-methyl-anthracene	4.3			17.1
acenaphthene			23.4	
anthracene	4.7			19.1
biphenylene				22.0
coronene		10.3		
fluoranthene			14.0	12.9
phenanthrene		5.7		18.3

Table 11. Aromatic C-H calibration factors of standard species in the out-of-plane bending region.

The spectral analysis of PAH and alkyl-substituted PAH standard used in this work as well as of PAH spectral library (Nist Chemistry Webbook) allows to assess that isolated hydrogens (solo) are located in the 890-870 cm^{-1} range (9-methyl-anthracene at 886 cm^{-1}, anthracene at 884 cm^{-1}) whereas two-adjacent hydrogens (duo) are located between 850 and 810 cm-1 (1-methyl-pyrene at 840cm^{-1}, coronene at 847cm^{-1}, phenanthrene at 817cm^{-1}).

Three-adjacent hydrogens (trio) are detected in the 790-750 cm^{-1} region (1-methyl-pyrene at 755cm^{-1}, acenaphthene at 784cm^{-1}, fluoranthene at 775cm^{-1}). Four-adjacent hydrogens (quatro) are detected in the 750-720 cm^{-1} region (9-methyl-anthracene at 723cm^{-1}, biphenylene at 729cm^{-1}, anthracene at 725cm^{-1}, phenanthrene at 731cm^{-1}, fluoranthene at 746cm^{-1}).

Similarly to the aliphatic C-H stretch, the OPLA bands of carbon samples, reported in Fig. 34, appear broad and strongly overlapped, thus the individual aromatic C-H bending peaks have been obtained by deconvolution of the OPLA region into six component absorption bands. The output of the deconvolution procedure is also reported in Fig. 34 whereas the spectral features of the peaks obtained by deconvolution are reported in Table 12. The width of the OPLA peaks in the standards

species has been found much lower (5 cm^{-1}) than the width measured on the deconvoluted peaks (>10 cm^{-1}).

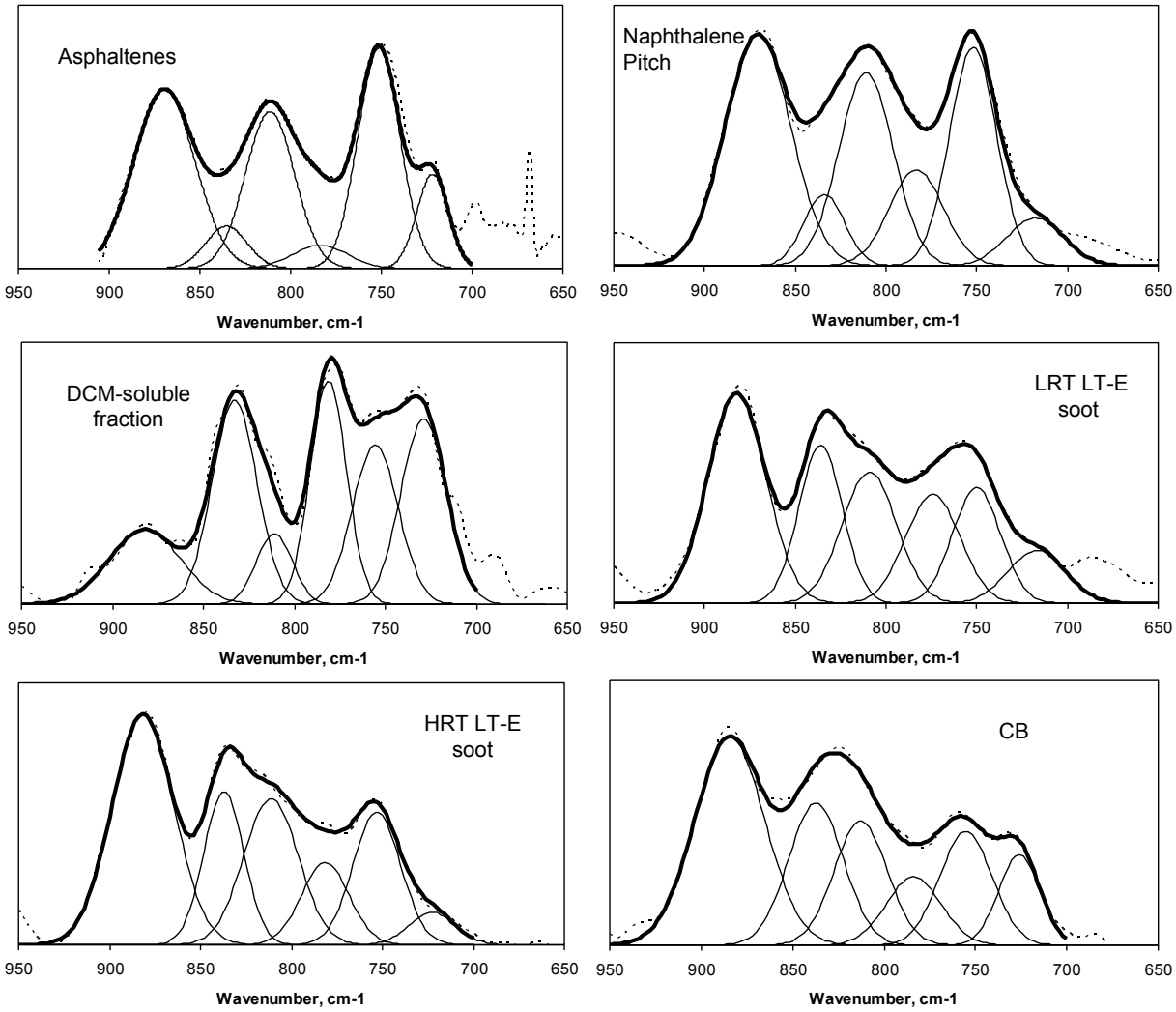

Fig .34 FT-IR spectra (dashed lines) of carbon materials in the C-H out-of-plane bending region. The individual Gaussians obtained by deconvolution of the spectrum as a sum of Gaussian bands are also reported (continuous line).

On the basis of the standard species spectra, the peak at ~ 880cm^{-1} is assigned to solo hydrogens, the two peaks in the range 850-810 cm^{-1} are ascribed to duo hydrogens, the peak at ~770cm^{-1} is due to trio hydrogens, the peak at ~ 750 cm^{-1} is due to both trio and quatro hydrogens while the peak at ~ 730cm^{-1} is due to quatro hydrogens.

		solo	duo		trio	trio-quatro	quatro
Asphaltenes	wavenumber (cm^{-1})	870	835	811	784	751	722
	bandwidth (cm^{-1})	17	11	14	12	12	9
Naphthalene Pitch	wavenumber (cm^{-1})	871	834	811	783	754	734
	bandwidth (cm^{-1})	18	11	15	15	13	16
DCM-soluble fraction	wavenumber (cm^{-1})	882	833	811	781	756	729
	bandwidth (cm^{-1})	20	12	10	10	13	13
LRT LT-E Soot	wavenumber (cm^{-1})	882	836	809	774	750	717
	bandwidth (cm^{-1})	16	12	15	15	13	16
HRT LT-E Soot	wavenumber (cm^{-1})	882	837	811	781	753	723
	bandwidth (cm^{-1})	17	11	15	13	13	13
CB	wavenumber (cm^{-1})	884	837	813	784	755	726
	bandwidth (cm^{-1})	19	15	14	15	14	11
Standards	wavenumber (cm^{-1})	885	844	816	780	750	728
	bandwidth (cm^{-1})	5	5	6	6	5	5

Table 12. Centres and widths of Gaussian function coming out from the deconvolution of FT-IR spectra of standards and samples in the OPLA region.

In the case of asphaltenes, richer in aliphatic functionalities the lower width (9 cm-1) and the position of the quatro peak at 722 cm^{-1} suggests the possible contribution of the rocking aliphatic CH2 vibration, arising at 720 cm^{-1} and typical of long CH2 chains (more than four contiguous groups). It can be also noticed that asphaltenes and naphthalene pitch present the solo peak at 870 cm^{-1}, more typical of aromatic rings substituted with aliphatic chains, in respect to the peak at 880 cm^{-1} observed for the other carbon samples and typical of zigzag-edged aromatic species.

		C-H stretching region					C-H bending region				
		CH3	C-H2	C-H	Aliph	C=C-H	C=C-H	SOLO	DUO	TRIO	QUATRO
Asphaltenes	W%	1.47	3.88	1.32	6.67	0.83	0.58	0.05	0.10	0.20	0.22
	X%	22.06	58.11	19.82				8.25	18.01	35.14	38.60
Naphthalene Pitch	W%	0.45	1.88	0.36	2.69	2.05	1.63	0.17	0.38	0.58	0.50
	X%	16.88	69.88	13.24				10.46	23.46	35.48	30.61
DCM-soluble fraction	W%	0.19	0.39	0.10	0.68	2.78	2.66	0.07	0.48	1.14	0.97
	X%	27.35	57.79	14.85				2.52	18.16	42.94	36.38
LRT LT-E soot	W%	0.08	0.38	0.08	0.55	1.22	1.14	0.12	0.33	0.41	0.27
	X%	15.40	69.58	15.02				10.88	29.40	36.25	23.47
HRT LT-E soot	W%				0.18*		0.75	0.09	0.24	0.25	0.16
	X%							12.48	31.79	33.71	22.02
CB	W%						0.54	0.06	0.15	0.15	0.17
	X%							11.24	28.13	28.27	32.36

Table 13 Weight fraction percentages (W%) of hydrogen present as CH3, CH2, CH aliphatic groups and as aromatic solo, duo, trio and quatro CH and percentage (X%) of CH3, CH2, CH to the total aliphatic hydrogen and of solo, duo , trio and quatro to the total aromatic hydrogen.

Quantitative analysis of aromatic and aliphatic hydrogen

The height of each stretching and bending C-H peaks coming out from deconvolution of the carbon sample spectra above described has been multiplied by the appropriate CF (Table 10 and Table 11) in order to quantify the aliphatic and aromatic hydrogen weight percentages reported in Table 13.

Consisting with the qualitative analysis of the spectra (Fig.30) asphaltenes and naphthalene pitch are characterized by the higher percentage of total aliphatic hydrogen, 6.67 and 2.69 wt% in respect to the very low aliphaticity of DCM-soluble fraction. Aliphatic groups are negligible or absent in LRT LT-E soot, HRT LT-E soot and carbon black. The percentages of CH3, CH2 and CH hydrogen in respect to the total aliphatic hydrogen are also reported in Table 13 to follow the relative abundance of each aliphatic group. A higher CH2 abundance can be noticed for the naphthalene pitch and for the LRT soot attributed to the larger presence of CH2 bridging aromatic units on the basis of the spectral analysis of CH2 stretch before described. Longer linear aliphatic groups are present in the asphaltenes as testified by the larger abundance of CH3 and lower presence of tertiary CH groups. Consistently with the lower aliphaticity, naphthalene pitch also exhibits a large presence of aromatic hydrogen similar to that of DCM-soluble fraction.

The quantitative analysis of aromatic hydrogen in the bending OPLA region gives some interesting insights on the edge of the aromatic systems, in particular for molecularly heterogeneous structures. It is noticeable that the solo hydrogen results to be generally less abundant in respect to the other hydrogens (Tab. 13) in spite of the apparent predominance and/or high contribution in the OPLA region of the solo peak, (Fig. 34), the latter being due to the much lower calibration factor (high response) in comparison to the other aromatic hydrogens (Tab. 11).

The population of aromatic hydrogens also reported in Table 13 as percentage of the different hydrogens in respect to the total aromatic hydrogen (evaluated on the bending) gives out an overall view of their relative contribution. As expected, the solo hydrogen takes into account for about 2% of the aromatic hydrogen whereas trio and quatro hydrogens are the most abundant in the case of DCM-soluble fraction, mostly constituted of small size unsubstituted-PAH molecules. Even for larger size aromatic structures, as those contained in asphaltenes and naphthalene pitch, and for carbon black and soot the population of solo hydrogens takes into account for only 10% of the total aromatic hydrogen as opposed to the trio and quatro hydrogens taking into account for most of the aromatic hydrogen. Indeed, the expected decrease of the relative population of trio and quatro structures in favour of solo and duo (Centrone et al., 2005) for effect of the larger size of aromatic clusters is not found. For interpreting this unexpected result, we can recall the issue of edge topology (armchair or zigzag) in relation with aromaticity. It can be speculated that armchair edges, mainly characterized by duo and trio hydrogens, are more abundant since they are energetically

stable due to a large number of aromatic sextets. By contrast, zigzag edges, mainly characterized by solo hydrogens, are less aromatic and, by consequence, energetically unstable in agreement with Clar's rule (Enoki, 2012).

The OPLA analysis is particularly useful also for an indirect evaluation of the total aliphatic hydrogen of hydrogen-poor carbons as soot HRT LT-E reported in Table 13, marked with an asterisk. It has been evaluated from difference between the total hydrogen content obtained from elemental analysis and the aromatic hydrogen content evaluated from the OPLA bending region. Moreover, even though the HRT LT-E soot spectrum in the C-H aliphatic stretching region is very noisy, a broad band at 2915cm^{-1} and at 2840cm^{-1} could be distinguished, leading to assign this aliphatic hydrogen mainly to CH2 groups bridging aromatic rings and tertiary hydrogen.

Finally, the H/C atomic ratio of carbons analyzed in this work has been evaluated by summing the individual hydrogen percentages obtained by quantitative FT-IR analysis. Table 14 reports a comparison between the H/C ratio measured by elemental analysis (EA) and by FT-IR analysis based on the aliphatic and aromatic CH stretching, named $(H/C)_{ST}$, and on the aliphatic CH stretching and aromatic CH bending named $(H/C)_{Bend}$. It can be noted that the agreement between the H/C ratio measured by elemental analysis and derived from both FT-IR procedures is quite satisfactory .

	$(H/C)_{EA}$	$(H/C)_{ST}$	$(H/C)_{Bend}$
Asphaltenes	0.95	0.97	0.94
Naphthalene Pitch	0.60	0.60	0.54
DCM-soluble fraction	0.45	0.43	0.41
LRT LT-E soot	0.21	0.22	0.21
HRT LT-E soot	0.11	-	0.09
CB	0.06	-	0.06

Table 14 Atomic H/C ratio as measured from elementary analysis $(H/C)_{EA}$ and FT-IR spectroscopy evaluated on aliphatic and aromatic CH stretching $(H/C)_{ST}$ and on aliphatic CH stretching and aromatic CH bending $(H/C)_{Bend}$.

4.3.5.4 FT-IR spectroscopy of soot

Ongoing work will be focused on a systematic application of the described procedure for the quantitative FT-IR analysis of aromatic and aliphatic hydrogen to soot carbon. Soot FT-IR spectra,

reported in Fig.35, present the main features typical of hydrogen poor carbon (see 4.3.5.2). At HRT the signal to noise ratio is always very low, increase in the sample concentration in the KBr powder is required for a correct application of the procedure in order to follow in details the soot hydrogen evolution inside a flame.

From the qualitative point of view, the high hydrogen content of methane soot, from the beginning to the end of the flame, can be ascribed mainly due aliphatic and aromatic hydrogen, moreover the persistence of aliphatic hydrogen also at HRT can be noted. For ethylene soot aliphatic and aromatic hydrogen has been found to decrease as the residence time increases, while for benzene soot a C-H stretch signal can not be detectable even a LRT and whichever the temperature.

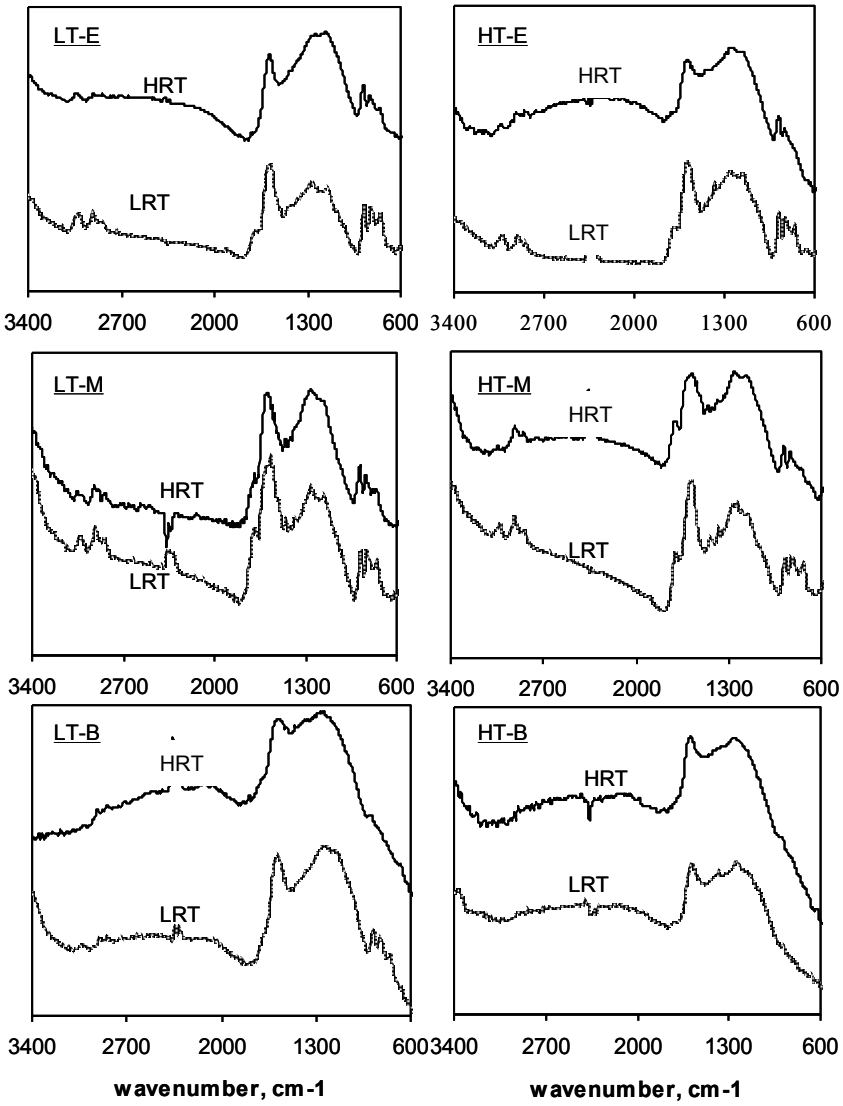

Fig.35 FT-IR spectra of benzene, methane and ethylene soot sampled at LRT and HRT

5 Conclusions

Structural data were gathered on carbon particulate (soot and soot precursors) sampled in methane, ethylene and benzene premixed flames by using many diagnostic tools for understanding the complex structure and formation mechanism of carbon particulate derived from combustion processes.

The order/disorder character, mainly linked to the sp^2/sp^3 features i.e. to the aromatic/aliphatic nature of soot, was followed in detail by measuring typical optical parameters of UV-Visible, FTIR and Raman spectroscopic methods purposely developed and implemented on carbon particulate matter and on its size/MW components as separated by chromatographic methods.

The UV-Visible spectral features of carbonaceous species distributed in a wide range of MW (from 200 to 1E11u) were found to be mainly affected by the higher MW species, included in the 1E8-1E11u range. Thus, the great advantage in separating the contribution of species having different size and composition, regards the possibility to follow their role in the soot formation process and the structural evolution of each class of components, even of minor and less absorbing components obscured by the main and highly absorbing components.

In benzene (LT-B) and ethylene (HT-E) flames just these higher MW species/particles showed to undergo graphitization/growth reactions during the formation process of carbonaceous species while the aromatic species of lower MW, from large PAH to clusters of PAH included in the 200-1E8u range, did exhibit neither a continuous molecular growth nor an internal structure transformation. This suggests that they merely aggregate/coagulate, without undergoing transformation, directly participating to the formation of large carbon particles that, instead, are subjected to dehydrogenation/annealing reactions.

The values of the optical band and of the UV maximum absorption position were used to get details on the carbon network structure in terms of sp^2 and sp^3 sites and size of the aromatic units. By means of this spectral analysis the larger MW species identified in the DCM-soluble fraction, beside fully-condensed PAH from two- to seven rings, were found to be mainly composed of relatively small PAH clustered together, rather than highly-condensed large PAH. This suggests that the clustering process, with the possible intervention of aliphatic species, is an important mechanism through which inception and further growth of soot particles occur.

The high content of hydrogen of methane soot, from the beginning to the end of the flame, was shown to be mainly due to aliphatic hydrogen in form of methylene CH_2 groups as measured by FT-IR spectroscopy. This can be attributed to the chemical environment, rich of unburned methane fuel, hydrogen and light aliphatic hydrocarbon products, in which soot inception occurs. By consequence,

in the first nuclei of methane soot the intervention of aliphatic groups is massive and causes the high disordered structure. The significant persistence of methylene groups, even for higher temperature conditions, suggests that methylene groups act as cross-linkers cementing the aromatic layers and limiting the occurrence of further dehydrogenation/graphitization process in the investigated residence time range. It can be suggested that methane soot behaves as the so-called non-graphitizing carbon for which the graphitization process, in turn resulting in the absorption coefficient increase, occurs to a lower extent (Franklin, 1951). However, it cannot be excluded that the lower dehydrogenation degree of methane soot could be due to the chemical and thermal environment in which methane soot is formed and transformed. In any case,, it can be assessed that just the methylene groups and the higher microporosity of methane soot causes it to be more susceptive to oxidation as confirmed by the lower combustion temperature of methane soot in comparison to benzene and ethylene soot (Alfè et al. 2009; Alfè et al. 2010).

Benzene soot is more aromatic from the beginning presenting a negligible content of hydrogen, mainly aromatic hydrogen, since it nucleates before the complete depletion of benzene fuel and oxygen, in a very reactive chemical environment rich of aromatic radicals and species, and poor of hydrogen and light aliphatic hydrocarbons. It incorporates low amount of hydrogen and aliphatic species and is also less liable to oxidation (Alfè et al. 2009; Alfè et al. 2010). Ethylene soot presents an intermediate behavior since it is formed in an environment rich of both light aliphatic and aromatic (benzene) hydrocarbons. Thus, soot presents from the beginning a structure with an order intermediate between methane and benzene soot, the presence of both aliphatic and aromatic hydrogen and it is prone to undergo an almost fully dehydrogenation and graphitization process.

Both FT-IR and Raman spectroscopy supported the UV-Visible analysis results giving information of the hydrogen functionality and on the carbon network structure. A method for the quantitative analysis of aliphatic and aromatic hydrogen and a deep analysis of Raman parameters allowed following dehydrogenation of soot accompanied by the increase of the ordering of soot structure during the soot formation process as a function of the fuel nature and temperature field.

5.1 Open questions and future perspectives

The flame synthesis of carbon materials is a field of research that has not been yet exploited in all its potentiality. A well -controlled combustion system, i.e. a premixed flame, has shown to be able to produce different particulate matters burning different fuels in a narrow temperature range. This work has been focused on the upgrade and the exploiting of the diagnostic potentiality of spectroscopic analysis for the quantitative and qualitative characterization of carbon materials and

their related micro- and nano-structure. Beside this, a deep knowledge of the carbonaceous species formation mechanism inside a flame environment, was obtained on the basis of the experimental results. A relationship between synthesis/combustion conditions and carbon properties, such as size, chemical composition, optical properties and internal structural organization, has been found.

This information can be useful in order to select combustion conditions to produce carbonaceous materials with tailored properties. Indeed, with the start of the nano-age, there has been tremendous interest in the combustion synthesis of materials because it is simple, fast, self-sustained and energetically economic compared to the conventional routes used to prepare carbon materials. However, the main efforts have been done up to now to produce directly in flame perfect carbon allotropes, as graphene, nanotube, fullerene, neglecting the more concrete and reliable possibility of considering a combustion system as a high yield source of less ordered carbon structures nonetheless useful for less demanding applications.

Ultimately, the production through combustion synthesis of carbon particulate matter in form of carbon particles and/or of molecular precursors could be significant in the context of finding a convenient *bottom-up* approach for the production of carbon materials having chemico-physical properties suitable for industrial applications.

Of course, this is a challenging and ambitious objective that can be achieved through what was attempted to get in this work, and has constituted one of the main aim of the thesis. That is, to give a contribution in the knowledge of the properties of these carbon materials and the related effect of combustion conditions, provided that appropriate and specific diagnostic tools are developed.

References

Aisenberg S, Chabot R., J. Appl. Phys., 42, 2953-2958, 1971.

Akhter M. S., Chughtai A. R., Smith D. M., The Structure of Hexane Soot I: Spectroscopic Studies, Applied Spectroscopy, 39, 143-153, 1985.

Alfè M., Apicella B., Rouzaud J.N., Tregrossi A., Ciajolo A., The effect of temperature on soot properties in premixed methane flames Combust. Flame, 157, 1959–1965, 2010.

Alfè M., Apicella B., Tregrossi A., Ciajolo A., Identification of large polycyclic aromatic hydrocarbons in carbon particulates formed in a fuel-rich premixed ethylene flame, Carbon, 46, 2059–2066, 2008.

Alfè M.,Apicella B., Barbella R., Rouzaud J.-N., Tregrossi A., Ciajolo A., Structure–property relationship in nanostructures of young and mature soot in premixed flames, Proceedings of the Combustion Institute, 32, 697-704, 2009.

Andresen J. M., Zhang Y. Z., Burgess C. E., Schobert H. H., .Synthesis of pitch materials from hydrogenation of anthracite, Fuel Processing Technology, 1361-1372, 2004.

Apicella B., Alfè M., Barbella R., Tregrossi A., Ciajolo A., Aromatic structures of carbonaceous materials and soot inferred by spectroscopic analysis, Carbon , 42, 1583-1589, 2004.

Apicella B., Carpentieri A., Alfè M., Barbella R., Tregrossi A., Pucci P., Ciajolo A., Mass spectrometric analysis of large PAH in a fuel-rich ethylene flame, Proc. Combust. Inst., 31, 547–553, 2007.

Aso H., Matsuoka K., Sharma A., Tomita A., Evaluation of Size of Graphene Sheet in Anthracite by a Temperature-Programmed Oxidation Method, Energy Fuels, 18, 1309–1314, 2004.

Bakry R, Vallant RM, Najam-ul-Haq M, Rainer M., Szabo Z., Huck C. W., Bonn G. K., Medicinal applications of fullerenes. Int J Nanomedicine, 2, 4, 639–649, 2007.

Berlman, I. B. Handbook of Fluorescence Spectra of Aromatic Molecules, 2nd ed.; Academic Press: New York, 1971.

Biscoe J, Warren B. E., An X-Ray Study of Carbon Black, J. Appl. Phys., 13, 364-372, 1942.

Bockhorn H., D'Anna A., Sarofim A. F., Wang H., Combustion Generated Fine Carbonaceous Particles,. KIT Scientific Publishing, Karlsruhe, 2009.

Böhm H., Hesse D., Jander H., Luers B., Pietscher J., Wagner H. G. G., Weiss M., The influence of pressure and temperature on soot formation in premixed flame, Proc. Combust. Inst. 22, 403-411, 1988.

Bond T. C., Bergstrom R. W., Light Absorption by Carbonaceous Particles: An Investigative Review, Aerosol Science and Technology, 39, 1–41, 2006.

Carpentier Y., Féraud G., Dartois E., Brunetto R., Charon E., Cao A.-T., d'Hendecourt L., Bréchignac P., Rouzaud J.-N., T. Pino, Nanostructuration of carbonaceous dust as seen through the positions of the 6.2 and 7.7 μm AIBs, A&A, 548, 2012.

Casiraghi C, Ferrari A. C., Robertson J., Raman spectroscopy of hydrogenated amorphous carbons, Physical Review B, 72, 085401, 2005.

Chhowalla M., Ferrari A. C., Robertson J., Amaratunga G. A. J., Evolution of sp2 Bonding with Deposition Temperature in Tetrahedral Amorphous Carbon Studied by Raman Spectroscopy, Appl. Phys. Let. 76, 1419–1421, 2000.

Choy K. L., Chemical vapour deposition of coatings, Progress in Materials Science, 48, 57–170, 2003.

Ciajolo A., Barbella R., Tregrossi A., Bonfanti L., Spectroscopic And Compositional Signatures Of Pah-Loaded Mixtures In The Soot Inception Region Of A Premixed Ethylene Flame, Proc. Combust. Inst., 27, 1481–1487, 1998.

Ciajolo A., D'Anna A., Barbella R., Tregrossi A., Violi A., The effect of temperature on soot inception in premixed ethylene flames, Proc. Combust. Inst., 26, 2327-2333, 1996.

Ciajolo A., Ragucci R., Apicella B., Barbella R., de Joannon M., Tregrossi A., Fluorescence spectroscopy of aromatic species produced in rich premixed ethylene flames, Chemosphere, 42, 835-841, 2001.

Conboy J. C., Messmer M. C., Richmond G. L., Dependence of Alkyl Chain Conformation of Simple Ionic Surfactants on Head Group Functionality As Studied by Vibrational Sum-Frequency Spectroscopy, J. Phys. Chem. B, 101, 6724-6733, 1997.

D Alessio A., Barone A. C., Cau R., D'Anna A., Minutolo P., Surface deposition and coagulation efficiency of combustion generated nanoparticles in the size range from 1 to 10 nm, Proceedings of the Combustion Institute, 30, 2595–2603, 2005.

D'Alessio A., D'Anna A., D'Orsi A., Minutolo P., Barbella, R., Ciajolo, A.,. Precursor formation and soot inception in premixed ethylene flames. Proc. Combust. Inst. 24, 973–980, 1992.

D'Anna A., Ciajolo A., Alfè M., Apicella B., Tregrossi A., Effect of fuel/air ratio and aromaticity on the molecular weight distribution of soot in premixed n-heptane flames, Proceedings of the Combustion Institute, 32, 803–810, 2009a.

D'Anna A., Combustion-formed nanoparticles, Proceedings of the Combustion Institute, 32, 593–613, 2009b.

D'Anna A., Violi A., D'Alessio A., Modeling the Rich Combustion of Aliphatic Hydrocarbons, Combustion and Flame, 121, 418–429, 2000.

Dischler B., Bubenzer A., Koidl P., Bonding in hydrogenated hard carbon studied by optical spectroscopy, Solid State Comun. 48, 105-108, 1983.

Dobbins R. A., Fletcher R. A., Lu W., The Evolution of Soot Precursor Particles in a Diffusion Flame, Combust. Flame, 100, 301–309 1995.

Dobbins R. A., Megadiris C. M., Morphology of flame-generated soot as determined by thermophoretic sampling, Langmuir, 3, 254–259, 1987.

Dresselhaus M. S., Dresselhaus G., Eklund P. C., Science of Fullerenes and Carbon Nanotubes, Academic Press, London, 1996.

Dresselhaus M. S., Dresselhaus G., Saito R., Physics Of Carbon Nanotubes, Carbon, 33, 883-891, 1995.

Duley W. W., Seahra S., Graphite, polycyclic aromatic hydrocarbons, and the 2175 Å extinction feature, The Astrophysical Journal, 507, 874-888, 1998.

Ergun S, Alexander L. E., Crystalline forms of carbon: A possible hexagonal polymorph of diamond, Nature, 195, 765-767, 1962.

Ergun S, Tiensuu V. H., Tetrahedral structures in amorphous carbons, Acta Cryst., 12, 1050-1051, 1959.

Faccinetto A., Desgroux P., Ziskind M., Therssen E., Focsa C., High-sensitivity detection of polycyclic aromatic hydrocarbons adsorbed onto soot particles using laser desorption/laser ionization/time-of-flight mass spectrometry: An approach to studying the soot inception process, in low-pressure flames, Combustion and Flame, 158, 227-239, 2011.

Ferrari A. C., Robertson J., Resonant Raman spectroscopy of disordered, amorphous, and diamondlike carbon, Phys. Rev. B 64, 75414 2001.

Ferrari A.C., Raman spectroscopy of graphene and graphite: Disorder, electron-phonon coupling, doping and nonadiabatic effects, Solid State Communications 143, 47-57, 2007.

Ferrari, A. C., Robertson, J. Interpretation of Raman spectra of disordered and amorphous carbon Phys. Rev. B61, 14095-14107, 2000.

Fetzer J. C., Large (C>=24) polycyclic aromatic hydrocarbons, John Wiley & Sons Inc., New York, 2000

Fitzer E., Kochling K. H., Boehm H. P., Marsh H, Recommended Terminology For The Description Of Carbon As A Solid, Pure & Appl. Chem., 67, 473-506, 1995.

Franklin R. E., Proc. Roy. Soc., 209, 196-218, 1951.

Frenklach M., Wang H., Detailed Modeling of Soot Particle Nucleation and Growth, Proc. Combust. Inst., 23, 1559–1566, 1990.

Frenklach M., Wang H., in: Soot Formation in Combustion: Mechanisms and Models, Bockhorn H., Springer-Verlag, Berlin, 162-190, 1994.

Frenklach, M., Reaction mechanism of soot formation in flames, Physical Chemistry Chemical Physics, 4, 2028-2037, 2002.

Fristrom R. M., Westenberg A. A., Flame Structure, McGraw-Hill, New York, U.S.A., 1965.

Galvez A., Herlin-Boime M., Reynaud C., Clinard C., Rouzaud J.N., arbon nanoparticles from laser pyrolysis, Carbon, 40, 2775–2789, 2002.

Gotoh Y., Kajiura S., FT-IR studies of graphite after keV-energy hydrogen ion irradiation, Journal of Nuclear Materials, 266-269, 1051-1058, 1999.

Grieco W. J., Howard J. B., Rainey L.C., Vander Sande J. B., Fullerenic Carbon in Combustion-Generated Soot, Carbon, 38, 597-614, 2000.

Grill, A., Diamond-like carbon: state of the art, Diamond and Related Materials, 8, 428–434, 1999.

Grotheer H. H., Wolf K., Hoffmann K., Photoionization mass spectrometry for the investigation of combustion generated nascent nanoparticles and their relation to laser induced incandescence, Appl. Phys. B, 104, 367-383, 2011.

Guo T., Nikolaev P., Rinzler A. G., TomBnek D., Colbert D. T, Smalley R. E., Self-Assembly of Tubular Fullerenes, J. Phys. Chem.,99, 10694-10697, 1995.

Haddon R. C., Hebard A. F., Rosseinsky M. J., Murphy D. W., Duclos S. J., Lyons K. B., Miller B., Rosamilia J. M., Fleming R. M., Kortan A. R., Glarum S. H., Makhija A. V., Muller A. J., Eick R. H., Zahurak S. M., Tycko R., Dabbagh G., Thiel F. A., Conducting films of C60 and C70 by alkali-metal doping, Nature, 350, 320-322, 1991.

Harris P. J. F., Fullerene-like models for microporous carbon, J Mater Sci, 48, 565-577, 2013.

Harris P. J. F., New Perspectives on the Structure of Graphitic Carbons, Solid State and Materials Sciences, 30, 235–253, 2005.

Harris P.J.F., Liu Z., Suenaga K., Imaging the atomic structure of activated carbon, J Phys: Condens Matter, 20, 1-5, 2008.

Haynes B. S., Wagner H. G., Soot formation, Prog. Energy Combust. Sci., 7, 229–273, 1981.

Heidenreich R. D., Hess W. M., Ban L. L., A test object and criteria for high resolution electron microscopy, J. Appl. Cryst., 1, 1-19, 1968.

Henning, Th., Jäger, C., Mutschke, H., Laboratory studies of carbonaceous dust analogs, Astrophysics of Dust, 309, 603–629, 2004.

Hernandez Y, Nicolosi V, Lotya M, Blighe FM, Sun Z, De S, McGovern IT, Holland B, Byrne M, Gun'Ko YK, Boland JJ, Niraj P, Duesberg G, Krishnamurthy S, Goodhue R, Hutchison J, Scardaci V, Ferrari AC, Coleman JN., High-yield production of graphene by liquid-phase exfoliation of graphite, Nature Nanotechnology, 3, 563–568, 2008.

Homann K. H., Formation of large molecules, particulates and ions in premixed hydrocarbon flames; Progress and unresolved questions, Proc. Combust. Inst., 20, 857–870, 1985.

Homann K.-H., Fullerenes and Soot Formation New Pathways to Large Particles in Flames, Angew. Chem. Int. Ed., 37, 2434-2451, 1998..

Hortal A. R., Hurtado P., Martinez-Haya B. M., Mullins O.C., Molecular-Weight Distributions of Coal and Petroleum Asphaltenes from Laser Desorption/Ionization Experiments, Energy&Fuel, 21, 2863-2868, 2007.

Howard J. B., Carbon addition and oxidation reactions in heterogeneous combustion and soot formation, Symposium (International) on Combustion, 23, 1107–1127, 1991.

Huang X., Fabrication and Properties of Carbon Fibers, Materials, 2, 2369-2403, 2009.

Iijima S., Ichihashi T., Nature, 363, 603-605,1993.

Iijima S., Nature 354, 56−58, 1991.

Jacob W., Unger M., Experimental determination of the absorption strength of C–H vibrations for infrared analysis of hydrogenated carbon films, Appl. Phys. Lett., 68, 475-477, 1996.

Jäger C., Henning T., Schlögl R., Spillecke O., Spectral properties of carbon black, Journal of Non-Crystalline Solids, 258, 161-179, 1999.

Jäger C., Krasnokutski S., Staicu A., Huisken F., Mutschke H., Henning Th., Poppitz W., Voicu I., Identification and Spectral Properties of Polycyclic Aromatic Hydrocarbons in Carbonaceous Soot Produced by Laser Pyrolysis, ApJS, 166, 557-566, 2006.

Jäger C., Mutschke H., Dorschner J., Henning Th., Optical properties of carbonaceous dust analogues, Astron. Astrophys., 332, 291-299, 1998.

Jenkins G. M., Kawamura K., Polymeric carbons—Carbon Fibre, Glass and Char, Cambridge University Press, 1976.

Kaskan W. E., Dependence of flame temperature on mass burning velocity, Proc. Combust. Inst., 6, 134-143, 1965.

Kroto H. W., Heath J. R., O'Brien S. C., Curl R. F., Smalley R. E., C_{60}: Buckminsterfullerene, Nature, 318, 162−163, 1985.

Kroto H. W., Walton D. R. M., The Fullerenes New Horizons for the Chemistry, Physics and Astrophysics of Carbon, Cambridge University Pres, 1993.

Larouche N., Stansfield B. L., Classifying nanostructured carbons using graphitic indices derived from Raman spectra, Carbon, 48, 620–629, 2010.

Lee C. H., Lambrecht W. R. L., Segall B., Kelires P. C., Frauenheim T., Stefan U., Electronic structure of dense amorphous carbon, Physical Review B 49. 11448-11451 1994.

Lee M. L., Novotny M. V., Bartle K. D., Analytical Chemistry of Polycyclic Aromatic Compounds; Academic Press: New York, 1981.

Li C.; Wu F.; Cai H.; Kandiyoti R., UV-fluorescence spectroscopy of coal pyrolysis tars, Energy Fuels, 8, 1039-1048, 1994.

Llamas-Jansa I., Jäger C., Mutschke H., Henning Th., Far-ultraviolet to near-infrared optical properties of carbon nanoparticles produced by pulsed-laser pyrolysis of hydrocarbons and their relation with structural variations, Carbon, 45, 1542–1557, 2007.

Marsh H., Rodríguez Reinoso F., Activeted carbon, Elsevier Ltd., Oxford, 2006.

Mennella V., Colangeli L., Bussoletti E., Merluzzi P., Monaco G., Palumbo P., Rotundi A., Laboratory experiments on cosmic dust analogues: the structure of small carbon grains, Planet. Space Sci., 43, 1217-1221 (1995).

Merchan-Merchan W, Saveliev A.V., Kennedy L. High-rate flame synthesis of vertically aligned carbon nanotubes using electric field control, Carbon, 42, 599-608, 2004.

Merchan-Merchan W, Saveliev A.V., Kennedy L., Fridman A.A.. Formation of carbon nanotubes in counter-flow, oxy-methane diffusion flames without catalyst, Chem Phys Lett, 354, 20-24, 2002.

Merchan-Merchan W., Saveliev A. V., Kennedy L., Jimenez W. C., Combustion synthesis of carbon nanotubes and related nanostructures, Progress in Energy and Combustion Science, 36, 696-727, 2010.

Miller J. A., Melius C. F., Kinetic and thermodynamic issues in the formation of aromatic Compounds In Flames Of Aliphatic Fuels, Combust. Flame, 91, 21–39, 1992.

Miller J. H., Herdman J. D., Green C. D. O., Webster E. M., Experimental and computational determinations of optical band gaps for PAH and soot in a N_2-diluted, ethylene/air non-premixed flame, Proceedings of the Combustion Institute ,34, 3669–3675, 2013.

Millikan R. C., Optical Properties of Soot, J. Opt. Soc. Am. 51:698–699, 1961.

Minutolo P., Gambi G., D'Alessio A., The Optical Band Gap Model in the Interpretation of the UV-Visible Spectra of Rich Premixed Flames Proc. Combust. Inst., 26, 951–957, 1996.

Mochida I., Korai Y., Ku C., Watanabe F., Sakai Y., Chemistry of synthesis, structure, preparation and application of aromatic-derived mesophase pitch, Carbon, 38, 305–328, 2000.

Mochida I., Korai Y., Nakamura M., Zeng S., Kameyana M., Structure and carbonization properties of pitches produced catalitically from aromatic hydrocarbons with HF/BF3, Carbon, 26, 843-852, 1988.

Muller J. O., Su D. S., Wild U., Schlogl R., Bulk and surface structural investigations of diesel engine soot and carbon black, Phys. Chem. Chem. Phys., 9, 4018–4025, 2007.

Mullins O. C., Sheu E.Y., Hammami A., Marshall A. G., Asphaltenes, Heavy Oils and Petroleomics, Springer, New York, 2007.

Mullins O. C.; Sabbah H.; Eyssautier J.; Pomerantz A. E.; Barre L.; Andrews A. B.; Ruiz-Morales Y.; Mostowfi F.; McFarlane R.; Goual L.; Lepkowicz R.; Cooper T.; Orbulescu J.; Leblanc R. M.; Edwards J.; Zare R. N., Advances in asphaltene science and the Yen− Mullins model, Energy Fuels, 26, 3986−4003, 2012.

Nathan A., Ahnood A., Cole M. T., Lee S., Suzuki Y, Hiralal P., Bonaccorso F., Hasan T, Garcia-Gancedo L., Dyadyusha A., Haque S., Andrew P., Hofmann S., Moultrie J., Chu D., Flewitt A. J., Ferrari A. C., Kelly M. J., Robertson J., Amaratunga G. A. J., Milne W. I., Flexible Electronics: The Next Ubiquitous Platform, Proceedings of the IEEE ,100, 1486-1517, 2012.

Novoselov K. S., Geim A. K., Morozov S. V., Jiang D., Zhang Y., Dubonos S. V., Grigorieva I. V., Firsov A. A., Electric field effect in atomically thin carbon films, Science, 306, 666-669, 2004.

Oberlin A., Application Of Dark-Field Electron Microscopy To Carbon Study, Carbon, 17, 7-20, 1979.

Oberlin A., in: P.A. Thrower (Ed.), Chemistry and Physics of Carbon, vol. 22, Marcel Dekker, New York, 1990.

Osawa E., Superaromaticity, Kagaku (Chemistry), 25, 854-863, 1970 (In Japanese).

Palotas A. B., Rainey L. C., Feldermann C. J., Sarofim A. F., Sande J. B. V., Soot Morphology: An Application of Image Analysis in High-Resolution Transmission Electron Microscopy, Microsc. Res. Technol., 33, 266–278, 1996.

Patrick J. W., Porosity in carbons: characterization and applications, Edward Arnold, London, 1995.

Pino T., Dartois E., Cao A. T., Carpentier Y., Chamaillé T, Vasquez R., Jones A. P., d'Hendecourt L., Bréchignac P., The 6.2 μm band position in laboratory and astrophysical spectra: a tracer of the aliphatic to aromatic evolution of interstellar carbonaceous dust, A&A, 490, 665–672, 2008.

Pope C. J., Marr J. A., Howard J. B., Chemistry of Fullerenes C_{60} and C_{70} Formation in Flames, J. Phys. Chem., 97, 11001-11013, 1993.

Postma H. W., Teepen T, Yao Z, Grifoni M, Dekker C., Carbon nanotube single-electron transistors at room temperature, Science, 293, 76-79, 2001.

Reich S., Thomsen C., Raman spectroscopy of graphite, Phil. Trans. R. Soc. Lond., 362, 2271-2288, 2004.

Reina A., Jia X., Ho J., Nezich D., Son H., Bulovic V., Dresselhaus M. S., Kong J, Large Area, Few-Layer Graphene Films on Arbitrary Substrates by Chemical Vapor Deposition, Nano Lett., 9, 30-35, 2009.

Richter H, Howard J. B., Formation of polycyclic aromatic hydrocarbons and their growth to soot—a review of chemical reaction pathways, Progress in Energy and Combustion Science, 26, 565–608, 2000.

Richter H., Benish T. G., Mazyar O. A., Green W. H., Howard J. B., Formation of polycyclic aromatic hydrocarbons and their radicals in a nearly sooting premixed benzene flame, Proceedings of the Combustion Institute, 28, 2609–2618, 2000.

Ristein J., Stief R. T., Ley L., Beyer W., A comparative analysis of a-C:H by infrared spectroscopy and mass selected thermal effusion, Journal of Applied Physics, 84, 3836- 3847, 1998.

Robertson J., Diamond-like amorphous carbon, Materials Science Engineering R, 37, 129-281, 2002.

Robertson J., Electronic processes in hydrogenated amorphous carbon, Journal of Non-Crystalline Solids, 198 -200, 615-618, 1996.

Robertson J., Gap states in diamond-like amorphous carbon, Philosophical Magazine Part B, 76:3, 335-350, 1997.

Robertson J., Hard amorphous (diamond-like) carbons, Prog. Solid St. Chem., 21, 199-333, 1991.

Robertson J., O'Reilly E. P., Electronic and atomic structure of amorphous carbon, Phys. Rev B, 35, 2946-2957, 1987.

Robertson J., Structural models of a-C and a-C:H Diamond and Related Materials, 4, 297-301, 1995.

Rodgers R. P., Reilly P. T. A., Whitten W. B., Ramsey J. M., Real-time observation of metastable polymeric species formed from precursor soot, Chemical Physics Letters, 397, 324-328, 2004.

Rodil S. E., Infrared spectra of amorphous carbon based materials, Diamond and Related Materials, 14, 1262–1269, 2005.

Roth P., Particle synthesis in flames, Proceedings of the Combustion Institute, 31,1773–1788, 2007.

Russo C, Stanzione F., Ciajolo A., Tregrossi A., Study of the contribution of different molecular weight specie sto the absorption UV-Visible spectra off lame-formed carbon species, Proceeding of Combustion Institute, 34, 3661-3668, 2013b.

Russo C., Alfè M., Rouzaud J.-N., Stanzione F., Tregrossi A., Ciajolo A., Probing structures of soot formed in premixed flames of methane, ethylene and benzene, Proceedings of the Combustion Institute 34, 1885–1892, 2013a.

Russo C., Stanzione F., Alfè M., Ciajolo A., Tregrossi A., Spectral Analysis in the UV-Visible Range for Revealing the Molecular Form of Combustion-Generated Carbonaceous Species, Combust. Sci. and Tech, 184, 1219-1231, 2012.

Russo C., Stanzione F., Tregrossi A., Alfè M., Ciajolo A., The effect of temperature on the condensed phases formed in fuel-rich premixed benzene flames, Combustion and Flame, 159, 2233–2242, 2012.

Sadezky, A., Muckenhuber, H., Grothe, H., Niessner, R., and P¨oschl, U., Raman Spectra of Soot and Related Carbonaceous Materials: Spectral Analysis and Structural Information, Carbon, 43, 1731–1742, 2005.

Santamaria A., Nancy Yang N., Eric Eddings E., Fanor Mondragon F., Chemical and morphological characterization of soot and soot precursors generated in an inverse diffusion flame with aromatic and aliphatic fuels, Combustion and Flame, 157, 33–42, 2010.

Savaliev A, Merchan-Merchan W, Kennedy L., Metal catalyzed carbon nanostructures in an opposed flow methane oxygen flame. Combust Flame, 135, 27-33, 2003.

Schnaiter M., Gimmler M., Llamas I., Linke C., Jäger C., Mutschke H., Strong spectral dependence of lightabsorption by organic carbon particles formed by propane combustion, Atmos. Chem. Phys. Discuss., 6, 1841-1866, 2006.

Schnaiter M., Horvath H., Mohler O., Naumann K. H., Saathoff H., Schock O. W., UV-VIS-NIR spectral optical properties of soot and soot-containing aerosols, Journal of Aerosol Science, 34, 1421-1444, 2003.

Schnaiter, M.; Henning, Th.; Mutschke, H.; Kohn, B.; Ehbrecht, M.; Huisken, F., Infrared Spectroscopy Of Nano-Sized Carbon Grains Produced By Laser Pyrolysis Of Acetylene: Analog Materials For Interstellar Grains, The Astrophysical Journal, 519, 687-696, 1999.

Schobert H. H, Song C., Chemicals and materials from coal in the 21st century, Fuel, 81, 15–32, 2002.

Schwan J., Ulrich S., Batori V., Ehrhardt H., Silva S. R. P., Raman spectroscopy on amorphous carbon films, J. Appl. Phys., 80, 440-4477, 1996.

Sirignano M., Alfè M., Tregrossi A., Ciajolo A., D'Anna A., Experimental and modeling study on the molecular weight distribution and properties of carbon particles in premixed sooting flames, Proceedings of the Combustion Institute, 33, 633-640, 2011.

Sirignano M., D'Anna A., Coagulation of combustion generated nanoparticles in low and intermediate temperature regimes: An experimental study, Proceedings of the Combustion Institute, 34, 1877–1884, 2013.

Soewono A., Rogak S., Morphology and Raman Spectra of Engine-Emitted Particulates, Aerosol Science and Technology, 45, 1206-1216, 2011.

Tauc J., Grigorovici R., Vancj A., Optical properties and electronic structure of amorphous germanium, Phys. Stat. Sol.,15, 627-637, 1966.

Thrower P. A., Nomenclature of sp^2 carbon nanoforms, Carbon, 50, 741-747, 2012.

Tomita S., Fujii M., Hayashi S., Defective Carbon Onions in Interstellar Space as the Origin of the Optical Extinction Bump at 217.5 Nanometers, The astrophysical Journal, 609, 220-224, 2004.

Tregrossi A., Ciajolo A., Barbella R., The combustion of benzene in rich premixed flames at atmospheric pressure, Combust. Flame, 117, 553–561, 1999.

Tregrossi A., Ciajolo A., Spectral Signatures of carbon particulate evolution in methane flames Combust. Sci. and Tech., 182, 683-691, 2010.

Tuinstra F., Koening J. L., Raman Spectrum of Graphite, J. Chem. Phys. 53, 1126-1130, 1970.

Ulrich G. D., Flame synthesis of fine particles, Chem. Eng. News, 62,22–29, 1984.

Vander Wal R. L., Tomasek A. J., Soot oxidation: dependence upon initial nanostructure, Combustion and Flame, 134, 1–9, 2003.

Vander Wal R.L., Flame synthesis of substrate-supported metal-catalyzed carbon nanotubes, Chem Phys Lett 324, 217-223, 2000.

Vo-Dinh, T., Multicomponent analysis by synchronous luminescence spectrometry, Anal. Chem., 50, 396-401, 1978.

Wada N., Gaczi P. J., Solin A., Diamond-like three-fold coordinated amorphous carbon, J. Non-Cryst. Solids 35&36, 543-548, 1980.

Walker P. L., Carbon: an old but new material revisited, Carbon, 28, 261-279, 1990.

Wang H., Formation of nascent soot and other condensed-phase materials in flames, Proceedings of the Combustion Institute, 33, 41–67, 2011.

Wang X., Li X., Zhang L., Yoon Y., Weber P. K., Wang H., Guo J., Dai H., N-doping of graphene through electrothermal reactions with ammonia, Science, 324, 768–771, 2009.

Warren B. E., X-ray diffraction study of carbon black, J. Chem. Phys., 2, 551-556, 1934.

Wasserfallen D., Kastler M., Pisula W., Hofer W. A., Fogel Y., Wang Z., Müllen K., Suppressing Aggregation in a Large Polycyclic Aromatic Hydrocarbon, J. Am. Chem. Soc., 128, 1334-1339, 2006.

Westbrook C. K., Mizobuchi Y., Poinsot T. J., Smith P. J., Warnatz J., Computational combustion, Proceedings of the Combustion Institute, 30, 125-157, 2005.

Williams T. C., Shaddix C. R., Jensen K. A., Suo-Anttila J. M., Measurement of the dimensionless extinction coefficient of soot within laminar diffusion flames, Int. J. Heat Mass Transfer, 50, 1616–1630, 2007.

Zhang J., Megaridis C. M., Soot Microstructure in Steady and Flickering Laminar Methane/Air Diffusion Flames, Combustion and Flame, 112, 473-484, 1998.

Zhao Y., Wei J., Vajtai R., Ajayan P. M., Barrera E. V., Iodine Doped Carbon Nanotube Cables Exceeding Specific Electrical Conductivity of Metals, Sci. Rep., 83, 1-5, 2011.